SLAC-R-641

NON-QUIESCENT X-RAY EMISSION FROM NEUTRON STARS AND BLACK HOLES

Derek Martin Tournear

SLAC-Report-641
August 2003

Prepared for the Department of Energy
under contract number DE-AC03-76SF00515

SLAC-R-641

NON-QUIESCENT X-RAY EMISSION FROM NEUTRON STARS AND BLACK HOLES*

Derek Martin Tournear

Stanford Linear Accelerator Center
Stanford University
Stanford, CA 94309

SLAC-Report-641
August 2003

Prepared for the Department of Energy
under contract number DE-AC03-76SF00515

Printed in the United States of America. Available from the National Technical Information Service, U.S. Department of Commerce, 5285 Port Royal Road, Springfield, VA 22161.

*Ph.D. thesis, Stanford University, Stanford, CA 94309.

NON-QUIESCENT X-RAY EMISSION FROM NEUTRON STARS AND BLACK HOLES

A DISSERTATION
SUBMITTED TO THE DEPARTMENT OF PHYSICS
AND THE COMMITTEE ON GRADUATE STUDIES
OF STANFORD UNIVERSITY
IN PARTIAL FULFILLMENT OF THE REQUIREMENTS
FOR THE DEGREE OF
DOCTOR OF PHILOSOPHY

Derek Martin Tournear
August 2003

© Copyright by Derek Martin Tournear 2003
All Rights Reserved

I certify that I have read this dissertation and that, in my opinion, it is fully adequate in scope and quality as a dissertation for the degree of Doctor of Philosophy.

Elliott D. Bloom
(Principal Adviser)

I certify that I have read this dissertation and that, in my opinion, it is fully adequate in scope and quality as a dissertation for the degree of Doctor of Philosophy.

Grzegorz Madejski

I certify that I have read this dissertation and that, in my opinion, it is fully adequate in scope and quality as a dissertation for the degree of Doctor of Philosophy.

Robert V. Wagoner

Approved for the University Committee on Graduate Studies:

Abstract

X-ray astronomy began with the detection of the persistent source Scorpius X-1. Shortly afterwards, sources were detected that were variable. Centaurus X-2, was determined to be an X-ray transient, having a quiescent state, and a state that was much brighter. As X-ray astronomy progressed, classifications of transient sources developed. One class of sources, believed to be neutron stars, undergo extreme luminosity transitions lasting a few seconds. These outbursts are believed to be thermonuclear explosions occurring on the surface of neutron stars (type I X-ray bursts). Other sources undergo luminosity changes that cannot be explained by thermonuclear burning and last for days to months. These sources are soft X-ray transients (SXTs) and are believed to be the result of instabilities in the accretion of matter onto either a neutron star or black hole.

Type I X-ray bursts provide a tool for probing the surfaces of neutron stars. Requiring a surface for the burning has led authors to use the presence of X-ray bursts to rule out the existence of a black hole (where an event horizon exists not a surface) for systems which exhibit type I X-ray bursts. Distinguishing between neutron stars and black holes has been a problem for decades.

Narayan and Heyl have developed a theoretical framework to convert suitable upper limits on type I X-ray bursts from accreting black hole candidates (BHCs) into evidence for an event horizon. We survey 2101.2 ks of data from the USA X-ray timing experiment and 5142 ks of data from the Rossi X-ray Timing Explorer (RXTE) experiment to obtain the first formal constraint of this type. 1122 ks of neutron star data yield a population averaged mean burst rate of $1.7 \pm 0.4 \times 10^{-5}$ bursts s^{-1}, while 6081 ks of BHC data yield a 95% confidence level upper limit of 4.9×10^{-7} bursts s^{-1}.

Applying the framework of Narayan and Heyl we calculate regions of luminosity where the neutron stars are expected to burst and the BHCs would be expected to burst if they had a similar surface. In this luminosity region 464 ks of neutron star data yield an averaged mean burst rate of $4.1 \pm 0.9 \times 10^{-5}$ bursts s^{-1}, and 1512 ks of BHC data yield a 95% confidence level upper limit of 2.0×10^{-6} bursts s^{-1} and a strong limit that BHCs do not burst with a rate similar to the rate of neutron stars in these regions. This gives evidence that BHCs do not have surfaces.

In addition to studying type I X-ray bursts, we analyzed the SXT behavior. In particular, 4U 1630−47, was analyzed throughout its 1999 outburst. This source is one of the oldest known SXTs. This source is assumed to be a BHC in a low-mass X-ray binary system. Despite the length of time devoted to studying this source, there is still little known about it.

We report the results of timing and spectral analysis on the 1999 outburst, and compare these results to other outbursts of 4U 1630−47. We found this source progressed from a low-hard state to a high-soft state and then rapidly transitioned back into the low-hard state before returning to quiescence. Timing analysis detected a low frequency quasi-periodic oscillation (LFQPO) during the initial rise of the outburst, which disappeared and did not return. The variability in the X-ray flux in the 0.1–2000 Hz frequency range is low during the high state, but increases as the source progresses into the low-hard state.

The next generation Gamma Ray Large Area Space Telescope (GLAST), will measure astrophysical phenomena in the 20 MeV − a few TeV energy range. We describe preliminary design and testing of GLAST. The detector is based on a silicon tracker with similar design characteristics of vertex detectors used in high-energy physics experiments at accelerator based facilities. A beam test engineering model was designed, constructed, and tested at SLAC in 1999–2000. We describe this test, and discuss how the results from this test can improve and demonstrate the viability of the GLAST technology.

Acknowledgements

It is right to give thanks and praise.
– excerpt from the Eucharistic Prayer

Gratitude is not only the greatest of virtues, but the parent of all the others.
– Cicero (106–43 B.C.)

I am grateful to my advisor Elliott Bloom for giving me the opportunity and guidance to perform the research that went into this dissertation. Elliott taught me many things about working in the scientific community and working with fellow scientists. Lessons learned while observing Elliott manage experiments while never losing track of the science questions will stay with me for a long time.

Bob Wagoner, and the other members of my committee have also contributed to this work. Their constructive comments greatly improved this thesis. I also received helpful comments from Erik Kuulkers, Lev Titarchuk, J.-P. Lasota, and an anonymous referee.

When I first came to group EK, Eduardo do Couto e Silva took me under his wing. I learned enough about silicon and hardware testing to be competent thanks to Eduardo. Eduardo also introduced me to the silicon community. As I progressed in my studies Eduardo's advice and encouragement was always helpful. Eduardo is a marvelous mentor and a joy to work with. I hope that someday we will collaborate on a project.

I cannot show enough appreciation for Warren Focke, who taught me most of the astrophysics I know. Warren's expertise in astrophysics, mathematics, computers and

analysis was indispensable to the completion of this dissertation. Warren has been a true asset to group EK.

I would also like to thank Kaice Reilly and Pablo Saz Parkinson. Without the help of these two USA data experts I would still be analyzing data for this dissertation. I also thank Pablo for stimulating political debates that kept life interesting.

The USA collaborators at NRL have been a great resource for astrophysical information. Paul Ray, Mike Wolff and Kent Wood provided essential scientific advice and comments to allow me to complete the work that led to this dissertation.

Summer students Rishik Saxena and Erica Raffauf were instrumental in the completion of this work. Rishik performed a large amount of the initial analysis on the 4U 1630–47 outburst and Erica performed the initial scan of the type I X-ray burst data. I also want to thank Alex Enu for his contribution to the type I X-ray burst analysis.

Alicia Kavelaars has been a wonderful coworker and friend throughout my research. As a coworker, she helped me make a lot of progress in TOT analysis. As a friend, she helped me through some rough times here at Stanford.

There are many other coworkers that have been key to the completion of my degree Berrie Giebels has been a great source for analysis advice. Greg Madejski, Paul Kunz, Marios Nikolaou, Heather Arrighi Kelly, and many more have helped me with science and technical problems too numerous to count.

I thank everyone at Purdue who taught me the physics and engineering skills that I have utilized to get where I am today. The course work and research I performed as a Purdue student continues to be my scientific foundation.

Thank you V. L. Price for convincing me to go to graduate school and encouraging me along the way. I am grateful to my parents for supporting me through this long process. My friends in physics, Nikolai Tolich, Tony Bollinger, and others have kept me sane throughout this process by allowing me to commiserate with them.

I can not thank Martha Kelly enough for reintroducing me to Jesus and introducing me to Vernita Ediger. Both have been life savers during this process. I can not thank God enough for all the great things he has done for me. I owe a great debt to Vernita, she has been with me through this and I love her very much.

I am also grateful for the facilities and support at SLAC. I thank the Department of Energy and NASA that funded the majority of this work. Work at SLAC was supported by the Department of Energy contract DE-AC 0376-SFO0515. Basic research in X-ray astronomy at the US Naval Research Laboratory is supported by ONR/NRL. This work was also supported by the NASA Applied Information Systems Research Program.

Anyone with good sense
is eager to learn more,
but fools are hungry
for foolishness.
– Proverbs 15:14 (CEV)

Contents

Abstract v

Acknowledgements vii

1 Introduction 1

2 Overview of Cosmic X-ray Sources 3

2.1 Neutron Stars . . . 3

2.1.1 Neutron Star Formation . . . 3

2.1.2 Types of Neutron Stars . . . 4

2.2 Black Holes . . . 10

2.2.1 Black Hole Formation . . . 10

2.2.2 Types of Systems . . . 11

3 Astrophysics Experiments 13

3.1 The Unconventional Stellar Aspect Experiment (USA) . . . 13

3.1.1 Description of USA . . . 13

3.1.2 USA Detector Hardware . . . 15

3.1.3 GPS and USA . . . 19

3.1.4 USA Data . . . 29

3.2 The Rossi X-ray Timing Explorer . . . 33

3.2.1 RXTE Hardware . . . 33

3.2.2 RXTE Data . . . 36

3.3 GLAST . . . 43

3.3.1 Description of the GLAST Experiment 43
3.3.2 Timeline 48

4 Type I X-ray bursts **49**
4.1 Introduction to Type I X-ray bursts 49
4.1.1 Type I X-ray Burst Observation 49
4.1.2 Type I X-ray Burst Theory 51
4.1.3 X-ray Bursts as Evidence for Surfaces 54
4.2 Observations and Data Analysis 55
4.2.1 Data Analysis 55
4.2.2 Observations of Neutron Star Systems 60
4.2.3 Observations of Black Hole Candidates 62
4.3 Discussion 65
4.3.1 Theoretical Framework of Narayan & Heyl 65
4.3.2 Luminosity Calculation 69
4.3.3 BHC Surface Limit 79
4.3.4 Comparison of Narayan & Heyl Theory to Neutron Star Observations 81
4.4 Burst Rates and Limits Conclusions 82
4.5 Analysis of USA Type I X-ray burst data 83
4.5.1 Spectral Analysis 83
4.5.2 Timing Analysis 84

5 Soft X-ray Transient Outbursts **88**
5.1 Introduction to SXT Theory in LMXBs 88
5.2 4U 1630−472 Outburst Analysis 92
5.2.1 Introduction 92
5.2.2 RXTE Observations 93
5.2.3 USA Observations 95
5.2.4 Data Analysis 97
5.2.5 Discussion 109
5.2.6 Conclusions 112

6 Conclusions and Perspectives **113**
6.1 Summary . . . 113
6.1.1 Type I X-ray Burst Summary . . . 113
6.1.2 4U 1630−47 Outburst Summary . . . 114
6.2 Future Developments . . . 116
6.2.1 X-ray Astrophysics . . . 116
6.2.2 Gamma Ray Astrophysics with GLAST . . . 119

A Systems of Time Used in Astrophysics **126**

B GLAST Beam Test Engineering Model (BTEM) **131**
B.1 GLAST BTEM Overview . . . 131
B.1.1 Introduction . . . 131
B.1.2 Construction of the BTEM . . . 132
B.1.3 Future Plans . . . 139
B.1.4 Conclusion . . . 139
B.2 Tray Alignment Measurements . . . 140
B.3 GLAST BTEM Time Over Threshold (TOT) Analysis . . . 154
B.3.1 Introduction . . . 154
B.3.2 TOT Operation . . . 155
B.3.3 Purpose and Description of TOT . . . 155
B.3.4 Readout Process of TOT . . . 156
B.3.5 TOT Calibration . . . 158
B.3.6 Charged Particle Rejection . . . 159
B.3.7 Position of Photon Conversion . . . 161
B.3.8 Position of Photon Conversion: Comparing TOT to Reconstruction . . . 162
B.3.9 Analysis of Photon Acceptance . . . 163
B.3.10 Position of Photon Conversion: Comparing TOT to Event Display 164
B.3.11 One and Two MIP Discrimination . . . 166
B.3.12 Conclusions . . . 167
B.4 GLAST BTEM Microdischarge Studies . . . 168

C List of Abbreviations **175**

Bibliography **178**

List of Tables

3.1 Summary of the USA Science Data Modes 30
3.2 Description of RXTE Standard Products 38
3.3 Description of Common RXTE Data Modes 40
3.4 Science Parameters of GLAST 45

4.1 USA observing times of X-ray binaries searched for bursts 56
4.2 Detected type I X-ray bursts of the USA experiment 63
4.3 Fit Parameters for Burst Luminosity Calculation 72
4.4 List of Cuts Used for X-ray Burst Search 76
4.5 X-ray Burst Rates and Limits from the USA & RXTE Experiments . 80

5.1 Energy Spectra Fit Parameters From 4U 1630−47 1999 Outburst . . 99

B.1 Silicon yield during the GLAST beamtest construction. 135
B.2 Bad channels during testbeam construction. 135
B.3 Leakage current progression for all ladders though the production steps. 137
B.4 Ladder yield during beamtest construction. 137
B.5 Alignment Map For Monte Carlo Simulation 153
B.6 TOT Calibration 160
B.7 Comparison of algorithms used to find the location of the photo-conversion point 166
B.8 Bias Voltages for the BTEM Runs 169

C.1 List of Abbreviations 177

List of Figures

2.1 Color-color diagram showing differences in Z and atoll sources 9

3.1 Picture of the USA instrument 14
3.2 Layout of one USA detector. 16
3.3 Positioning of the USA experiment aboard the ARGOS satellite. . . . 18
3.4 Mounting scheme of the USA instrument 18
3.5 Cartoon showing the GPS Constellation orbits. 21
3.6 The RXTE satellite and its different instruments. 33
3.7 Artist's conception of GLAST satellite instrument 44
3.8 Artist's conception of GLAST Silicon Tracker 44
3.9 Cartoon outlining the operation of a pair production telescope. 46

4.1 Diagram showing the CNO, hot CNO and rp processes 53
4.2 Example of a typical type I X-ray burst 60
4.3 Example of type II X-ray burst behavior in the Rapid Burster 62
4.4 Regions of instability predicted by NH02 for type I X-ray bursts . . . 68
4.5 Spectral fit to Aquila X-1 in the hard state with USA data 71
4.6 Distribution of the log $\left(\frac{L}{L_{\rm Edd}}\right)$ for the BHC observations 73
4.7 Distribution of the log $\left(\frac{L}{L_{\rm Edd}}\right)$ for the neutron star observations 74
4.8 Distribution of simulated log $\left(\frac{L}{L_{\rm Edd}}\right)$ 78
4.9 Temperature and normalization during type I X-ray bursts (part 1) . 85
4.10 Temperature and normalization during type I X-ray bursts (part 2) . 86
4.11 Temperature and normalization during type I X-ray bursts (part3) . . 87

5.1 Cartoon describing the states of a soft X-ray transient outburst. . . . 91
5.2 The ASM dwell by dwell light curve of the 1999 4U 1630−47 outburst. 94
5.3 The ASM dwell by dwell light curve of 4U 1630−47 showing outbursts in 1996, 1998, 1999 and 2000/2001 95
5.4 The 1999 outburst light curve of 4U 1630−47 96
5.5 Spectral model components of 4U 1630−47 data 100
5.6 Example of a spectral fit to 4U 1630−47 RXTE data near the outburst peak 101
5.7 Example of a spectral fit to 4U 1630−47 RXTE data in the outburst tail 102
5.8 The contribution to overall flux by the individual model components of observation 40418-01-42-00. 103
5.9 Plots showing the progression of the 1999 4U 1630−47 outburst as it moves to different states 104
5.10 Plot showing the evolution of the disk temperature, hardness ratio, and disk radius during the 1999 outburst 107
5.11 Plot showing the evolution of the disk radius vs. disk temperature during the 4U 1630–47 1999 outburst 108
5.12 QPO seen during the beginning of the 1999 outburst. 110
5.13 RMS during the 1999 outburst of 4U 1630−47 111

6.1 X-ray all-sky map 116
6.2 Gamma-ray all-sky map 120

B.1 GLAST BTEM ladder gluing jig 133
B.2 Arrangement of the silicon layers in the BTEM tracker design. 133
B.3 Drawing showing details of silicon detectors used in the GLAST beamtest. 134
B.4 Drawing showing the construction of the trays. 138
B.5 Picture showing the GLAST BTEM tracker 138
B.6 Calibration of z measurement for GLAST BTEM tray measurement . 141
B.7 GLAST BTEM ladder straightness definition 142
B.8 Distribution of GLAST BTEM ladder straightness 142
B.9 Drawing defining GLAST BTEM tray angle measurement 143

B.10 Distribution of angle measurements of the GLAST BTEM ladders . . 144
B.11 Cross-section of GLAST BTEM tray 146
B.12 Z positional error in the GLAST BTEM 147
B.13 Vertex positions in the GLAST BTEM 148
B.14 Cartoon demonstrating the TOT progression along the path of a particle in the tracker 156
B.15 GLAST BTEM TOT distribution of a 20 GeV positron 159
B.16 Background rejection using TOT 162
B.17 The TOT distribution progression following a track in the tracker, see B.14 163
B.18 Rejection and acceptance power of the TOT 165
B.19 TOT distribution correlated to vertex position in tracker 168
B.20 Noise in a Large Leaky Strip 170
B.21 Noise in a Medium Leaky Strip 171
B.22 Strip occupancy vs. voltage 172
B.23 Noise vs. voltage 173
B.24 Hits per strip vs. strip 174

Chapter 1

Introduction

In 1962, the first extrasolar X-ray source, Scorpius X-1, was discovered by a team led by Riccardo Giacconi[1]. This discovery led to forty years of exciting discoveries in X-ray astrophysics.

It was soon discovered that some of the brightest galactic sources emit radiation almost exclusively in the X-ray band. Scorpius X-1, for example, emits ten thousand times as much radiation as our Sun, and 99.9% appears in the X-ray band. Soon after, the first X-ray pulsar, Centaurus X-3 was discovered. Around the same time the first non-quiescent X-ray behavior was detected. Centaurus X-2 was discovered where previously no X-ray emission was measured. It became clear that this source underwent periods of quiescent (dim or normal) behavior and periods of non-quiescent (outburst or bright) behavior. Many X-ray sources have a nearly constant or slightly variable X-ray luminosity[2], interrupted by periods of large increases in X-ray flux. These jumps in flux are what we term *non-quiescent* behavior and generally fall into two main categories. First, there are increases in flux caused by rapid thermonuclear burning. In this dissertation we call this non-quiescent behavior short-term, or X-ray burst. It typically lasts from a few to hundreds of seconds. X-ray bursts were initially

[1]Dr. Riccardo Giacconi was awarded the 2002 Nobel Prize in Physics for his work in the field of X-ray astrophysics.

[2]X-ray pulsars undergo regular pulsed X-ray emission. In this dissertation we consider the pulsed emission part of the quiescent or normal emission from the source.

discovered in 1975 as an X-ray spike that emitted $\sim 10^{39}$ ergs of X-ray energy[3] in about 10 s. Second, there are increases in flux caused by drastic changes in the processes that produce the quiescent emission, usually an increase in material falling onto, or accreting, onto a compact object. This non-quiescent behavior is called long-term or soft X-ray transient (SXT) behavior and typically lasts from weeks to months.

This dissertation is divided into two main areas of X-ray astrophysics reflecting these two main classifications in non-quiescent X-ray behavior. In Chapter 2 background on the types and formation of the sources to be studied is given. Chapter 3 discusses the three astrophysics experiments that were used to complete the work that went into this dissertation. Chapter 4 is devoted to the short-term non-quiescent behavior, in particular type I X-ray bursts. The first part of Chapter 4 discusses the theory of X-ray bursts and how we have analyzed them to show that there is a difference in the physical properties of neutron stars and black hole candidates. We show observational evidence that surfaces on black hole candidate systems can not exist without some radical changes in the equation of state of the object. The second part of Chapter 4 discusses some spectral and timing analysis performed on the X-ray bursts we have detected. Chapter 5 focuses on the long-term non-quiescent behavior. In particular, the SXT behavior of a particular source, 4U 1630−47 a black hole candidate, is studied in detail. Chapter 6 gives an overview of the results and the prospects for future X-ray and gamma-ray astrophysics. Appendix B details useful information from the results and analysis of the GLAST gamma-ray mission beam test.

[3]For comparison it would take the Sun about 10^{11} s to emit this much X-ray radiation.

Chapter 2

Overview of Cosmic X-ray Sources

2.1 Neutron Stars

Neutron stars are extremely dense, $\rho_{max} \approx 3 \times 10^{14} - 3 \times 10^{15}$ g cm^{-3}, collapsed cores of burned out stars. For comparison, consider the density of ordinary nuclear matter, $\rho \approx 3 \times 10^{14}$ g cm^{-3}. Neutron stars are the result of a balance between gravitational collapse and nuclear degeneracy pressure in stellar material. Neutron star masses are bound to lie between 1.4 M$_\odot \lesssim M_{NS} \lesssim$ 3.0 M$_\odot$ Most neutron stars, where the mass has been determined, have masses clustered tightly around 1.4 M$_\odot$. The lower limit is based on the Chandrasekhar limit below which a white dwarf exists (balanced by electron degeneracy pressure), and the upper limit is based on the point at which gravity would crush the neutron star into a black hole. This upper limit is dependent on the equation of state of the neutron star. Neutron stars possess a wide range of magnetic fields, from millisecond radio pulsars with $\sim 10^8$ G to magnetars believed to power anomalous X-ray pulsars (AXPs) and soft gamma ray repeaters (SGRs) with $\sim 10^{15}$ G.

2.1.1 Neutron Star Formation

Neutron stars form as the result of a supernova explosion at the end of a star's lifetime. There are two main types of supernovae, distinguished by their optical

spectra. Type II supernovae have hydrogen lines, type I do not. Type II supernovae form when a massive star, $M \gtrsim 8\ M_\odot$ burns out. The star becomes stratified like an onion with different layers of burning elements, with hydrogen on the surface and iron as the core. Iron is the most bound of all nuclei so it no longer fuses. The temperatures and pressures build up from the addition of more iron to the core until the iron finally photodisintegrates into alpha particles and neutrons. The alpha particles themselves break apart and the free protons combine with electrons that had been helping to support the core with electron degeneracy pressure. The process now runs away and the core collapses until nuclear density is reached, forming a neutron star. Shock waves and turbulent flow cause the outer shell of the star to be blown off in a violent supernova explosion releasing $\sim 10^{51}$ ergs, and leaving behind a neutron star. Type Ib and Type Ic supernovae are also caused by core collapse of a star. However, there is little or no hydrogen in their outer envelopes.

Type Ia supernovae differ from the supernova types listed above. The progenitor star is believed to be a white dwarf which is in a binary orbit with another star. The white dwarf accretes material from its companion until its mass is pushed above the Chandrasekhar limit and it undergoes rapid collapse similar to the type II supernova case. Type Ia supernovae do not leave behind neutron star remnants. Type Ia supernovae are characterized by the presence of a strong silicon line and no hydrogen lines. See Wheeler & Harkness (1990), Weiler (2003), Shu (1982) for a more complete review of supernovae.

2.1.2 Types of Neutron Stars

Isolated Neutron Stars

When isolated neutron stars are first formed, there is residual heat that can produce X-ray emission, and some models allow for accretion from the interstellar medium (ISM) to produce X-ray radiation. Neutron stars which are formed isolated are difficult to detect in the X-ray band unless they are pulsars. The generally accepted view is that neutron stars are formed with large magnetic fields, $B \approx 10^{11-13}$ G, and spin rapidly, $P \approx 10^{-2} - 10$ s. The pulsar drags its magnetosphere along with its rotation,

and electrons stripped from the rotating surface are trapped in the field lines of the magnetosphere. The electrons accelerate along the field lines until they reach a point where continuing to co-rotate with the neutron star would require them to approach the speed of light (at the speed of light cylinder). As the electrons approach this speed they give up a significant portion of their energy in the form of synchrotron emission that is seen as a power law emission in radio bands. A handful of isolated pulsars will produce X and gamma-ray radiation. The exact process by which this occurs is unknown and probing these systems for clues is one of the missions of the GLAST experiment described in §6.2.2. One of the main competing theories involves emission occurring far away from the star near the speed of light cylinder. Here the charge density goes to zero, so there is a gap in the charge distribution. Theories that invoke emission originating near this cylinder are called "outer gap" models (see e.g. Chiang & Romani 1994). There is another gap region where there is charge depletion. This region occurs above the polar caps, and there are theories that invoke processes occurring at this point to produce high energy emission. These theories are called "polar cap" theories (see e.g. Chiang & Romani 1992, Goldreich & Julian 1969, Harding & Muslimov 2001). These theories are not mutually exclusive, radiation can be produced by both mechanisms in a single system (Holloway 1973). In each of these scenarios the vast majority of the energy to produce the radio and high-energy emission comes from conversion of rotational energy of the star into electromagnetic and particle energy. For this reason, these isolated pulsars are observed to spin down over long periods of time (rotational period increases).

Anomalous X-ray Pulsars There is another type of birth scenario for an isolated neutron star. The anomalous X-ray pulsars (AXPs), and soft gamma ray repeaters (SGRs) are believed to be born with very strong magnetic fields, $B \approx 10^{14-16}$ G, and spin periods of, $P \approx 2 - 10$ s (Gaensler et al. 2001). The luminosities of the AXPs are very constant at 10^{34-36} erg s^{-1}, which is too much radiation for a pulsar with such a long period to produce solely by loss of rotational energy. To explain these sources, new theories of magnetic field decay are invoked to give the pulsars another means of producing energy. These two types of sources are now considered variants of

the same class, called 'magnetars'. Magnetars have only recently been discovered and understood, see Gavriil & Kaspi (2002), Thompson & Duncan (1995), and references therein for a review of these sources.

Neutron Star Binaries

Many stars are in a binary system, and often the binary system survives after one of the stars undergoes a supernova explosion. In this case the neutron star will be formed in a binary orbit with its companion star. The neutron star will accrete matter from the companion and convert the gravitational energy from the infalling matter into radiation energy with a high efficiency ($\sim 50 - 100\%$). This system is called an X-ray binary. X-ray binaries are the brightest objects in the X-ray sky.

The spectral type of the companion star influences the details of the accretion onto the neutron star and is the next parameter used to classify the type of neutron star binary.

High Mass X-ray Binaries (HMXBs) HMXBs are binary systems where the companion star is generally an O or B class star with a mass greater than 10 $M_\odot$. The OB companion will generate significant stellar wind, removing between $10^{-6} - 10^{-10}$ $M_\odot$ yr^{-1} (Lewin, van Paradijs, & van den Heuvel 1995). The compact object in orbit with this source will capture a large fraction of this wind and convert it to X-ray emission. The orbit may be very eccentric leading to transient behavior as the compact object moves closer and further away from the companion in orbit. Transient HMXBs may also be formed when the companion is a rapidly rotating Be star which forms a disk that undergoes mass-ejection episodes leading to transient activity. Roche lobe overflow may supplement the accretion due to the wind. However, full Roche lobe overflow becomes unstable after $\sim 10^5$ yrs if the mass ratio of compact object to companion is greater than unity (Lewin & den Heuvel 1983). In this case the compact object will spiral in to the massive star. As the supergiant approaches its Roche lobe, increased focusing of accretion onto the compact object can occur. HMXBs are young, bacause the life of an OB star is short, and they retain a large fraction of the magnetic field they are born with (see above). If a compact object has

a magnetic field around 10^{10} G or greater it will disrupt the accretion flow and funnel the material onto the magnetic poles (Lewin, van Paradijs, & van den Heuvel 1995). If the magnetic and rotation axis are misaligned, X-ray pulsations will be observed if the beamed emission crosses our line of sight. For this reason, the majority of HMXBs are X-ray pulsars, most notably Centaurus X-3, and Vela X-1.

Low Mass X-ray Binaries (LMXBs) LMXBs have companion stars $M \lesssim 1$ M$_\odot$. With such a low mass companion it is actually an extremely rare event that the binary system survived the supernova explosion and remained as an X-ray binary. However, since the low mass star has a much longer lifetime, LMXBs are more common in the X-ray sky than HMXBs. The more massive of the two stars in a binary evolves faster and proceeds to supernova first. Before undergoing a supernova explosion, a large portion of the envelope of the more massive star is either: (1) transferred to the companion (2) lost from the binary as the companion spiraled in or (3) lost from the binary in the form of stellar wind. During the supernova explosion if less than half of the binary mass is lost in the explosion, then the binary will survive the explosion. If more than half the mass is lost in the supernova, then the binary can only survive by a kick velocity from the explosion that happens to be in the right direction.

After the LMXB forms, the companion star expands to fill the Roche lobe and the compact object begins accreting material from the companion. The accreting material will form a disk if $R_{\rm circ} = \frac{J^2}{GM_1}$ is larger than the radius of the accretor, where J is the specific angular momentum of the infalling matter and M_1 is the mass of the compact object. This condition always holds if accreting via Roche lobe overflow, because the particles started out on a companion that has enough angular momentum to orbit the compact object.

Millisecond Pulsars As with the HMXBs, some LMXB systems are detected as X-ray or radio pulsars. Present theories suggest that if a LMXB is in a wide orbit with a companion $M \sim 0.2 - 0.4$ M$_\odot$ then the accretion may cause the compact object to spin up very rapidly. If the magnetic field is low, $\lesssim 10^9$ G, then the spin period can get as low as $\sim$ milliseconds. These neutron stars would be very old as it

would have taken accretion a long time (LMXB lifetime is $10^8 - 10^9$ yr) to spin up such objects. Therefore, the principal explanation proposes that extended periods of accretion cause a decay in the neutron star's magnetic field, and also transfer angular momentum to the neutron star. These effects cause the neutron star to spin rapidly. If the spin axis is misaligned with the magnetic field axis and the radiation beam crosses our line of sight, a millisecond pulsar will be observed. The companion may no longer be present; some theories suggest that the companion is eroded away by radiation from the pulsar. There are more millisecond pulsars than are expected from this simple explanation. This has led to many theories involving detailed mass transfer in other orbits besides wide binary orbits. However, the main process of spinning up to millisecond periods is the same. See Chapter 5 in Lewin, van Paradijs, & van den Heuvel (1995) for more information on millisecond pulsars. The fastest X-ray pulsar is 1937+21, a 1.6 ms pulsar with no detected companion (Alpar et al. 1982).

Z & Atoll Sources LMXBs are further broken down according to spectral measurements. If a soft color (ratio of count rates in the two lowest energy bands) is plotted against the hard color (ratio of count rates in the two highest energy bands) two distinct types of neutron star LMXBs become evident. In a color-color diagram of hard color versus soft color the brightest sources follow a so-called Z track, and the dimmer sources follow a fragmented path, with an island state, and a banana shaped state. The sources are classified as either 'Z source' or 'atoll source' based on this observation. See Figure 2.1 for some representative color-color diagrams.

Z sources show three kinds of states, corresponding to the upper part of the Z, the horizontal branch (HB), the connecting part of the Z, the normal branch (NB), and the bottom branch of the Z, the flaring branch (FB). It has been found that Z sources have higher $\dot{M}$ and magnetic field than atoll sources (Gierliński & Done 2002). Most Z sources are bright and are accreting near their Eddington limit[1] when they are in the NB and FB. Z sources rarely show X-ray bursts, usually only when

[1]The Eddington limit is the luminosity where radiation pressure would overcome gravitational pressure, generally $L_{\rm Edd} = 4\pi c GMm/\sigma_T$, where M is the mass of the object, m is the mass of the particle, and σ_T is the Thomson cross section. See §4.3.2 for details on calculating $L_{\rm Edd}$.

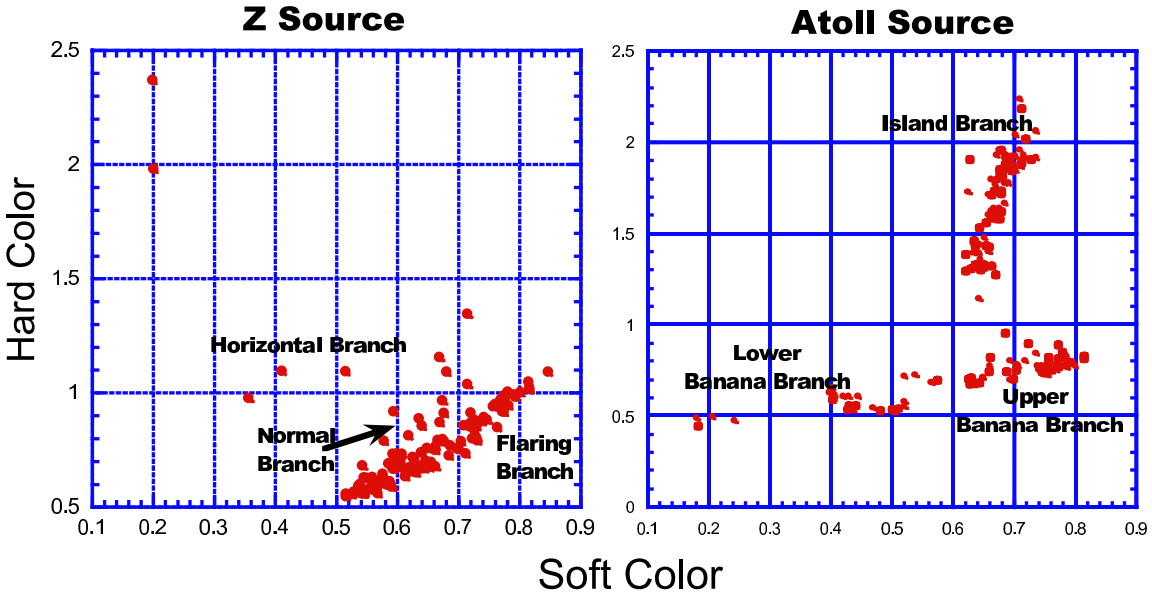

Figure 2.1 A color-color diagram demonstrating the differences between Z and atoll sources. These data are from USA light curves, one point per observation ($\sim 10 - 20$ minutes). The Z source is Scorpius X-1, and the atoll source is Aquila X-1. The hard color is (5.4–13.4 keV)/(3.1–5.4 keV); the soft color is (3.1–5.4 keV)/(1.1–3.1 keV). The two points in the upper left of the Z source show a feature of a very hard state that is seen in some Z sources. Aquila X-1 is a representative atoll source, however, the patterns formed in color-color diagrams of atoll sources are varied.

they are in the HB, whereas atoll sources frequently show X-ray bursts. Z sources may also have longer orbital periods, but measurements are insufficient to conclude this. Seperating the two classes of sources based on the magnetic field strength is model dependent. Some atoll sources that have evolved into brighter sources have been detected to display NB & FB behavior in color-color diagrams, making the distinction less clear (Muno, Remillard, & Chakrabarty 2001).

2.2 Black Holes

In §2.1 we described neutron stars. Neutron stars are a state of matter that is formed by the balance between gravity and neutron degeneracy pressure. A black hole is an object more massive than a neutron star, so massive that the force of gravity overwhelms the neutron degeneracy pressure[2] causing the object to collapse even further. No well established model can resist the subsequent collapse to a singularity.

In General Relativity, a black hole can be completely described by its mass, charge and angular momentum. Since black holes are postulated to exist, but have not been proven to exist by direct measurements (see §4.3), compact objects too massive to exist as neutron stars are usually referred to as black hole candidates (BHCs).

Black holes are detected through radiation given off by accretion. There are four types of black holes. First, stellar mass black holes, which are galactic black holes with a mass of ~ 10 $M_\odot$. Second, supermassive black holes are formed at the center of galaxies and have mass of $\sim 10^{6-9}$ $M_\odot$. Third, intermediate mass black holes, these recently discovered[3] objects may have a mass $\sim 10^{3-5}$ $M_\odot$. Fourth, primordial black holes, which have not been detected, but some theories propose that black holes could have been created in the early universe by external compression. They could have very small masses and very short lifetimes. Unless specified otherwise, all mention of black holes in this dissertation will refer to stellar mass black holes.

2.2.1 Black Hole Formation

Black holes may be formed in supernova similar to neutron stars. However, the progenitor star of the black hole would be very massive, $M \gtrsim 30$ $M_\odot$. The supernova may be very energetic, exploding in a hypernova explosion, perhaps giving off a gamma ray burst (van Paradijs 2001). The explosion may also take place in two steps, first forming a neutron star core, then quickly collapsing further as more mass falls onto the core. When the core mass exceeds ~ 3 $M_\odot$ then the core can no longer exist as ordinary nuclear matter. A black hole is the expected result.

[2]This is not true for supermassive black holes.

[3]The discovery of these objects is still a subject of debate (Körding, Falcke, & Markoff 2002).

Black holes may also be formed from a neutron star that is accreting material after it is formed via common envelope accretion (Podsiadlowski, Rappaport, & Han 2003), a mechanism which is questioned (Armitage & Livio 2000). Neutron stars can accrete at much higher than the Eddington rate in this situation. Neutron star mergers may also be a means of creating black holes. If a neutron star merges with its companion, which could also be a neutron star, then a black hole may result (Belczynski, Bulik, & Kalogera 2002).

2.2.2 Types of Systems

Stellar mass black holes can form as individual, HMXB or LMXB just like their neutron star counterparts. For this reason, observational distinction between BHCs and neutron stars is difficult (see §4.2.1). Stellar BHCs commonly show up as X-ray transients. Transients are not strictly defined, but usually refer to sources that are not detected in quiescence and are only detected when they undergoes an X-ray outburst. These outbursts can last from weeks to months and can recur on time scales of months to decades, and may occur at regular or irregular intervals. More information about BHC transients can be found in §5.1. The first BHC discovered, Cygnus X-1, is part of a HMXB and is one of the brightest persistent hard X-ray source in the sky..

The following formulas and numbers give the reader a sense of the size of these systems. First, the Schwarzchild radius, the location of the "event horizon" of a black hole, is approximated by setting the escape velocity to the speed of light,

$$R_S = \frac{2GM}{c^2}, \text{ where } \frac{2G\mathrm{M}_\odot}{c^2} \approx 3 \text{ km}. \tag{2.1}$$

This value is for a non-rotating (Schwarzchild) black hole. It is more likely that the black hole was formed with angular momentum and is rotating. In a rotating black hole, the angular momentum intrinsic to the black hole creates some modifications of this value. From General Relativity theory, a rotating black hole (Kerr black hole)

has an event horizon:

$$\begin{aligned} R &= R_S/2 + \sqrt{(R_S/2)^2 - a^2} \\ a &= \frac{J}{Mc} \\ 0 \leq |a| &\leq R_S/2. \end{aligned}$$

A maximally rotating 10 $M_\odot$ black hole has an event horizon of 15 km. There exists another surface, called the static limit, within which an object must rotate with the black hole. The boundary for the static limit is at the event horizon on the poles and expands to R_S at the equator. The volume between the event horizon and the static limit is called the *ergosphere*. The second dimension to keep in mind is the minimum stable circular orbit. Called the *innermost stable circular orbit*, this is

$$R_{\rm ISCO} = R_S \times \begin{cases} 1/2, & a = R_S/2 \\ 3, & a = 0 \\ 9/2, & a = -R_S/2 \end{cases} \tag{2.2}$$

$R_{\rm ISCO} \approx 90$ km for a 10 $M_\odot$ non-rotating black hole.

Chapter 3

Astrophysics Experiments

There is no higher or lower knowledge,
but one only, flowing out of experimentation.
– Leonardo da Vinci (1452–1519)

3.1 The Unconventional Stellar Aspect Experiment (USA)

3.1.1 Description of USA

USA (Figure 3.1) is a low-cost X-ray timing experiment built jointly by the Naval Research Laboratory (NRL) and the Stanford Linear Accelerator Center (SLAC) for the dual purpose of conducting studies of variability in X-ray sources and exploring applications of X-ray sensor technology (see Ray et al. (2001) for more details). USA was launched on 1999 February 23 aboard the Advanced Research and Global Observation Satellite (ARGOS), and took data until the mission ended in 2000 November. The primary observing targets were bright galactic X-ray binaries, with the goal of obtaining large exposures on a small number of sources ($\sim$ 30 of the most luminous sources). See §3.1.4 for more information on the observations of USA. USA has the effective area, precise timing ability, and data throughput capability to probe these

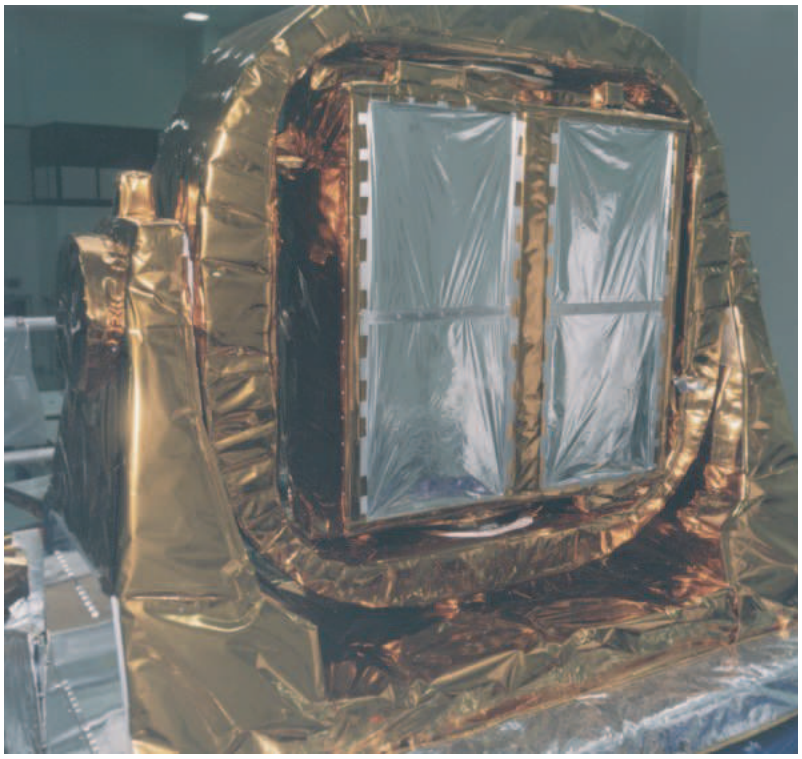

Figure 3.1 USA instrument picture showing the two detectors assembled onto the yoke and pylons prior to integration onto the ARGOS spacecraft.

sources at the timescales of processes near neutron star surfaces or the innermost stable orbits around black holes (Ray et al. 2001). See chapter 2 for more information on these systems.

The main characteristics of the USA mission include:

- a mission concept that allows long observing times on bright X-ray objects,
- large-area detectors with high time resolution (effective area[1] at 3 keV of 2000 cm^2; telemetry: 40 kbs, 128 kbs available for short periods; event timing accurate to better than 32 μs),
- good low energy response, 1–15 keV with a resolution of 1 keV at 5.9 keV,

[1]This effective area is for both detectors on USA. One detector was damaged very early in the mission, so nearly all USA data were obtained with one detector with an effective area of 1000 cm^2.

- absolute time-tagging using a GPS receiver, see §3.1.3,
- a collimated field of view (FOV) of $1.2° \times 1.2°$ (FWHM),
- the Crab Nebula gives about 3500 cts s^{-1} at the center of the FOV in one detector.
- nearly circular Sun-synchronous orbit, 830 km altitude, 98.7° inclination
- with ~ 7400 ks of data from sources collected during the mission lifetime.

A second objective of the USA mission was to conduct experiments involving applied uses of X-ray detectors and reliable computing in space (Wood 1994). This objective is not discussed here.

3.1.2 USA Detector Hardware

Proportional Counter

The detector consists of two multiwire constant flow counters that were refurbished from the NASA Spartan-1 mission (Kowalski et al. 1993). Early in the mission one counter was damaged. All data analyzed in this dissertation are from one detector only. Each detector has an effective area of 1000 cm^2 at 3 keV. USA is a pointed timing and spectral instrument, collimated by a copper hexcell collimator (see Figure 3.2) giving a $1.2° \times 1.2°$ (FWHM) FOV, with a flat top of $\sim 0.05°$. Each detector collimator is constructed from eight identical collimator modules whose response was individually measured at SLAC prior to assembly (Wen 1997; Ray et al. 2001).

USA is effective over the energy range 1–15 keV, with detection up to ~ 30 keV. The energy resolution is 17% at 5.9 keV. The spectral information is recorded either in 8, 16, or 48 Pulse Height Analyzer (PHA) channels depending on the mode of operation (see §3.1.4 for more information on data modes). The minimum energy is determined by the detector window material and thickness. The energy resolution is limited by the intrinsic resolution of the proportional counter and secondarily the number of PHA channels used. Onboard energy calibration was performed using an ^{55}Fe source that could be moved in front of the detector. In addition, the chamber

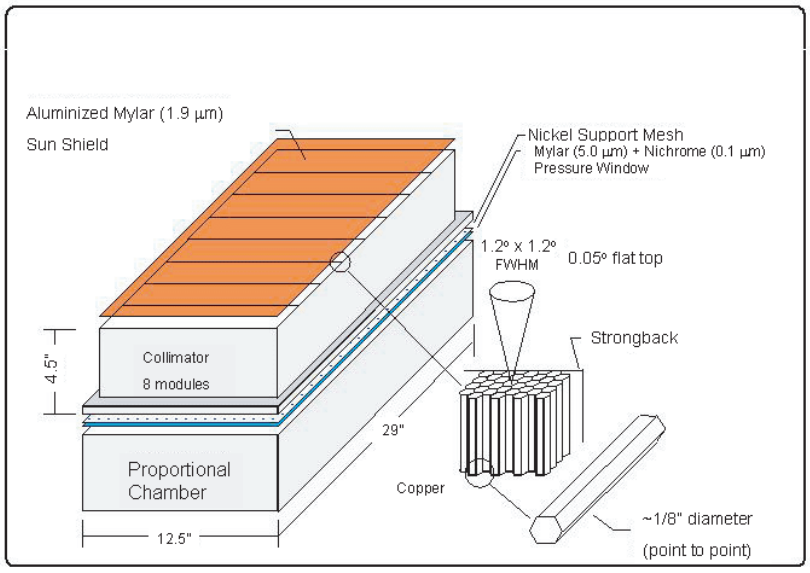

Figure 3.2 Layout of one USA detector.

high-voltage is automatically adjusted to stabilize the gain, using a feedback mechanism that monitors pulse height distribution of the X-ray events from another ^{55}Fe source. ^{55}Fe decays by electron capture to ^{55}Mn* which emits lines of 5.9 & 6.4 keV when the ^{55}Mn* electrons return to the ground state. In addition to these lines, there are lines associated with the difference between the incoming photon energy and the ionization energy of the gas in the detector (argon). These *escape peak* lines occur when a photon emitted from a de-exciting argon atom escapes the detector undetected ($\sim 4\%$ effect). This makes it appear as the incoming photon had a lower energy than it actually did. The *escape peak* energies for the ^{55}Fe source occur at 2.9 & 3.5 keV. In addition to these lines from the ^{55}Fe source, there is an 8.04 keV Cu$-$k emission line from X-rays exciting the copper in the collimator. The escape peak for this line is too small to be detected. These lines are used for on-orbit energy calibration (Saz Parkinson 2003). It was found that different energy calibrations are needed for the ascending and descending sides of the orbit. This is due to temperature differences in the gas chamber. Details can be found in Saz Parkinson (2003).

Events are tagged to a precision of either 2 μs, 32 μs or 10 ms if using the binned spectrum mode. The high timing resolution allows USA to probe kilohertz astrophysical events. The event times are time-tagged relative to an absolute time given by an onboard GPS receiver, see §3.1.3 for more information on the operation of the GPS receiver on ARGOS.

The USA gas chambers are filled with P-10 gas, 90% argon 10% methane, at 16.1 psia (at room temperature). The gas is contained by a 5.0 μm Mylar window covered with a 1.9 μm aluminized Mylar Sun shield, see Figure 3.2. The detector interior consists of an array of wires providing two layers (top (0) and bottom (1)) of nine 2.8 cm square cells, with one anode wire each running along the length of the counter. An additional wire runs around the periphery of the array as part of the cosmic ray veto system. When X-rays are absorbed by the gas, they usually impart all of their energy to a single electron, which quickly transfers the energy to nearby electrons. It is unlikely that any of these electrons will escape one detector cell and reach another cell. However, an energetic charged particle entering the detector can cross several cells. Therefore, if an event triggers more than one anode, including the peripheral anode, then it is vetoed with an efficiency of about 99% (Ray et al. 2001).

USA Pointing system

The ARGOS spacecraft is a three-axis-stabilized nadir pointed observatory. USA was designed to offset point from the ARGOS spacecraft, see Figure 3.3. USA's detectors are mounted on a 2-axis gimballed platform, on the $-z$ (velocity vector) side of the satellite, to permit inertial pointing at celestial objects. Thus, the pointer is configured as an equatorial mount looking aft. Pointing is accomplished by a yaw rotation to acquire the target, followed by a continuous slew in the pitch to track the target as the spacecraft orbits. Figure 3.4 shows the positioning of the yoke supporting the detector, and the pylons attaching the yoke to ARGOS. Figure 3.3 shows the placement of USA onto ARGOS. This unique pointing system posed challenges as the amount of obscuration from the detector supporting yoke needs to be accounted for when calculating the detector effective area for different yaw angles. The yaw and pitch values for the detector are included in housekeeping data and are used to

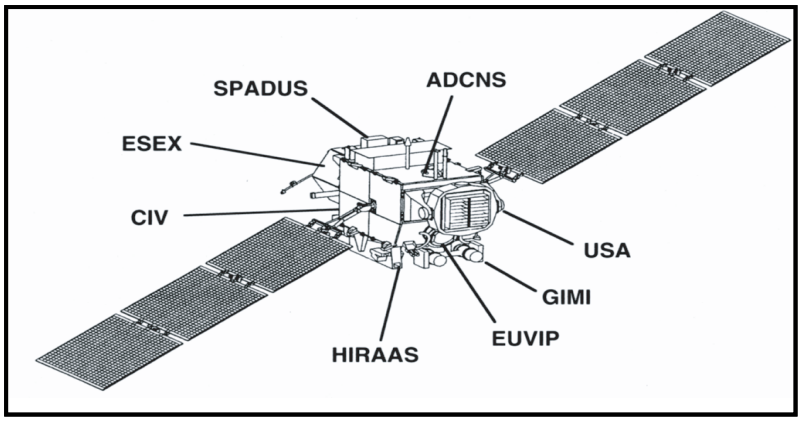

Figure 3.3 Positioning of the USA experiment aboard the ARGOS satellite.

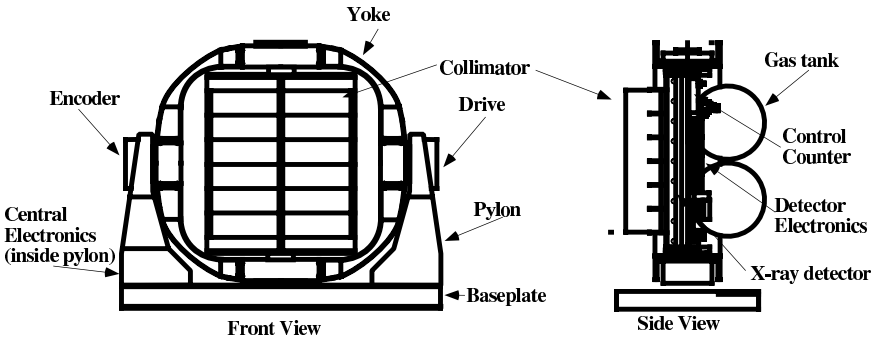

Figure 3.4 Drawing of the USA instrument showing the two detectors mounted on the yoke and pylons, left the instrument seen from the front, right seen from the side.

calculate the fraction of obscuration by the yoke.

USA Electronics

The USA detector electronics local to the detector itself has the following functionality: amplify the signal, convert the analog output of the chamber to a digital signal (ADC), determine the PHA channel and layer identification (top or bottom). After performing these operations, the data are transferred to the detector interface board located in the central command and control electronics. The central command and

control electronics is a Harris radiation hardened 80C86 microprocessor whose purpose is to interface the ARGOS spacecraft, control the pointing system, interface the USA's RH3000 and IDT3081 processors and handle data acquisition from these modules. The detector interface board on the central command and control electronics performs the actual time tagging and formats the X-ray science and housekeeping data for telemetry. More information on how this time tagging is performed can be found in Appendix A. Information on the USA electronics is available in Ray et al. (2001) and, Shabad (2000).

In the amplification electronics or the ADC there is a pileup effect that causes the energy of an incoming event to be affected by the energy of the previous event and the time from the previous event. This is not fully understood, but the problem manifests itself as an energy dependent instrumental effect (EDIE). EDIE appears in power spectral density distributions (PSD). EDIE will turn a flat PSD into one that has a *bump* at ~ 400 Hz. The shape and intensity of the *bump* is affected by energy cuts on the data, and the shape of the source's energy spectrum. EDIE has caused a problem in the range of 200–600 Hz when analyzing PSD data for broad features in all USA sources with a relatively soft energy spectrum. The Crab and Cygnus X-1 are examples of sources whose data are not affected as long as no energy cuts are made on the X-ray energy. A detailed description of EDIE is given in Reilly (2002).

3.1.3 GPS and USA

Introduction

The USA instrument is equipped with a Global Positioning System (GPS) receiver that was designed to allow the instrument to have microsecond absolute time resolution throughout an observation, and from observation to observation. This feature is particularly useful in timing pulsars through several observations. The USA GPS receiver, built by Boeing (then Rockwell International), has an anomaly that causes it to drop out of lock after a few hours. This section describes the problem and the existing solutions.

General GPS Operation

GPS consists of three main components, the satellite (SV) component, the ground based Control Segment, and the User Segment or receiver. We provide here a summary of the material presented in reference Dana (1994).

Space Segment GPS is a constellation of at least 24 satellites that orbit the Earth in 12 hours. There are often more than 24 operating satellites available as new ones are launched to replace older units. Each SV has a life expectancy of 7.5 years. The GPS SVs orbit such that they repeat the same track and configuration over any point on Earth approximately every 24 hours. There are six orbital planes, equally spaced and inclined about 55° with respect to the equatorial plane. The SVs orbit at an altitude of 10,900 nautical miles. This constellation provides a ground based user with between five and 8 SVs visible from any point on the Earth. The constellation is illustrated in Fig. 3.5.

GPS is funded and controlled by the U.S. Department of Defense (DOD). The system was designed for and is operated by the US military. The GPS signals contain specially coded satellite signals that can be processed in a hand held receiver. Four GPS SVs are used to compute the position and velocity in three dimensions and the time offset in the receiver clock. Each SV contains four atomic clocks, two cesium and two rubidium.

Control Segment There are ground based monitor stations for GPS that measure signals from the SVs which are incorporated into orbital models for each satellite. These models are used to calculate the ephemeris of each satellite and SV clock corrections. The Master Control station, located at Schriever Air Force Base in Colorado, uploads the ephemeris and clock data to the SVs. Subsets of this information are then sent with the GPS signal to the receivers. Ground stations also monitor SV clocks and occasionally reset the SV clock to maintain time within one-millisecond of GPS time. See Appendix A for the description of GPS time.

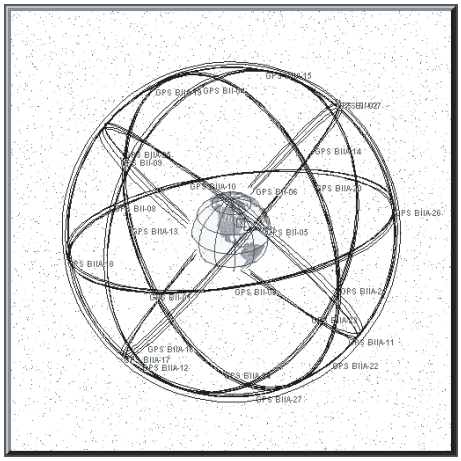

Figure 3.5 Cartoon showing the GPS Constellation orbits. Nominal constellation is 24 satellites in six orbital planes with four satellites in each plane. Satellites orbit at 20,200 km altitude with a 55° inclination.

User Segment The User Segment consists of the GPS receivers and the user community. GPS receivers can calculate time, position and velocity. Receivers are used for navigation, positioning, timing and other research. Four signals from four SVs are necessary to get position and time information. Since each GPS SV has atomic clocks onboard, and each GPS receiver gets its time information from the GPS SV, each receiver is nearly as accurate as an atomic clock. More precise positioning can be achieved using a GPS receiver at a reference location. This reference location is usually land based, but it could also be a satellite in a geosynchronous orbit. Using the reference location a Differential GPS (DGPS) signal can be computed for sub -meter accuracies.

GPS Accuracies Civil users worldwide use GPS for the Standard Positioning Service (SPS) without charge or restriction. The SPS accuracy is usually intentionally degraded by the DOD using Selective Availability (SA). SA was turned off by the DOD on 2000 May 02. The SPS 95% accuracy is:

- 100 meter horizontal accuracy
- 156 meter vertical accuracy

- 340 nanosecond time accuracy

Authorized users with cryptographic equipment and keys and specially equipped receivers use the Precise Positioning System (PPS). U.S. and Allied military, along with certain users approved by the U.S. government can use PPS. The PPS 95% accuracy is:

- 22 meter horizontal accuracy
- 27.7 meter vertical accuracy
- 200 nanosecond (UTC) accuracy (see Appendix A for a description of UTC)

The use of a reference receiver in addition to the measured receiver can lower the limits even further and can allow civil users to take out the SA errors. DGPS accuracies can be:

- positioning to < 1 meter for stationary applications.
- positioning to < 5 meters for moving applications.

GPS Data The SVs transmit two microwave carrier signals. The L1 frequency, 1575.42 MHz, carries the navigation message and the SPS Signal. The L2 frequency, 1227.60 MHz, is used to measure the ionospheric delay by PPS receivers. The data signal is a 50 Hz signal on top of these carriers mixed with a 1.023 MHz pseudo random noise (PRN) signal that uniquely identifies the GPS SV.

The GPS navigation message consists of time-tagged data bits marking the time of transmission of each subframe. A data frame is transmitted every thirty seconds in five six-second subframes. SV clock corrections are sent in subframe one, and precise ephemeris information is sent in subframes two and three. Subframes four and five transmit different pages of system data. It takes an entire set of twenty-five frames (125 subframes) to give a complete Navigation Message that is sent over 12.5 minutes.

The complete SV data set includes a ten parameter almanac that describes the orbit of the SV. This orbit data is used to preset the receiver with the approximate position and carrier Doppler frequency of each SV in the constellation. Each complete

data set also includes an ionospheric model the reciver uses to calculate the phase delay through the ionosphere. The SV sends the amount of time GPS is offset from UTC. This correction can be used by the receiver to set UTC within 100 ns.

Calculating Receiver Position, Velocity, and Time Four satellites are used to determine three position dimensions and time. Position dimensions are computed by the receiver in Earth-centered, Earth-Fixed X, Y, Z (ECEF XYZ) coordinates. Time from GPS is used to correct the offset in the receiver clock. The receiver position is computed from the GPS SV positions, the measured pseudo-ranges (corrected for SV clock offsets, ionospheric delays and relativistic effects), and a receiver position estimate. The receiver position estimate is usually the last computed receiver position, or an estimate based on last position and last computed velocity. Five or more SVs can be used to give time and position redundancy. More SVs can allow detection of out-of-tolerance signals under certain circumstances. Velocity is computed from change in position over time, Doppler frequencies or both. Time is computed in SV time, GPS time and UTC (see Appendix A).

SV time is set in the receiver from the GPS signals. Data bit subframes occur every six seconds and contain information to resolve the time of week to within six seconds. The arrival time of a data bit edge is on a 50 Hz data bit stream. Using the approximate range to the SV resolves the twenty millisecond ambiguity. Multiple SVs and a navigation solution (or a known receiver position) permit the SV time to be set to an accuracy limited by the position error and the pseudo-range error for the SV. SV Time is converted to GPS Time and UTC time in the receiver. GPS Time is measured in weeks and seconds from 1980 January 5 24:00:00. GPS is kept within one microsecond of UTC before leap seconds. GPS Time does not include leap seconds, UTC does include leap seconds. Therefore GPS time is ahead of UTC by several integer seconds. More information on time systems can be found in Appendix A.

GPS Error Sources GPS errors are a combination of noise, bias and blunders.

- Noise errors are the combined effect of Pseudo-Range Navigation code noise ($\sim$ 1 meter) and noise within the receiver ($\sim$ 1 meter).

- Bias errors result from:
  - SA degradation. This reduces the accuracy from around 30 meters to 100 meters. SA degredation was turned off 2000 May 02.
  - SV clock errors uncorrected by control segment ($\sim$ 1 meter).
  - Ephemeris data errors ($\sim$ 1 meter).
  - Tropospheric delays ($\sim$ 1 meter).
  - Unmodeled ionospheric delays ($\sim$ 10 meters).
  - Multipath or reflected signals to the receiver ($\sim$ 0.5 meter).
- Blunders can give errors of hundreds of kilometers.
  - Control segment mistakes ($\sim$ 1–100,000 meters).
  - User mistakes, usually in Datum selection for latitude and longitude ($\sim$ 1–100 meters).
  - Receiver errors hardware/software can cause errors of any size.
- Noise and bias errors, combine and result in typical errors of around 15 meters for each SV used in the position solution.

Differential GPS Techniques Differential GPS techniques involve correcting bias errors at an unknown location using measured bias errors at a known location. This requires a well known reference receiver to be accessible by the unknown receiver. The US Coast Guard (USCG) maintains a network of differential monitors and transmits DGPS corrections over radio frequencies covering much of the US coastline. Corrections can also be recorded for post-processing if the position is not needed in real time. The FAA maintains DGPS monitors near airports for using DGPS during aircraft take-off and landing. The FAA is also researching the feasibility of using geosynchronous satellites as DGPS monitors, therefore covering the entire US or World with a DGPS signal.

DGPS removes all common mode errors, including the SA degradation. DGPS works best when the reference and unknown receiver are close together. After using

DGPS the only errors remaining are multipath and receiver errors. DGPS can give absolute positions of 1–10 meters. Using phase differences relative positions can be achieved in the centimeter range. For this accuracy the monitor and unknown receiver must be close enough to ensure the ionospheric delay is less than one carrier wavelength. This means the two stations must be within about 30 kilometers.

GPS operation on the ARGOS Satellite

The GPS receiver on ARGOS is a five-channel receiver built by Rockwell International (Now Boeing). It employs the civilian coding, so it is subject to the SA degradation. The accuracy of the receiver should be $\sim$ 100 meters in position and $\sim$ 200 ns in timing.

The GPS receiver measures its performance by a single figure of merit (FOM). The FOM varies from one meaning converged solution achieving full accuracy and nine which means no solution. On ARGOS a solution is accepted as "good" and is used by navigation software when FOM is less than five. The GPS receiver gets a GPS position estimate each second from the GPS SVs. It then applies a Kalman filter to propagate it's own position to predict where it will be at the next second. The comparison between this predicted value and the measured value is the basis for the FOM.

There was a design error that caused problems operating the GPS receiver for certain geometries. The designers of the receiver had concerns that under certain worst case scenarios the GPS signal would be too small for the receiver. To counter this, they designed for all worst case scenarios and gave the receiver a very high non-adjustable gain. However, in practice, none of these worst case scenarios was present. Therefore, sometimes the GPS signal is larger than expected, causing the receiver to pick up a sidelobe of the main GPS signal rather than the global maximum. This causes an incorrect PRN measurement from one or more GPS SVs. The PRN ensures the receiver is looking at the correct code, not the code before or after. Looking at the wrong code gives a navigation error of 300 km corresponding to a PRN code length of 1 ms. This causes a poor position and time estimate on the ARGOS receiver. Sometimes, this is recoverable as ARGOS moves with respect to

the GPS constellations. However, sometimes the predicted solution is sufficiently far off such that the receiver is too confused to calculate its position and predict a position for the next fix. When this occurs the receiver drops out until it is reinitialized with a good state vector from the ARGOS ground monitoring stations. A new state vector is sent to ARGOS from the ground every 6 hours. This particular receiver configuration has no independent means of recovering a good solution once it has lost its ability to predict the position of the next fix to an acceptable accuracy. When the GPS receiver is not initialized the timing accuracy is determined by the accuracy of the initialization vector sent to the spacecraft clock and the drift rate of the spacecraft clock (~ 1 μs/10 s).

GPS Calibration and Epochs Between USA initialization on 1999 May 01 and 1999 August 18 the GPS receiver was rarely initialized. During this time the ARGOS flight software (FACP) trusted the GPS receiver implicitly and GPS initializations were considered dangerous. Early in the mission a GPS solution wandered off causing ARGOS to go into Sunsafe Mode and the solar panels to point away from the Sun. During this period, when initializations did occur, the receiver introduced 13 second jumps up to 25 minutes after each initialization. These jumps were caused by the GPS receiver incorrectly applying leap second corrections when converting between GPS and UTC (see Appendix A).

Between 1999 August 18 and 1999 August 20 USA was off while new ARGOS flight software was uploaded to deal with some of the GPS receiver problems. The important changes were:

- The ARGOS Attitude Determination and Control System (ADACS) was modified to always ignore positions output by the GPS receiver. Positions from this point onward were determined solely by an orbit propagator started with the state vector at each six hour GPS initialization. Therefore, from 1999 August 20–on all position information from the GPS were ignored: it was only a timing device.

- The time processing software was modified to fix the leap second jump irregularities. From this point on the leap second corrections were done by the flight software rather than the GPS receiver. From 1999 August 20 ARGOS used the GPS receiver when the GPS FOM was less than five. When the GPS time was unusable, ARGOS incremented the time by one second per spacecraft clock tick. The spacecraft clock was good to about one part in 10^7.

- Changes were also made to allow more accurate initializations of the GPS receiver and propagator.

- Operational changes were made to initialize the GPS receiver and propagator four times per day (over the North Pole at approximately six-hour intervals).

USA Timing Accuracy There are basically five levels of accuracy in the *uncorrected* USA photon event times:

- **No GPS Init (pre 1999 August 18)** During this time the GPS receiver and onboard propagator were not regularly initialized. The absolute time accuracy is poor; no better than a few seconds.

- **Failed GPS Init** When a normal GPS init occurs, but the GPS receiver fails to achieve lock, time is never set to GPS time and the timing accuracy will be that of the init plus a slow drift from the inaccuracy of the spacecraft clock. The accuracy during failed inits has not been calibrated but is likely $\lesssim$1 s. This may be calibrated better in future, but currently data after a failed GPS init should not be used for precise timing.

- **GPS in lock** While the GPS receiver is in lock, the spacecraft time is defined by the GPS receiver. The timing accuracy should be better than 1 μs but in practice, jumps of tens of microseconds are observed due to the spurious cross-correlation problems in the receiver.

- **GPS Dropped Out** After the GPS has been in lock and then dropped out, time will continue to be incremented by one second per spacecraft clock tick.

The timing error will grow at a rate of about 1 μs/10 s until the next init. This means the maximum timing error should be about 1 μs/10 s $\times$ 6 hours $\lesssim$ 2 milliseconds.

GPS Post Processing Corrections In consultation with the USA team, Boeing engineers developed a post-processing tool (P91GPSLS) to correct times on the ground and provide timing accuracy close to what had been promised for the GPS receiver. This tool takes data from one GPS init to the next. It applies several filters based on receiver parameters and timing performance to fit a true time vs. spacecraft time model. This model is used to extrapolate from when the GPS was locked on through after the GPS has dropped out of lock. Temperature dependent drifts in the clock rate are compensated for. The output is a table of corrected times vs. spacecraft times that can be used to correct USA event times. This tool can only correct times that occur after the GPS achieves first lock and subsequently drops out before the next init. It does not apply if the GPS fails to achieve first lock. There is also a gap of a few hundred seconds between the GPS receiving an init and the receiver achieving a lock, the tool does not apply during this gap. Thus, about 80% of the times in the USA data are correctable. This correction is applied by choosing *Boeing corrected times* in *picktelemII* when creating the data FITS files. See §3.1.4 for more information on using *picktelemII*.

Conclusions

GPS is designed to provide users a relatively inexpensive means of accurate positioning and timing in various applications. The GPS receiver on the ARGOS satellite was designed to provide position and sub-microsecond timing without any need for post-processing. However, due to design problems, the data from the receiver contains errors. Most of the errors can be removed by post-processing the data on the ground. Studies are continuing to ensure the validity of these corrections and extend the corrections to a larger data set.

At present, for observations over several days, with no postprocessing corrections, the residuals between the USA Crab Pulsar pulse time of arrival (TOA) data and

the Jodrell Crab ephemeris are less than 300 μs (Ray et al. 2003). Thus, the current USA FITS files are usable for all but the most demanding timing applications. The implementation of post-processing corrections to the event times (done by hand at this point) reduce these errors to ~ 30 μs. This is at the level where comparison with the radio ephemeris becomes difficult. The radio ephemeris has an RMS of 60 μs and an uncertainty in the extrapolation to infinite (i.e. X-ray) frequency due to secular changes in the dispersion measure to the Crab Pulsar that are not measured perfectly.

3.1.4 USA Data

USA Standard Data Modes

USA operated in five science-telemetry modes summarized in Table 3.1. There are four event modes (1–4) and one spectral mode (5). Each event mode contains information about individual X-ray photons with bits allocated for a time stamp, PHA channel, detector ID[2], and layer ID. The timing resolution and number of PHA channels vary for each event mode. Table 3.1 gives information on the maximum counting rate available in each mode. The rate is limited in the event modes by the telemetry rate constraints limiting the number of events a given mode can store in each one s frame. The events are distributed according to Poisson process in each one s frame, therefore they are not evenly distributed, so the actual maximum observed rate is lower than the maximum number of events that can be held in one frame. Table 3.1 gives an approximate highest count rate that can be observed in each mode. This value was obtained by simulating USA science frame packing assuming a Poisson distribution of incoming events (Shabad 2000). If the observed rate becomes too high in a particular frame and the amount of data exceeds the amount that can be held in that particular frame, the frame will be truncated and the rest of the data in that frame will be lost. This will result in a gap in the science data, and an entry in the event good time interval (GTI) table informing the user that this gap occurred. The spectral mode data are binned and can hold all the events up to the maximum

[2]For all data analyzed in this dissertation, only detector 1 was used. Detector 2 was damaged very early in the USA mission.

Table 3.1. Summary of the USA Science Data Modes

Mode Num.	Mode Type	Time Res.	Spectral Channels	Bits per Event	Layer ID	Telemetry Rate [kbps]	Maximum events per frame	Maximum Poisson Rate [cts s^{-1}]
1	event	32 μs	16	12	yes	40	3060	~1350
2	event	32 μs	16	12	yes	128	9940	~8000
3	event	2 μs	8	15	yes	40	2448	~1100
4	event	2 μs	8	15	yes	128	7952	~6500
5	binned spectral	10 ms	48	192 per spectrum	no	40	10000	~10000[a]

[a]This value is the maximum count rate for one USA detector. Nearly all of the USA data were taken with only detector 1 functioning.

incident counting rate allowed in USA, 10,000 cts s^{-1} in one detector (Shabad 2000; Ray et al. 2001).

USA Data Selection and Processing

The USA science working group (SWG) has created a user friendly fairly automated way to extract USA data. The USA data are stored in a level one database at NRL, and until recently mirrored at SLAC. This database is accessed using the program *picktelemII*. *PicktelemII* allows the user to browse the level 1 archive and search for all observations for a particular source. In addition, the user can sort, and select observations based on various criteria. Usually, one will select observations based on yaw angle, percent archived (normally 100% for all observations), average count rate, Dt%[3], and observation vector. The observation vector tells the user whether the satellite was moving from the south to the north (ascending) or north to south (descending) during the observation. The observation vector is important for energy analysis, as the ascending and descending observations have different energy calibrations and require different response matrices (Saz Parkinson 2003). One can use *picktelemII* to visually select data within a particular observation also. This feature is useful when

[3]Dt% is the percentage of time the detector is on.

an accurate background measurement is needed as one can select the data at the beginning of the observation before the detector pointed on-source. One–two minutes of off-source observation was always performed before pointing on-source. After selecting the data in *picktelemII* the program calls *dat2fits* which converts the data from the archive into useable flexible image transport system files (FITS) (Hanisch et al. 2001).

Once the FITS files have been created, one containing science information and one containing housekeeping information for each observation of interest, then the background can be estimated. The program *usabckgnd* uses information from the perimeter and coincidence veto rates (§3.1.2), satellite (SV) position and other information to estimate the background rate and spectrum for the instrument. This program is usually run using the *mkbckusa* script. *Usabckgnd* will create a FITS file containing a binned background science file. This background model was created by Dr. Michael Wolff at NRL, and further details can be found in Saz Parkinson (2003).

After creating the background files for each observation of interest, the USA data were filtered to ensure that the data used in analysis were free of most obvious systematic instrumental problems, and filtered in such a way as to be repeatable for other observers. The *MkTimeUSA* program accessed via the *mktimeusa* script is used for this type of filtering. The *mktimeusa* script takes an input file containing the cuts you wish to place on the data, this allows for consistent and repeatable cuts. Some output of this script include new FITS science and background files that have events removed that failed the cuts and a new GTI table in these FITS files incorporating the cuts, and a *STAT* file for each observation described below. There are other output from *mktimeusa* and the interested reader can see Reilly (2002) for more information. Any analysis involving timing or spectral work should be performed using these filtered FITS files produced from *mktimeusa*.

The *STAT* files are text files that contain information from the science and background filtered FITS files binned every second. The counting rate for each PHA channel and each layer, both of science and background are included. In addition, information about the collimator and yoke corrections are given for each second. The

STAT files make it easy to create a one s binned light curve of the observations corrected for background and any collimator and yoke obstruction. The corrected light curve is:

$$\mathrm{Rate}_{\mathrm{corrected}} = \frac{\mathrm{Rate}^{\mathrm{meas}}{}_{ij} - \mathrm{Rate}^{\mathrm{bck}}{}_{ij}}{\mathrm{C}_{\mathrm{coll}} \cdot \mathrm{C}_{\mathrm{yoke}}} \tag{3.1}$$

where the PHA channels and detector layers of interest are summed over ij and $\mathrm{C}_{\mathrm{coll}}$ and $\mathrm{C}_{\mathrm{yoke}}$ are the corrections for the collimator and yoke obscuration. We found that these corrections are not very reliable when $\mathrm{C}_{\mathrm{yoke}} \lesssim 25\%$ or $\mathrm{C}_{\mathrm{coll}} \lesssim 40\%$.

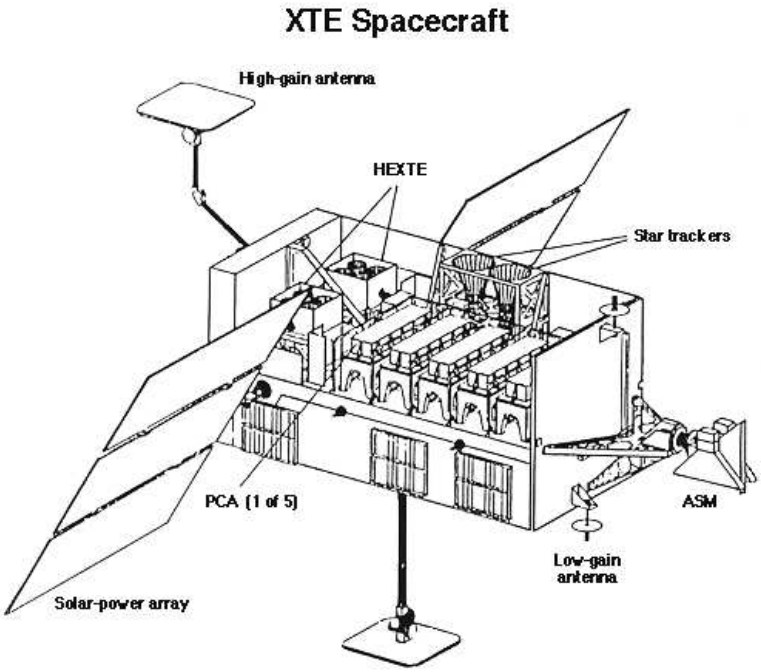

Figure 3.6 The RXTE satellite and its different instruments.

3.2 The Rossi X-ray Timing Explorer

3.2.1 RXTE Hardware

The Rossi X-ray Timing Explorer (RXTE) experiment is an X-ray satellite that was launched in 1995 December. The spacecraft (SV) is in a low Earth orbit, and completes about fourteen orbits per day. RXTE is composed of three instruments: the Proportional counter array (PCA), the high energy X-ray timing experiment (HEXTE) and the all sky monitor (ASM), Figure 3.6. The PCA is effective over the range 2–60 keV. The HEXTE instrument consists of two detectors that cover the energy range 20–250 keV. The ASM has three detectors sensitive in the 2–10 keV range and rotates to take $\sim$ 90 s exposure on $\sim$ 75 sources several times daily (Bradt, Rothschild, & Swank 1993; Focke 1998; Jahoda et al. 1996).

PCA

The PCA consists of five essentially identical Proportional Counter Units (PCUs). Each PCU has an area of $\sim 125 \times 25$ cm, giving a total physical area of 15,625 cm^2, with a peak effective area of 7000 cm^2. The PCA is a pointed timing and spectral instrument, collimated by a hexagonal beryllium/copper grid giving a 1° (FWHM) field of view (FOV).

The PCA is effective over the energy range 2–60 keV, with detection up to 100 keV. The energy resolution is 18% at 6 keV and 9% at 22 keV. The spectral information is recorded by a 256-channel Pulse Height Analyzer (PHA) per PCU. The energy resolution is determined by the physics of the detection processes within the gas in the proportional counter (counting statistics on the number of secondary and tertiary electrons).

Events are tagged to a precision of 2^{-20} s (slightly better than 1 μs), allowing high time resolution for events in different PCUs (Focke 1998; Jahoda et al. 1996).

The PCU gas chambers are filled with xenon and 10% methane. The anodes and cathodes are gold-coated stainless steel wires. There are several veto methods built into the PCU design to help reject charged particle events (primarily energetic electrons trapped in the Van Allen belts and cosmic rays). First, there is a 1.3 cm thick propane volume above each PCU with a single layer of anodes. Charged particles entering the propane will cause charge cascades which will be collected on the anodes. X-rays above 2 keV are not likely to interact in this propane layer, therefore the acceptance of the detector is not adversely affected. Second, the anodes in the detector that are adjacent to the back and sides of the chamber are dedicated for use as a veto layer. Third, the detector is composed of cells made up of squares of cathodes with an anode in the center interleaved throughout the chamber. When X-rays are absorbed by the gas, they usually impart all of their energy to a single electron, which then transfers it to nearby electrons. It is unlikely any of these electrons will escape one detector cell and go into another. However, this is likely for an energetic particle entering the detector leaving a trail of ionization. Therefore, if an event triggers multiple cells it is vetoed (Focke 1998).

ASM

The All Sky Monitor (ASM) is designed to monitor the entire sky for early alerts of transient phenomena in addition to continuous monitoring of brighter X-ray sources. The ASM provides coverage of 80% of the sky every 90 minutes. The ASM has 90 s dwells in a particlar position then looks at a different position. A given source will have typically 5–10 dwells per day.

The ASM consists of three scanning cameras, each with an eight-wire position sensitive xenon proportional counter. The total collecting area is 90 cm^2. The cameras have a $90° \times 6°$ FOV, and use the position sensitivity with a shadow mask to provide source distinction. The ASM can determine the location of a bright source to a position of $3' \times 15'$ and $0.2° \times 1°$ for weak sources. The ASM is sensitive to sources at least 30 milliCrab[4] (Focke 1998).

The ASM has three energy channels for rough spectral analysis in the energy range 2–10 keV.

HEXTE

The High Energy X-ray Timing Experiment (HEXTE) consists of two clusters each containing four phoswich scintillation detectors. Each cluster can "rock" (beam-switch) along mutually orthogonal directions to provide background measurements 1.5 or 3.0 degrees away from the source every 16 to 128 s. The instrument covers the 20–250 keV range with 15% energy resolution at 60 keV. The clusters sit behind a lead hexagonal grid giving a 1° FOV with a net area of 1600 cm^2.

The on-source dwells are alternated with dwells on either side, interleaved so that there is always one cluster on-source. Dwell times of 16, 32, 64, or 128 s may be selected, with 32 s being recommended. The actual rocking motion takes two s and occurs during the off-source portion of the cycle. Therefore, if using a 32 s dwell time, the entire cycle length is 128 s with 64 s on-source, 28 s on each background position and eight s slewing (Focke 1998).

[4]The Crab nebula is often used as a calibration source in X-ray astronomy. The flux density and spectrum are known to be constant. The flux of one milliCrab in the 2–10 keV range is $\approx 2.8 \times 10^{-11}$ ergs cm^{-2} s^{-1}.

The phoswich detectors are crystal scintillation detectors made by sandwiching two crystals with different pulse rise times. The front crystal has a faster rise time and absorbs the X-rays in the energy range of interest. Then the light passes through the back crystal to a photomultiplier tube. Electrons entering the detector through the collimator, or photons that are not completely absorbed in the first crystal will deposit energy in both crystals. The presence of the longer pulse from the back crystal is used to veto these events. In addition to this veto method, each detector cluster is surrounded by flat plastic scintillators. These scintillators are used as anti-coincidence triggers to veto particles entering the detector from the side.

3.2.2 RXTE Data

Analysis of RXTE data requires a thorough understanding of the types of RXTE data available and the information contained in each type. A single RXTE observation will have several data modes, producing several FITS files for each observation, each one with different types of information. In this section I will walk through the process of obtaining the RXTE data and generic steps to perform analysis. More detailed information is available in the *RXTE Cookbook*[5].

Downloading RXTE Data

Data from RXTE are kept proprietary for the investigators that submitted the proposal for one year from the date of receipt of data by the PI. The RXTE science observer facility team (SOF) will email the PI after processing the data in a proposal with instructions on how to obtain the files via FTP. The files are compressed with a security code that the SOF gives the PI, and the PI uses to decode the data. Target of opportunity (TOO) data become public as soon as they are processed. After data become public, the data are controlled by the RXTE guest observer facility team (GOF). The GOF will make the data available from the HEASARC website[6], or anonymous ftp to ftp://legacy.gsfc.nasa.gov/ where the RXTE data are located

[5]http://heasarc.gsfc.nasa.gov/docs/xte/recipes/cook_book.html
[6]http://heasarc.gsfc.nasa.gov/db-perl/W3Browse/w3basic.pl

in /xte/data/archive/AO*N*/*Proposal ID*/*obs. ID*. Where AO*N* refers to the N^{th} observing cycle, *Proposal ID* is the ID unique for each proposal, and *obs. ID* is an ID for a given observation in the proposal. The proposal ID and observation ID can be obtained by searching at the HEASARC website. Obtaining data via the website is the most efficient method if you are sure to only download data in groups of about twenty observations at a time.

After downloading and unpacking the data, you will have a proposal directory PNNNNN (NNNNN is the proposal number), below which you will have directories for each individual observation NNNNN_01 etc. You should create a new FMI file. The FMI file is the index that FTOOLS (Blackburn, Greene, & Pence 1993) use to know what observations and what files exist in subdirectories. To create a new FMI file in the proposal directory, copy an FMI file from any observation directory into the proposal directory. Then type the command *recofmi dirpath=PNNNNN delete=yes*. If you have FTOOLS properly installed on your system, this command should be recognized and rebuild the FMI file in the proposal directory.

Making sense of the RXTE FITS files

A single observation directory will contain a subdirectory for each spacecraft subsystem. The only ones that we need to be concerned with are:

hexte HEXTE science and housekeeping data

orbit Orbit ephemeris from the Flight Dynamics Facility

pca PCA science and housekeeping data

stdprod Standard products — cleaned light curves, spectra etc.

The Standard Products Data are collected in standard modes for every PCA and HEXTE observation. The PCA has two standard modes. *Standard 1* data are binned in 0.125 s intervals and contain no energy information, the count rates are normalized to 1 PCA module, as there may be different numbers on for different observations. *Standard 2* data are binned in 16.0 s intervals with 129 PHA channel (0–128) energy

Table 3.2. Description of RXTE Standard Products

Filename[7]	**Description**
	PCA
xpObsId_**M2B**.lc	16 s source, background and net light curves in five bands **B** = a,b,c,d,e where a = 2–9 keV b = 2–4 keV c = 4–9 keV d = 9–20 keV e = 20–40 keV
xpObsId_n1.lc	0.125 second net light curve, all channels
xpObsId_**M2**.pha xpObsId.rsp	Source and background Standard2 spectra Corresponding response matrix
	HEXTE
xhObsId_**MCB**.lc	128 s source, background, and net light curves in three bands: **C** = cluster 0(A) or 1(B) **B** = a,b,c where a = 15–30 keV b = 30–60 keV c = 60–250 keV
xhObsId_**MC**.pha	Archive mode spectra for source and background, both clusters.

information. The HEXTE standard mode data are binned in 128 s intervals with 129 spectral channels. Table 3.2 explains the files that are found in the *stdprods* directory. The FH* files are housekeeping and can be ignored, the *gifs* directory contains GIF images of each of the standard products described in Table 3.2.

Table 3.2—Continued

xh*pwa.rmf	.RMF file for spectral analysis; Cluster 0 (A)
xh*pwb013.rmf	.RMF file for spectral analysis; Cluster 1 (B)
hexte*.arf	.ARF files for spectral analysis of both clusters
Miscellaneous Products	
xObsId.gti	Good Time Interval file used in the data extraction
xObsId.xfl	RXTE Filter File; attitude and HK parameters versus time

[a]**M** refers to s(source), b(background), or n(net) in all instances.

Other RXTE Data Modes The FITS files in the PCA and HEXTE directories contain all the science files one should need to analyze. The files are named with the following convention FS4* refers to a science FITS file for the PCA. FH4* refers to a PCA housekeeping file. FS5* and FH5* are the science and housekeeping FITS files for HEXTE. The standard modes are taken for every observation. In addition, the PI specifies other modes that can be used to observe with. In order to see what data mode a particular science file was created with type *fkeyprint <science filename>[1] datamode*. This command will return the data mode of the FITS file. Common data modes are summarized in Table 3.3, more details on the data modes can be found in (RXTE Team 1995).

Basic RXTE Data Reduction Detailed instructions for analyzing RXTE data are found in the *RXTE Cookbook*[6], here I present a shortened outline of the most common steps involved in analysis.

- Create a Filter file. This is done by running *xtefilt*. This step merely creates a file with all the information that will be used to make cuts on the data.

Table 3.3. Description of Common RXTE Data Modes

Standard Products	
Standard 2f	129 channel spectra every 16 s.
Standard 1	0.125 s. binned light curve
Binned Modes	
B_ttt_ccx_ll_hh_A	ttt — time bin size cc — number of energy bins x — binning configuration ll — lower energy channel hh — upper energy channel A — bits per bin code
Single Bit Modes	
SB_ttt_ll_hh_rr	ttt — time bin size ll — lower energy channel hh — upper energy channel rr — readout time
Event Modes	
E_ttt_ccx_ll_rr	ttt — time resolution cc — number of energy bins x — binning configuration ll — lower energy channel rr — readout time
Good Xenon Modes	
Good_XenonX_rr	X — either file 1 or 2 rr — readout time

- Combine Good Xenon files. If you are analyzing Good Xenon data mode data, then you will need to perform this step. Two Good Xenon files are created for each observation due to hardware constraints, but they should be analyzed as a single file.

- Create a Good GTI file. This step uses the information in the filter file to create a list of times that contain data that survived the cuts. In this step, you define the cuts to be placed on the data, minimum number of PCU's to be operating, maximum offset etc.

- Estimate the Background. This is accomplished using *pcabackest* and is a continually updated process. You should consult the *RXTE Cookbook* for the latest information on running *pcabackest*.

- Create Light curves and PHA files for both HEXTE and PCA science and background data. At this stage you are ready to create light curves and energy PHA files from your filtered data.

- Correct for deadtime. Deadtime exceeds 1% when the count rate per PCU exceeds 1000 cts s^{-1}. The *RXTE Cookbook* gives a recipe for this correction. No deadtime corrections were applied in my analysis, time ranges where deadtime would be an issue were not studied. Deadtime corrections only affect high-precision timing; for precision timing analysis I analyzed USA data.

- Create response matrices. *Pcarsp* is the program use to create response matrices. They must be matched for the PHA channels used and the epoch of the experiment.

- Barycenter the light curves. If you are doing timing analysis of pulsar data, this is where you would use *faxbary* to barycenter your light curves.

These are the basic steps needed to perform analysis on RXTE data. At this stage, various other FTOOLS are used to analyze the timing and spectral data you have just created. You may run XSPEC (Dorman & Arnaud 2001) to analyze the PHA files for spectral information. We found it often necessary to use the HEXTE background

PHA files as a background PHA file *and* as a correction file for additional subtraction. The HEXTE background was under-subtracted for most of our observations. You may also perform timing analysis such as epoch-folding and making power density spectra with the light curves you have created.

3.3 GLAST

3.3.1 Description of the GLAST Experiment

The Gamma Ray Large Area Space Telescope (GLAST) is a satellite based, gamma ray pair conversion telescope to be launched in 2006 (Michelson 1996; Atwood 1994). Figure 3.7 shows an artist's conception of the satellite. The principal objectives of the GLAST mission involve the observation of energetic gamma rays, starting at 20 MeV and extending to $\sim$ 300 GeV (Michelson 1996; Atwood 1994). Observational data in this range are limited. In the past, gas chamber detectors were used. GLAST will employ 74 m^2 of silicon microstrip detectors to probe this energy regime. Silicon detectors offer better response, higher resolution, shorter dead time, and more robustness over gas detectors. The GLAST Large Area Telescope (LAT) will provide overlap (20 MeV to 300 GeV) between satellite observations and ground–based telescopes. It will offer tremendous opportunity for discovery in high–energy astrophysics by probing these systems with >30 times better sensitivity than the previous gamma-ray telescope, the energetic gamma-ray experiment telescope (EGRET). In addition to the LAT, GLAST will employ a very wide Field of View (FOV) instrument, the gamma-ray burst monitor (GBM), to detect gamma ray bursts and allow the LAT to be re-pointed to gather information on the delayed high-energy emission. Table 3.4 details some of the important science parameters of the GLAST mission.

The LAT instrument will be made up of 16 individual towers of silicon detectors. Each tower will have a CsI calorimeter beneath it and the entire telescope will be covered with an Anti-Coincidence Detector (ACD). Figure 3.8 shows an artist's conception of the LAT.

Silicon Tracker

The LAT tracker consists of a 4×4 array of silicon modules. Each module is composed of nineteen pairs of planes of silicon — in each pair, one plane has the strips oriented in the 'x-direction', while the other has the strips oriented in the perpendicular 'y-direction'. When a particle interacts in the silicon, its position on the plane can

Figure 3.7 Artist's conception of GLAST satellite instrument. Figure courtesy Spectrum Astro.

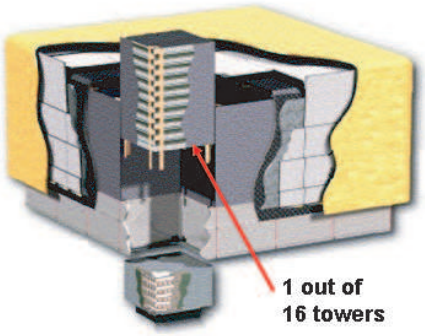

Figure 3.8 Artist's conception of GLAST Silicon Tracker. Figure courtesy of Hytec.

Table 3.4. Science Parameters of GLAST

Parameter	Value
Tracker	
Effective Area	> 300 cm^2 @ 20 MeV > 3000 cm^2 @ 100 MeV > 6400 cm^2 @ 300 GeV > 8000 cm^2 peak
Energy Resolution	$\leq 50\%$ (20 – 100 MeV) $\leq 10\%$ (100 – 10 GeV) $\leq 20\%$ (10 GeV – 300 GeV) $\leq 6\%$ (Energy > 10 GeV, incidence $> 60°$)
Angular Resolution (1 σ on-axis)	$< 3.5°$ front, $< 6°$ back @ 100 MeV $< 0.15°$ front, $< 0.3°$ back @ 10 – 100 GeV off-axis is $< 1.7\times$ on-axis
Field Of View	> 2 steradians
Source Location Determination	≤ 1 arcmin (for 1×10^{-7} ph cm^{-2} s^{-1})
Point Source Sensitivity (> 100 MeV)	$< 6 \times 10^{-9}$ cm^{-2} s^{-1} 1 yr survey, 5 σ detection
Time accuracy	Better than 10 μs relative to SV time
Dead Time	< 100 μs per event
Gamma Ray Burst Monitor	
Energy range	5 keV – 25 MeV
Detection Threshold	0.35 ph cm^{-2} s^{-1}
Energy Resolution	$< 10\%$ (1 σ 0.1 – 1 MeV)
Field of View	all sky not occulted by Earth

therefore be determined in two dimensions. The third dimension of the track is determined by analyzing signals from adjacent planes, as the particle travels down through the telescope towards the calorimeter. Each plane of silicon is made up of individual single-sided silicon microstrip detectors. In between each plane of silicon there will be a tungsten foil that will allow a place for the incoming photon to interact and pair-produce charged particles that will be tracked through the tracker. Figure 3.9 shows a cartoon of a pair-production telescope to detail how this technology works.

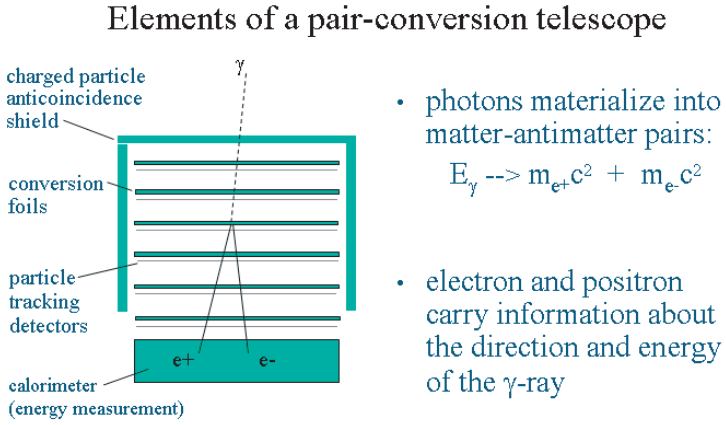

Figure 3.9 Cartoon outlining the operation of a pair production telescope. The high energy photon enters the instrument. In passing though one or more layers of conversion foils (tungsten sheets) the photon interacts with a tungsten nucleus and converts into an electron positron pair. These charged particles then leave a trail of ionization through the silicon tracker. The trails are analyzed to reconstruct the direction of the incoming photon. The particles' energy are deposited and measured in the CsI calorimeter.

To test this design, a beamtest engineering model was constructed and tested. Details of this test are in Appendix B.1

Calorimeter

The GLAST LAT calorimeter will consist of CsI(Tl) bars, arranged in a segmented manner, to give both longitudinal and transverse information about the energy deposition pattern. Once a gamma ray penetrates through the anti-coincidence-shield, converts in the silicon-strip tracker and tungsten converter planes, the product e^+ e^- pass through the rest of the tracker and into the cesium-iodide calorimeters. This causes a scintillation reaction in the cesium-iodide, and the resultant light flash is photoelectrically converted to a voltage using diodes. This voltage is then digitized, recorded and relayed to earth by the spacecraft's onboard computer and telemetry antenna. Cesium-iodide blocks are arranged in two perpendicular directions, to provide additional tracking capabilities within the calorimeter itself.

Anti-coincidence Detector (ACD)

The ACD will consist of segmented plastic scintillator tiles, read out by wave-shifting fibers and photo-multiplier tubes. The segmentation is designed to avoid the self-veto problem of EGRET at high energies while still providing high cosmic-ray rejection. The self-veto problem occurs when high-energy photons create a backsplash of charged particles from the calorimeter and these charged particles hit the ACD causing the high-energy event to be vetoed. The ACD is the first line of background rejection and should reject $> 99.97\%$ of all incoming charged particle background events.

Data Acquisition System (DAQ)

The GLAST LAT data acquisition system (DAQ) is the brain behind the GLAST LAT. It makes the initial on-board distinction between false signals and real gamma ray signals, and decides which of the signals should be relayed to the ground. The DAQ performs this job by hit pattern recognition and preliminary track fitting using information from the tracker, ACD and calorimeter. This system collects the data from the subsystems, implements the multi-level event trigger, and provides an on-board science analysis platform to search for transients. The DAQ will consist of specialized electronics and 32-bit radiation-hard processors that record and analyze the information generated by the silicon-strip detectors, calorimeter, and the ACD. The DAQ will be shielded from the rigors of space-flight, such as extreme high and low temperatures as well as high energy cosmic rays, which can cause the electronics to malfunction

GLAST Burst Monitor (GBM)

The GLAST burst monitor is not part of the LAT, but a separate instrument that is part of GLAST. The GBM is designed to supplement the LAT observations of GRBs. The Burst Monitor includes twelve sodium iodide (NaI) scintillation detectors and two bismuth germanate (BGO) scintillation detectors. The NaI detectors cover the lower part of the energy range, from 10 keV to about one MeV and provide burst triggers and locations. The BGO detectors cover the energy range of $\sim$ 150 keV to

$\sim$ 30 MeV, providing a good overlap with the NaI at the lower end, and with the LAT at the high end. Together the NaI and BGO detectors have similar characteristics to the combination of the BATSE large area and spectroscopy detectors but cover a wider energy range and have a smaller collection area.

3.3.2 Timeline

The timeline for GLAST: construction of the final flight instrument has begun and the launch date is scheduled for late in 2006. Final systems integration and testing will be done at SLAC.

Chapter 4

Type I X-ray bursts

There must be no barriers to freedom of inquiry. There is no place for dogma in science. The scientist is free, and must be free to ask any question, to doubt any assertion, to seek for any evidence, to correct any errors.
– J. Robert Oppenheimer 1949

4.1 Introduction to Type I X-ray bursts

4.1.1 Type I X-ray Burst Observation

Unless specified otherwise, the term "X-ray burst" refers to type I X-ray bursts. Type I X-ray bursts are very quick, large increases in X-ray flux from a source. Type I X-ray bursts are diverse; however, all X-ray bursts share the following features (Strohmayer & Bildsten 2003):

1. Burst rise times are shorter than their decay times. Rise times are typically < 2 s, but can be as long as 10 s. Typical decay times are 10–20 s, but can be as long as several hundreds of seconds.

2. Burst profiles are shorter at higher energies.

3. Burst profiles are generally smooth, showing an exponential-like decay.

4. Burst spectra are described well by a blackbody, always showing cooling during the decay (e.g Swank et al. 1977).

Of the approximately 160 known LMXBs, bursts have been detected from about 70 (Strohmayer & Bildsten 2003). X-ray bursts are most commonly observed from the lower luminosity "atoll" LMXBs, however bursts have also been observed in bright Z sources as well. X-ray bursts have also been detected from sources with such low persistent luminosities that the quiescent flux is less than 10^{-10} ergs cm^{-2} s^{-1} (Cornelisse et al. 2002). Therefore, bursting is observed for accretion rates of $10^{-10} \lesssim \dot{M} \lesssim 2 \times 10^{-8}$ M$_\odot$ yr^{-1}.

Unstable thermonuclear burning on the surface of a weakly magnetized neutron star is the generally accepted model for type I X-ray bursts. Material accretes onto the surface until it reaches densities and temperatures sufficient for nuclear ignition. For some accretion rates, the burning is unstable and propagates around the star consuming all of the available fuel, resulting in an X-ray burst. This type of X-ray burst is characterized by a fast rise time of a few seconds and a decay time longer than a few seconds (up to several minutes). See Strohmayer & Bildsten (2003), Hansen & van Horn (1975), Lewin, van Paradijs, & van den Heuvel (1995), Paczynski (1983), Bildsten (2000), and §4.1.2 for a more detailed description.

Recently, high frequency (300–600 Hz) oscillations have been discovered during X-ray bursts, termed "burst oscillations" (Strohmayer & Markwardt 1999). It is commonly believed that the compact object spin modulation of the X-ray burst flux is the basic mechanism responsible for oscillations. These oscillations can have a large amplitude and occur shortly after the initial rise of the X-ray flux. The amplitude of these modulations have been shown to be anti-correlated with the X-ray burst flux. The thermonuclear model supports this finding, the burst starts as a local burning hot spot that quickly expands ($\sim$1 s) to engulf the entire surface of the compact object (Nath, Strohmayer, & Swank 2002). Most of these oscillations are observed to spin up to an asymptotic value during the decay of the burst flux, with this asymptotic value being viewed as the spin frequency of the star. For more detailed information on burst oscillations see Strohmayer & Bildsten (2003).

The type I X-ray bursts discussed in this paper are different from the X-ray superbursts recently discovered e.g (Kuulkers et al. 2002). Type I X-ray bursts occur when a mixture of hydrogen and helium on the surface of a neutron star ignites via thermonuclear processes forming carbon, oxygen and other elements (more details in §4.1.2). These bursts last $\sim$ a few seconds – 100s of seconds. Superbursts likely occur due to nuclear burning of carbon or by some other nuclear processes and last for several hours (see Cumming & Bildsten 2001 and Strohmayer & Brown 2002 for a review).

4.1.2 Type I X-ray Burst Theory

At the core of the X-ray burst engine is a thin shell instability which results when the nuclear energy generation rate is more temperature sensitive than radiative cooling and is confined to a thin shell. The shell model is used successfully to calculate how these instabilities occur in Paczynski (1983) and elaborated upon in Narayan & Heyl (2002).

Hydrogen and helium (of varying abundances and may or may not include other elements), are accreted onto the surface of a neutron star. After accretion the material gets compressed as new material is piled on top of it. The hydrostatic pressure causes the material to reach ignition densities and temperatures within a few hours to days, depending on the chemical composition and the accretion rate per unit area, $\dot{m} = \dot{M}/A_{acc}$, where $\dot{M}$ is the mass accretion rate and A_{acc} is the area covered by fresh material. Unless strong magnetic fields are present, as with a pulsar, one can take $A_{acc} \lesssim 4\pi R^2 \approx 1.2 \times 10^{13}$ cm^2. Here we assume the accreted material covers the entire surface of the neutron star with $R = 10$ km. This material may cover a small fraction of the neutron star surface if magnetic fields affect the flow over the surface of the star.

The temperature in the accreted material exceeds 10^7 K and the hydrogen burns via the CNO cycle, or if the temperature exceeds $\sim 8 \times 10^7$ K via the hot CNO cycle, see Figure 4.1. The stability of this process depends on the accretion rate and composition of the accreted material. There exist four possibilities (Paczynski 1983;

Narayan & Heyl 2002):

1. For $\dot{m} \lesssim 900$ g cm^{-2} s$^{-1}(Z_{CNO}/0.01)^{1/2}$, the hydrogen burning is unstable and can lead to X-ray bursts triggered by unstable hydrogen ignition. Z_{CNO} is the mass fraction of CNO.

2. For 900 g cm^{-2} s$^{-1}(Z_{CNO}/0.01)^{1/2} \lesssim \dot{m} \lesssim 2000$ g cm^{-2} s$^{-1}(Z_{CNO}/0.01)^{13/18}$ the hydrogen burns and is thermally stable. Pure helium ignition occurs leading to an X-ray burst.

3. For 2000 g cm^{-2} s$^{-1}(Z_{CNO}/0.01)^{13/18} \lesssim \dot{m} \lesssim 10^5$ g cm^{-2} s^{-1}, there is mixed hydrogen and helium burning and a burst is triggered by unstable helium ignition.

4. For $\dot{m} \approx 10^5$ g cm^{-2} s^{-1}, near the Eddington limit, stable hydrogen and helium burning begins and no X-ray bursts result.

The transition numbers above are from Strohmayer & Bildsten (2003) and should only be used as a rough guide. Narayan & Heyl (2002) and Paczynski (1983) show that there are other factors that need to be considered when calculating such boundaries, such as temperature of the surface, and surface mass density. In fact, as Narayan & Heyl (2002) point out, at very low luminosities, the hydrogen burning is unstable (see list above), but the recurrence time for these bursts would be too long for interest in transient X-ray binaries.

When the instability in the burning layer occurs the flash burns at a fixed pressure and the increasing temperature allows radiation pressure to dominate. For pure helium flashes, item 2 above, the fuel burns rapidly via the triple-alpha process[1] and the local Eddington limit is often exceeded leading to a photospheric radius expansion (PRE) burst, lasting 5–10 s. When hydrogen and helium are present, then the burning can reach very high temperatures and trigger the rapid-proton (rp) process (Figure 4.1). This rp process is a succession of proton capture and β decays, which can produce heavy elements far beyond the iron group, see Strohmayer &

[1] $^4\mathrm{He} + {}^4\mathrm{He} \rightarrow {}^8\mathrm{Be} + {}^4\mathrm{He} \rightarrow {}^{12}\mathrm{C} + \gamma$, sometimes followed by ${}^{4n}\mathrm{X} + {}^4\mathrm{He} \rightarrow {}^{4(n+1)}\mathrm{X}' + \gamma$

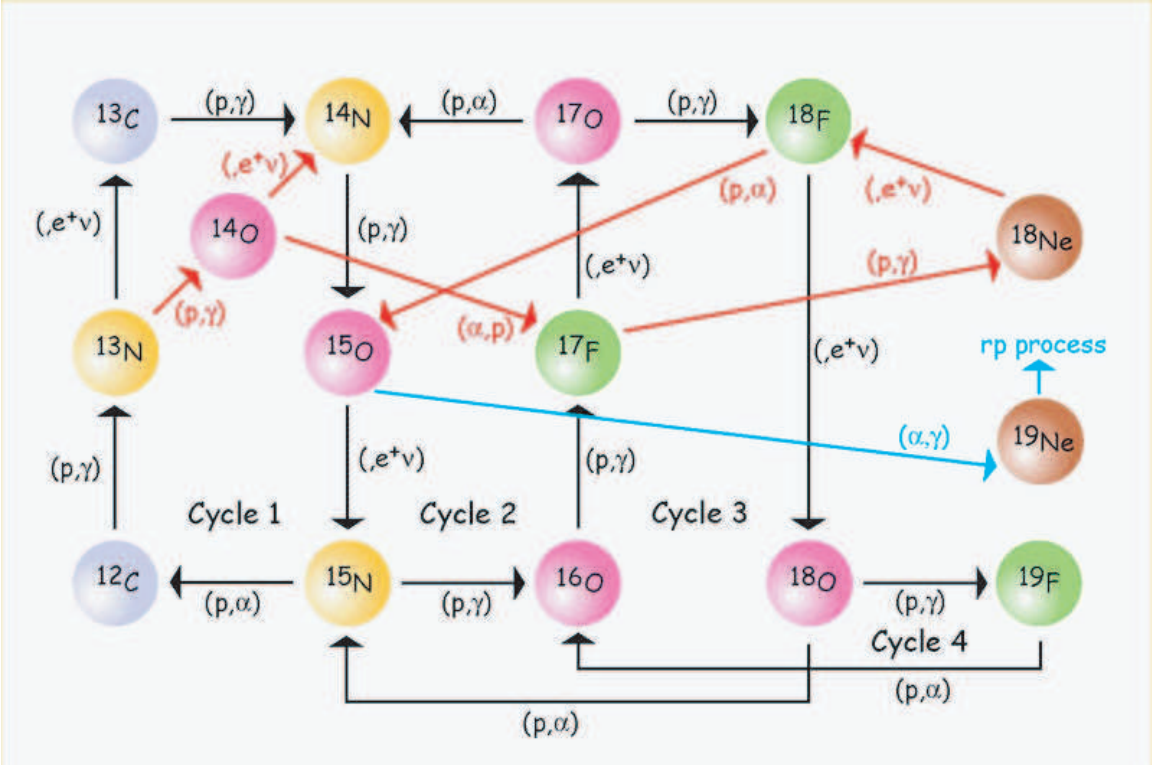

CNO: T < 8 x 10^7 K HOT CNO: T > 8 x 10^7 K RP: T > 5 x 10^8 K

Figure 4.1 Diagram showing the CNO process that normally takes place as fuel is burning on the surface of a neutron star. The process converts hydrogen to helium by following the black path along cycle 1 (most dominant cycle). If temperatures are high enough the hot CNO cycle dominates where ^{14}O is formed and usually produces ^{14}N and continues along cycle 1. If the temperatures get still higher, then ^{19}Ne can be produced and this is a seed for the rp process which creates heavy elements by means of successive proton captures and β decays. Drawing courtesy of F. X. Timmes of the University of Chicago and the School of Art Institute of Chicago.

Bildsten (2003) and references therein. A mixed hydrogen helium burst can last up to several hundred seconds.

4.1.3 X-ray Bursts as Evidence for Surfaces

In the nuclear burning model for X-ray bursts, a well-defined surface must exist for an X-ray burst to occur. Narayan & Heyl (2002) (hereafter NH02) performed a stability analysis of accumulating fuel on the surface of a generic compact object and showed that if Black Hole Candidates (BHCs) had surfaces, they would be expected to exhibit X-ray bursts. For this reason the lack of type I X-ray bursts in BHCs in stellar systems can be considered as evidence for an event horizon.

BHCs are typically distinguished from neutron stars using one of three methods. The primary method is direct dynamical measurements of their companions yielding masses for the compact objects that are $\gtrsim 3$ $M_{\odot}$, where a stable equation of state for a neutron star does not exist. The second method is that if timing and spectral analysis of the radiation from the accretion onto the compact object resembles other known BHCs the compact object is usually classified as a BHC. This typically means very little power above ∼500 Hz in a Fourier power density spectrum (Sunyaev & Revnivtsev 2000) and an energy spectrum that cannot be explained by a low temperature blackbody with an emission radius of ∼10 km (Rutledge et al. 2000). It has recently been discovered that BHCs may exhibit unique differences from neutron stars when viewed on a color-color diagram (Done & Gierliński 2003). Thirdly, if an object exhibits type I burst behavior it is assumed to be a neutron star as this is strong evidence for the presence of a surface. This is the case for the compact object in GS 1826−238, which was first classified as a BHC based on timing and spectral behavior. It was only reclassified as a neutron star when X-ray bursts were detected (Ubertini et al. 1999). This is also the case for the compact object in Circinus X-1, which has timing and spectral behavior at times resembling a BHC and at other times resembling a Z source neutron star. However, two type I X-ray bursts were detected from Circinus X-1 in 1986 (Tennant, Fabian, & Shafer 1986) resulting in its classification as a neutron star.

In this section we present observations of neutron star LMXBs and BHCs from the USA and RXTE telescopes as observational support for the work of NH02. We survey both neutron star and BHC systems for X-ray bursts and calculate burst rates for neutron stars and upper limits for the burst rate in BHCs, both overall and in the unstable burning regions calculated by NH02. This provides quantitative results which are important in any attempt to demonstrate formally the existence of event horizons using the method of NH02. In addition, it is important that any evidence in support or contradiction of the black hole model be aired to watch for evidence the standard picture may not be quite right (Peebles 2002; Babak & Grishchuk 2002).

4.2 Observations and Data Analysis

4.2.1 Data Analysis

All binary sources with more than 30 ks of exposure time with the USA detector were scanned for bursts, including seven BHCs and seventeen neutron stars. The selection criteria described in §4.3.2 result in less than 30 ks of analyzed data on some sources. The list of selected data analyzed in this paper is shown in Table 4.1. The columns are the source name, total time of good data analyzed, distance and mass of the source, classification of the source (BHC) Black Hole Candidate, Neutron Star (NS) and if a subdivision of Z or atoll is clear. Additional information on the sources can be found in the references given. To supplement the USA BHC data, the RXTE public BHC data were analyzed for each USA BHC source analyzed in this paper, all public data for these sources as of April 2003, were analyzed.

Table 4.1. USA observing times of X-ray binaries searched for bursts

Source	**Time (ks)**	**Dist. (kpc)**	**Mass estimate** ($M_\odot$)	**Class**[c]	**Reference(s)**
Cygnus X-1	449 - USA 1748 - RXTE	2	~ 10.1	BHC	Herrero et al. 1995
XTE J1118+480	183 - USA 119 - RXTE	1.9 ± 0.4	6.0 ± 0.36	BHC	Wagner et al. 2001 McClintock et al. 2001
GRS 1915+105	163 - USA 2358 - RXTE	12.5	14 ± 4	BHC	Greiner et al. 2001
XTE J1859+226	94 - USA 311 - RXTE	11	$\geq 7.4 \pm 1.1$	BHC	Filippenko & Chornock 2001 Zurita et al. 2002
XTE J1550−564	50 - USA 606 - RXTE	$3 - 6$	$9.7 - 11.6$	BHC	Orosz et al. 2002
4U 1630−472	46.2 - USA	10	??[a]	BHC	Augusteijn et al. 2001 Meyer-Hofmeister & Meyer 2001
Cygnus X-3	37.0 - USA 335 - RXTE	11.6	17^{+23}_{-10}[d]	BHC	Singh et al. 2002 Schmutz et al. 1996
Cygnus X-2	158.1	7.2 ± 0.11	1.4 ± 0.6	NS, b	Titarchuk & Shaposhnikov 2002 Orosz & Kuulkers 1999
Aquila X-1	93.2	$4 - 6.5$	~ 1.4[b]	NS A, b	Rutledge et al. 2001
EXO 0748−676	124.8	7.6	~ 1.4[b]	NS, b	van Paradijs & White 1995 Shahbaz & Kuulkers 1998
Rapid Burster	89.2	8.6	~ 1.4[b]	NS, b	Marshall et al. 2001
GX 354−0	81.1	$4.4 - 6.2$	~ 1.4[b]	NS A, b	Galloway et al. 2003
Circinus X-1	75.6	6.7 ± 1.2	$1.4 - 3.0$[e]	NS, b	Mignani et al. 2002 Saz Parkinson 2003
4U 0614+09	66.2	5	~ 1.4[b]	NS, b	Brandt et al. 1992 Christian & Swank 1997
GX 349+2 (Scorpius X-2)	81.6	5	~ 1.4[b]	NS Z	O'Neill et al. 2002 Christian & Swank 1997
XB 1254−690	51.7	12	??[f]	NS, b	Iaria et al. 2001 Christian & Swank 1997

Table 4.1—Continued

Scorpius X-1	44.3	2.8 ± 0.3	1.4 ± 0.6	NS, Z	Titarchuk & Shaposhnikov 2002 Geldzahler et al. 1999
4U 1735−445	38.1	9.2	~ 1.4[b]	NS A, b	Seon et al. 1997 van Paradijs & White 1995
X1636−536	37.9	6.5 ± 0.2	~ 1.4[b]	NS, b	van Paradijs & White 1995 Christian & Swank 1997
GX 5−1	34.6	9	~ 1.4[b]	NS, Z	Christian & Swank 1997
GX 3+1	28.7	4-6	~ 1.4[b]	NS A, b	Kuulkers & van der Klis 2000 Christian & Swank 1997
GX 340+0	28.5	9.5-11.0	~ 1.4[b]	NS, Z	Christian & Swank 1997
GX 17+2	29.4	7.5	~ 1.4[b]	NS, Z, b	Christian & Swank 1997
MXB 1659−298	16.0	~ 10	~ 1.4[b]	NS A, b	Wijnands et al. 2002

[a]There is no dynamical mass estimate for 4U 1630−472. This source was not used in burst rate limit calculations.

[b]This neutron star mass is unknown, a value of 1.4 $M_\odot$ was assumed.

[c]Class of the source: BHC - Black Hole Candidate; NS - Neutron Star; A - atoll source; Z - Z source; b - if bursts have been detected in the source in the past.

[d]The mass function for this source is 2.3 $M_\odot$, the nature of the compact object in this source is still unknown. This source was not used in burst rate limit calculations.

[e]Timing and spectral analysis of this source give evidence that Circinus X-1 is larger than 1.4 $M_\odot$ (Saz Parkinson 2003). This source was not used in burst rate calculations

[f]The nature of this source could not be identified independent of bursts, therefore this source was not used in burst rate calculations.

Source Categorization Criteria

Because we are testing for the presence of bursts on objects purported to be black holes the classification criteria used must be crafted to avoid selection effects. Most importantly, the sources must not be classified based on the presence or absence of type I bursts. We have thus categorized our sources into neutron stars or black holes as follows.

Black Hole Candidates Each of the BHCs, with the exception of 4U 1630−472, have a known mass function or other mass estimate that give a lower mass limit of the compact object that exceed current theoretical limits for neutron stars. In the quiescent state of an X-ray binary, the absorption line velocities of the secondary star can be measured precisely because the non-stellar light from the accretion flow is low compared to the secondary luminosity. Measuring the velocity of the secondary as a

function of binary orbit phase, one may determine the mass function,

$$f(M) \equiv \frac{M_1^3 \sin^3 i}{(M_1 + M_2)^2} \tag{4.1}$$

where M_1 and M_2 are the masses of the compact object and secondary star, and i is the orbital inclination angle. The mass function provides a strict lower limit on the mass of the compact object.

Since 4U 1630−472 does not have a mass limit requiring it to be a BHC, the data from this source are not used in calculating any of the bursting rates or bursting rate limits used later in this chapter. Cygnus X-3 also has a debateable compact object. Cygnus X-3 has a mass function of 2.3 $M_\odot$ (Schmutz, Geballe, & Schild 1996) which does not rule out the possibility that the compact object is a neutron star. Therefore, the data of Cygnus X-3 are not used in calculating any burst rates or limits quoted in this paper. These two sources are included in Table 4.1 for completeness, to let the curious reader know that we did search the data of these sources and no X-ray bursts were detected.

Neutron Stars The following neutron stars were classified as such based on the presence of kilohertz quasi-periodic oscillations (QPOs): Cygnus X-2, Aquila X-1, EXO 0748−676, GX 354 − 0 (4U 1728−34), 4U 0614+09, GX 349+2, Scorpius X-1, 4U 1735−445, X1636−536, GX 5-1, GX 340+0, and GX 17+2. The generally accepted view is that these kHz QPOs represent in some way an orbital frequency around the compact object. The frequency of an orbit around a compact object is:

$$\nu_{orb} = \left(\frac{GM}{4\pi^2 r_{orb}^3}\right)^{1/2} \approx 1200 \text{ Hz } \left(\frac{r_{orb}}{15 \text{ km}}\right)^{-3/2} M_{1.4}^{1/2}, \tag{4.2}$$

where $M_{1.4}$ is the mass of the compact object in units of 1.4 $M_\odot$. From general relativity, no stable orbital motion is possible within the innermost stable circular orbit (ISCO). $R_{ISCO} = 6GM/c^2 \approx 12.5\ M_{1.4}$ km, for a non-rotating compact object. At this orbit, the frequency is $\nu_{ISCO} \approx (1600/M_{1.4})$ Hz (van der Klis 2000). From this, one can see that an object too massive to exist as a neutron star, $M \gtrsim 3$ $M_\odot$, should

not demonstrate QPOs in the kHz range[2]. For a list of known sources demonstrating kilohertz QPOs and a review of millisecond oscillations in X-ray binaries see van der Klis (2000).

The Rapid Burster is an unusual source which frequently demonstrates X-ray bursts that repeat rapidly with a period of a few to tens of seconds. These X-ray bursts are found in this source in addition to the type I X-ray bursts present. Currently, these bursts have only been detected in the Rapid Burster and the Bursting Pulsar (GRO 1744–28). These bursts do not show cooling during the tail of the burst and are believed to be caused by an accretion phenomena not thermonuclear burning. These type of X-ray bursts are called type II X-ray bursts. The Rapid Burster is classified as a neutron star based on the presence of excess power in the kHz range during it's type II X-ray bursts as reported in Guerriero et al. (1997). The presence of significant noise above 500 Hz in an X-ray power spectrum density distribution (PSD) gives evidence for a neutron star according to Sunyaev & Revnivtsev (2000). In addition, spectral work from Chandra data give evidence of a radius $\sim$ 10 km for this source by looking at the type II X-ray bursts (Marshall et al. 2001), giving further evidence that this source should be classified as a neutron star.

The sources XB 1254−690 and Circinus X-1 do not have strong enough evidence to support that they are neutron stars independent of the past observed type I X-ray bursts. Therefore, these sources will be included in Table 4.1 for completeness, but will not be included in any bursting rate or bursting rate limit calculations.

Detecting Bursts

The data were searched for bursts by visually inspecting the light curves, binned in one second intervals for USA data and 1/8 second intervals for RXTE data, of each observation several times. The visual scan looked for events that displayed properties consistent with type I X-ray bursts: large changes in flux with Fast Rise Exponential Decay (FRED) profiles, rise times of a few seconds, and decay times of several seconds or more. Any feature that increased its flux by a factor of two on timescales of a few seconds and showed a FRED profile was flagged as a possible

[2]Some QPO models allow for $\nu_{QPO} > \nu_{ISCO}$.

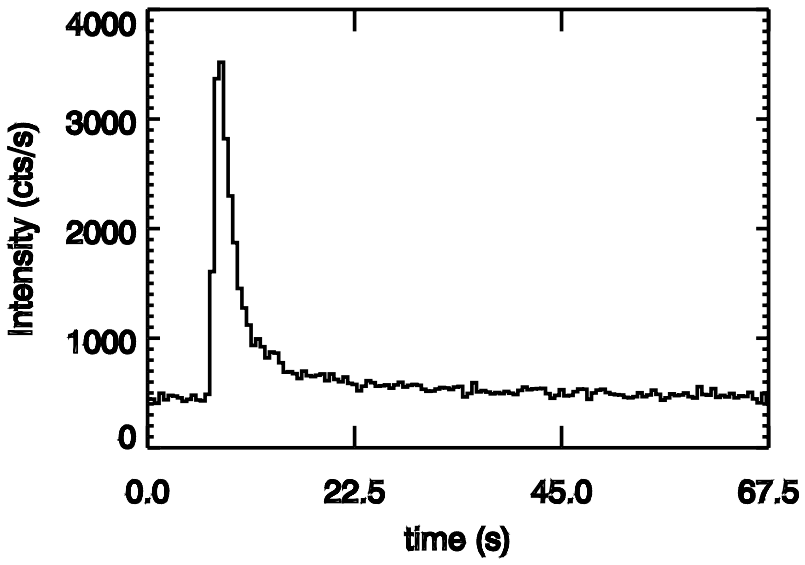

Figure 4.2 Example of a typical type I X-ray burst observed in 4U $1735-445$ by USA.

type I X-ray burst. After flagging the burst, energy spectral analysis was performed to ensure the burst showed blackbody cooling seen in all type I X-ray bursts. At the flux levels of all of the sources included in this work, this method will easily detect all X-ray bursts. Even if a burst in a BHC occurred with as much as a factor of four less luminosity compared to a neutron star, as would be expected due to general relativistic effects see Abramowicz, Kluźniak, & Lasota (2002), we expect to have detected them visually. Figure 4.2 shows an example of a typical type I X-ray burst found by USA in 4U $1735-445$. We did not search the USA data archive for superbursts. The longest continuous observation by USA was 20 minutes, with no less than 90 minutes between observations of the same source, making a burst spanning several hours difficult to detect.

4.2.2 Observations of Neutron Star Systems

Of the seventeen neutron stars that we studied (see Table 4.1), seven were observed to have type I X-ray bursts. These are: Aquila X-1, EXO 0748−676, GX 354−0, the Rapid Burster, 4U 1735−445 , GX 3+1, and MXB 1659−298. The Rapid Burster

and GX 354−0 are separated in the sky by only 0.54°. Thus, they will be in the USA FOV at the same time making it possible to mistake a burst in one source for a burst in the other source, albeit attenuated by a factor of 0.53. For this reason, the data for these two sources were double counted in our analysis, meaning that an observation pointed at either source was considered to be a simultaneous observation of both sources. Therefore, the total observing time of these two sources will be twice the sum of the respective pointed observations. In theory, one may distinguish the Rapid Burster type I X-ray bursts from the GX 354−0 X-ray bursts. The GX 354−0 bursts nearly always show radius expansion and are much brighter than the Rapid Burster type I X-ray bursts (Kuulkers 2003; Fox 2003). In addition, the GX 354−0 bursts may display a harder spectrum than the Rapid Burster bursts (Fox et al. 2001; Fox 2003). However, we were not able to see definite evidence for radius expansion in the energy spectra of any of these bursts, and we were not able to distinguish two groups of bursts by any energy or timing analysis of the bursts from these sources (See §4.5.1). This may be due to the energy resolution of the USA experiment. The intensity difference cannot be used to distinguish these sources since a collimator effect would disguise the burst intensity. Therefore, since the Rapid Burster and GX 354−0 are both known to display type I X-ray bursts regularly (Lewin, van Paradijs, & Taam 1995; Fox et al. 2001), we cannot distinguish the bursts from these two sources.

Several type I X-ray bursts were observed in the vicinity of the Rapid Burster in addition to hundreds of type II bursts that occur continuously in this source when it is in a bursting state. We distinguished the type II bursts in this source from the type I bursts by their regular, 'rapid-fire', intervals. Spectral differences can be used to give a more definite distinction between the types of X-ray bursts. Type I X-ray bursts always have cooling blackbody spectra. Type II X-ray bursts do not show softening throughout the burst characteristic of a cooling blackbody. See Figures 4.3 and 4.2 for an example of type II and type I bursts detected by USA. See Guerriero et al. (1999); Lewin, van Paradijs, & Taam (1993) for more information on the Rapid Burster and type II X-ray bursts. Table 4.2 gives a list of bursts found in each source in our survey.

We did not detect bursts in ten of the seventeen neutron stars in our data:

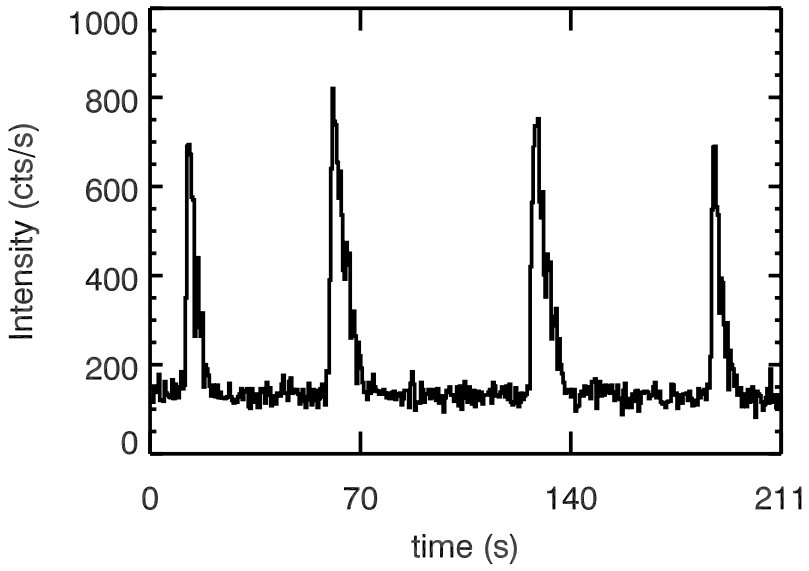

Figure 4.3 Example of type II X-ray burst behavior in the Rapid Burster seen by USA. We distinguished the type II bursts based on their very regular pattern not seen in the type I bursts.

Cygnus X-2, Circinus X-1, 4U 0614+09, GX 349+2, XB 1254−690, Scorpius X-1, X1636−536, GX 5−1, GX 340+0, GX 17+2. Type I X-ray bursts have been detected in the past for each of these neutron star systems observed except for GX 349+2, Scorpius X-1, GX 5−1, and GX 340+0. Using the data from all seventeen neutron stars, we calculate an overall neutron star bursting rate $\lambda_{\rm NS} = 1.7 \pm 0.4 \times 10^{-5}$ bursts s^{-1} per neutron star. This results in an observed average time between bursts in our data, $R_{\rm NS} = 59.1$ ks, about 16.5 hours, from 1122 ks of data (double counting the GX 354−0 and Rapid Burster data).

4.2.3 Observations of Black Hole Candidates

Seven BHCs were searched for bursts: Cygnus X-1, XTE J1118+480, GRS 1915+105, XTE J1859+226, XTE J1550−564, 4U 1630−472, and Cygnus X-3. The total USA observing time for all of these BHCs is 1022 ks, the total observing time for the RXTE PCA/HEXTE is 5477 ks. No evidence of bursts was detected. Data from 4U 1630−472 and Cygnus X-3 were not used in any burst limit calculations. GRS 1915+105

Table 4.2 Detected type I X-ray bursts of the USA experiment

Source	**Time of Burst Peak [MJD]**	**Rate Change [cts s^{-1}]**
Aquila X-1	51856.15684	1000 $\longrightarrow$ 5000
EXO 0748−676	51614.54328	30 $\longrightarrow$ 420
	51648.97544	40 $\longrightarrow$ 420
	51648.41676	35 $\longrightarrow$ 400
	51669.44317	40 $\longrightarrow$ 470
	51687.50888	50 $\longrightarrow$ 520
Rapid Burster / GX 354−0[a]	51482.51368	300 $\longrightarrow$ 2700
	51487.23736	200 $\longrightarrow$ 2100
	51492.94726	150 $\longrightarrow$ 2100
	51861.23391	220 $\longrightarrow$ 1100
	51861.93667	120 $\longrightarrow$ 1500
	51491.82323	300 $\longrightarrow$ 2000
	51743.31991	250 $\longrightarrow$ 2600
	51812.96651	250 $\longrightarrow$ 3000
	51816.00111	300 $\longrightarrow$ 4000
	51817.41458	250 $\longrightarrow$ 4400
4U 1735−445	51379.11730	400 $\longrightarrow$ 3400
GX 3+1	51396.12709	200 $\longrightarrow$ 1000
MXB 1659−298	51850.08140	180 $\longrightarrow$ 400

[a] The Rapid Burster and GX 354−0 are both in the USA FOV at the same time, therefore a burst in one source would be indistinguishable from a burst in the other.

showed several flares during the USA observations, but close examination showed no distinct FRED profiles in these flares that would signal a type I X-ray burst. The USA observations were scheduled for repeated sampling to obtain many short observations over a long time period. The RXTE Target of Opportunity (TOO) observations repeatedly sampled transient sources during outbursts. As applied to transients this is particularly effective for the sources studied here: bursting may not occur in all ranges of mass accretion rate but the USA and RXTE observations sampled this critical parameter over the maximum extent possible. If BHCs burst in a narrow

range of mass accretion rate, we are likely to have sampled that range. The USA experiment was fortunate that over its lifetime it was able to observe a number of very important transients, including systems with the largest known physical dimensions (GRS 1915+105) and the smallest (XTE J1118+480). USA and RXTE also devoted substantial time to Cygnus X-1 and GRS 1915+105, so that there was ample opportunity for any rare modes of bursting to be present in our observation of these sources.

X-ray bursts are not a Poisson process. The time between bursts is a function of how long it takes to accumulate fuel to reach a critical density and temperature where unstable nuclear burning can occur. Burst intervals have been observed to be regular and irregular, and range from $\sim$ 5 min to days or longer (Lewin, van Paradijs, & Taam 1995), and are dependent on the accretion composition and rate (Strohmayer & Brown 2002). However, since our observation times were short compared to typical burst intervals and the revisit times were hours or longer, we are unlikely to observe consecutive bursts. Therefore, we treat these observations using Poisson statistics in order to place a numerical limit on the bursting rate. The probability of observing n events of a Poisson process is:

$$P(n) = (\lambda T)^n \frac{e^{-\lambda T}}{n!}, \tag{4.3}$$

where: λ is the rate of bursts (bursts s^{-1}) and T is the total observing time. We will also define $R = 1/\lambda$ the average time between bursts. To set a limit on the burst rate to a confidence level of $CL = 95\%$ we calculate from eq. 4.3 for $n = 0$:

$$\lambda = -\frac{\ln(1 - CL)}{T} \tag{4.4}$$

where $P = 1 - CL$. For the values given, we calculate the upper limit of $\lambda_{\rm BHC} = 4.9 \times 10^{-7}$ bursts s^{-1} with a 95% confidence level. This is the first published survey to place quantitative limits on the rate of occurrence of bursts in a wide range of BHCs with a significant amount of data. As discussed in Knight (2003), limits of these type emphasizing searches and null results are important to promulgate to the rest of the

scientific community.

4.3 Discussion

In this section we discuss these observations in the context of the theoretical work of NH02. We start by converting our results to a format which allows easy comparison with theoretical predictions. Next, we show that our data in conjunction with the stability analysis of NH02, can place a probablity-limit on the existence of a surface on a BHC. Finally, we check our neutron star results for consistency with the NH02 analysis.

4.3.1 Theoretical Framework of Narayan & Heyl

Consider a compact spherical star of mass M and radius R, accreting steadily at a rate $\dot{\Sigma}$ (g cm^{-2} s^{-1}). In the local frame, the gravitational acceleration is $g = GM(1+z)/R^2$, where the redshift, z, is given by $1 + z = (1 - R_S/R)^{-1/2}$, and $R_S = 2GM/c^2$ is the Schwarzschild radius. Assume the accreting material has a solar composition ($\sim$ 70% H, 27% He, and 3% CNO) and is sitting in a thin shell on the surface above a substrate of fully burnt material. Assuming plane parallel geometry and g independent of depth, solve for density, ρ, temperature, T, outgoing flux, F, and the hydrogen, helium and heavy element fractions, $X, Y, Z = 1 - X - Y$, as functions of column density, Σ.

Hydrostatic equilibrium, combined with the equation of state $P = P(\rho, T)$ of the gas gives:

$$\frac{\partial P}{\partial \Sigma} = \frac{\partial P}{\partial \rho}\frac{\partial \rho}{\partial \Sigma} + \frac{\partial P}{\partial T}\frac{\partial T}{\partial \Sigma} = -g \tag{4.5}$$

For the equation of state of the material we follow the procedure outlined in Paczynski (1983) using a "One-Zone Model for Shell Flashes" where the authors contend that one can treat the equations controlling the physics of the flashes as if they were contained in a thin shell around the stellar surface and independent of the core of the star. The model describes the whole hydrogen-rich layer with one mass zone overlying a core of a fixed size. Using the plane parallel geometry mentioned above, the stellar

structure equations are:

$$\begin{aligned} \frac{\partial P}{\partial \Sigma} &= -g; & \frac{\partial P_r}{\partial \Sigma} &= -\frac{\kappa F}{c}; \\ \frac{\partial F}{\partial \Sigma} &= \epsilon - T\frac{dS}{dt}; & \frac{\partial z}{\partial \Sigma} &= \frac{1}{\rho}; \\ \frac{dX}{dt} &= -\frac{\epsilon_H}{E^*_H}; & \frac{dY}{dt} &= -\frac{dX}{dt} - \frac{\epsilon_{He}}{E^*_{He}}; \\ \frac{d}{dt} &\equiv \dot{\Sigma}\frac{\partial}{\partial \Sigma}, \end{aligned} \tag{4.6}$$

where P_r is the radiation pressure, S is the entropy, ϵ is the nuclear energy generation rate, κ is the opacity, c is the speed of light, and E^* is the energy released by burning one g of fuel. For ϵ_H NH02 include the pp chain *and* the CNO cycle, whereas Paczynski (1983) only includes the pp chain for simplification. All CNO reactions are considered: fast, saturated and electron capture. However, proton capture onto heavier nuclei is not included based on the assumption that the details of the deep crust are unimportant for predicting the overall bursting behavior of the thin shell. For the He-burning, triple-α reactions are included by NH02, Paczynski (1983) does not consider helium burning.

Radiative transfer gives another differential equation:

$$\frac{\partial T}{\partial \Sigma} = \frac{3\kappa F}{16\sigma T^3}, \ \frac{1}{\kappa} = \frac{1}{\kappa_{\rm rad}} + \frac{1}{\kappa_{\rm cond}}. \tag{4.7}$$

NH02 employed the fitting functions in Iben (1975) for the radiative opacity, $\kappa_{\rm rad}$, and an analytical formula from Clayton (1968) for the conductive opacity, $\kappa_{\rm cond}$, after correcting for relativistic electrons.

The energy equation gives,

$$\rho T\frac{ds}{dt} = \rho(\epsilon_H + \epsilon_{He}) + \rho\frac{\partial F}{\partial \Sigma}, \tag{4.8}$$

where s is the specific entropy.

To solve the above differential equations, the following boundary conditions are used, at the surface $\Sigma = 0$, $X = X_0$, $Y = Y_0$, at the base $\Sigma = \Sigma_{\rm max}$. The final

boundary condition comes from equating the accretion luminosity of the infalling matter to blackbody emission from the surface:

$$L_{\rm acc} = 4\pi R^2 \dot{\Sigma} c^2 z/(1+z) = 4\pi R^2 \sigma T_{\rm out}^4 \tag{4.9}$$

The nuclear energy generation rate from steady processes is ignored. This fixes the surface temperature $T_{\rm out}$. So, after assuming a $T_{\rm out}$ and $F_{\rm out}$ NH02 solved for the surface density profile $\rho(\Sigma)$ from the radiative transfer equation above, recall for hydrostatic balance $\partial\rho/\partial\Sigma = -g$. NH02 assumed that the temperature at the top of the substrate, $T_{\rm in} = T(\Sigma_{\rm max})$, is fixed. NH02 examined several values for $T_{\rm in}$, corresponding to $T_{\rm in} \lesssim 10^8$ K for a reasonable value of a LMXB neutron star, and $T_{\rm in} \lesssim 10^{7.5}$ K for the BHC models. The value for $T_{\rm in}$ in the BHC was motivated by the low quiescent luminosity of many of the BHC LMXRBs.

NH02 then solve for steady state profile in the accretion layer, $d/dt \rightarrow \dot{\Sigma} d/d\Sigma, \partial/\partial\Sigma \rightarrow d/d\Sigma$, which comes from setting $\partial/\partial t = 0$. The solution to the differential equations listed above gives the profiles of the fluid quantities: $\rho(\Sigma), T(\Sigma), F(\Sigma), X(\Sigma), Y(\Sigma)$.

After finding a steady state solution, the next step is to check its stability. To do this, NH02 start with the steady state solution and assume that it is slightly perturbed,

$$Q(\Sigma) \rightarrow Q(\Sigma) + Q'(\Sigma) {\rm e}^{(\gamma t)}, \tag{4.10}$$

where Q corresponds to each of the five variables above and the perturbations $Q'(\Sigma)$ are small. NH02 linearize the five equations, apply boundary conditions, and solve for the eigenvalue γ. The accretion layer is considered unstable if any eigenvalue has a real part (growth rate) larger than the characteristic accretion rate $\gamma_{\rm acc} = \dot{\Sigma}/\Sigma_{\rm max}$. If the steady-state model is unstable according to this analysis, accretion cannot proceed stably with the particular $\Sigma_{\rm max}$ and $\dot{\Sigma}$. The assumption is then made that once ignited at some random point, this instability envelopes the surface of the star resulting in a type I X-ray burst. For information about this assumption see Spitkovsky, Levin, & Ushomirsky (2002) for more details of the onset of the burst and flame propagation.

Figure 4.4 shows the results for solar composition material ($X_0 = 0.7, Y_0 = 0.27, Z_0 = 0.03$) accreting onto either a 1.4 $M_\odot$ neutron star (top panels), or a 10 $M_\odot$

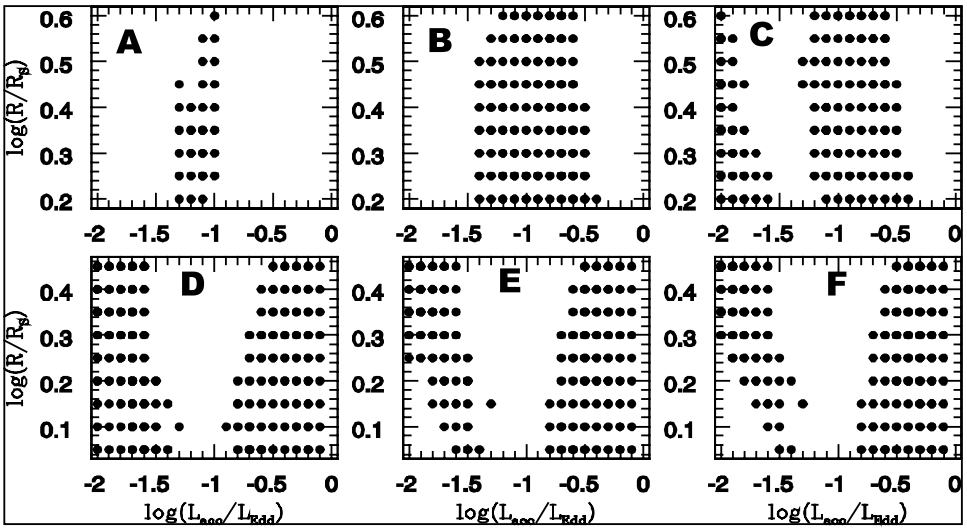

Figure 4.4 Figure 1 in NH02, regions of instability, shown by dots, as a function of accretion luminosity and stellar radius. **A** – 1.4 $M_\odot$ NS with a base temperature $T_{\rm in} = 10^{8.5}$ K. **B** – NS $T_{\rm in} = 10^{8}$ K. **C** – NS $T_{\rm in} = 10^{7.5}$ K. **D** – 10 $M_\odot$ BHC with a surface, and a base temperature $T_{\rm in} = 10^{7.5}$ K. **E** – BHC $T_{\rm in} = 10^{7}$ K. **F** – BHC $T_{\rm in} = 10^{6.5}$ K. This figure shows the regions of instability for different values of the radius of the surface, shown on the Y-axis.

object with a surface (bottom panels). A range of accretion rates, parameterized on the X-axis by $\log\left(\frac{L}{L_{\rm Edd}}\right)$ where $L_{\rm Edd} = 4\pi GMc/\kappa_{\rm es}$ with $\kappa_{\rm es} = 0.4$ cm^2 g^{-1} are plotted. A range of surface radii were also considered, $\log(R/R_S) = 0.2 - 0.6$ for neutron stars and $\log(R/R_S) = 0.05 - 0.45$ for the 10 $M_\odot$ object. For each value of $\log(R/R_S)$ and $\log\left(\frac{L}{L_{\rm Edd}}\right)$ three values of $\Sigma_{\rm max} = 10^9, 10^{10}, 10^{11}$ g cm^{-2} were tested. If an instability in any one of these values was calculated to be unstable, that portion of R and L phase space was considered unstable.

These results predict regions of instability in the neutron stars consistent with observation. Bright Z sources, and pulsars are accreting near Eddington and would not be in the region of instability in Figure 4.4. The calculations show further, that

a 10 $M_\odot$ object with a surface behaves similar to a neutron star regarding bursting behavior. The only difference between the two objects is the regions of luminosity where the bursting behavior occurs. From this, NH02 conclude that BHCs are as prone to the instabilities that lead to type I bursts as neutron stars are. NH02 concede that details in the calculations were omitted, but contend these would lead to small variations in the position of the strips of instability, perhaps by a factor of two in $L/L_{\rm Edd}$. Pane A & B in Figure 4.4 show that neutron stars with very low luminosity become stable to bursts. This is not true (see §4.1.2), but NH02 conclude that the recurrence time between bursts in these scenarios would be too long to be of interest for observations in transient X-ray sources. In fact, we did detect X-ray bursts in this region, see Figure 4.7.

4.3.2 Luminosity Calculation

From the 17 neutron stars analyzed we calculate a bursting rate of $\lambda_{\rm NS} = 1.7 \pm 0.4 \times 10^{-5}$ bursts s^{-1}. This is comparable to rates found by other observers (Strohmayer & Bildsten 2003). NH02 predict that the occurrence of type I X-ray bursts is a strong function of $\log\left(\frac{L}{L_{\rm Edd}}\right)$, where $L_{\rm Edd}$ is the Eddington luminosity of the source,

$$L_{\rm Edd} = (4\pi cGM/\kappa)\left(1 - 2GM/c^2R\right)^{-1/2} \text{ ergs s}^{-1} \tag{4.11}$$

where M is the mass of the object, R is the radius of the object, and κ is the opacity of the object. Therefore, $L_{\rm Edd} = 1.3 \times 10^{38} \frac{M}{M_\odot}$ ergs s^{-1} for H rich material[3] with $R \approx 10$ km. The composition of accreting material affects the $L_{\rm Edd}$ by affecting κ. NH02 show that for certain values of $\log\left(\frac{L}{L_{\rm Edd}}\right)$ there can be stable burning and for other values there will be unstable burning leading to type I X-ray bursts. The exact ranges of L for stable accretion depend on the base temperature of the compact object and its radius. For neutron stars, assuming a temperature at the base of the accretion layer of 10^8 K, the region of instability lies between $-1.5 \lesssim \log\left(\frac{L}{L_{\rm Edd}}\right) \lesssim -0.5$.

For each of the sources analyzed, we made a light curve in units of $\log\left(\frac{L}{L_{\rm Edd}}\right)$ for

[3]for solar abundancies with $\sim 70\%$ H, $\kappa \sim 0.45$ and $\left(1 - 2GM/c^2R\right)^{-1/2} \approx 1$.

each observation. We then looked at the fraction of time sources were in the range of L where NH02 predict bursts should occur. In order to calculate the luminosity of the source, we fit a spectrum to a typical observation of the source using XSPEC (Dorman & Arnaud 2001). If distinct states in the source were evident from the source's hardness ratio, then observations from these states were fit separately. Most sources were fit using the Bulk Motion Comptonization (BMC) (Titarchuk, Mastichiadis, & Kylafis 1997) model in XSPEC with absorption and iron emission lines as needed. The BMC model is an analytic model describing Comptonization of soft photons by matter undergoing relativistic bulk-motion. The model describes thermal photons from the inner region of an accretion disk illuminating in-falling matter close to the inner edge of the accretion disk. The model takes into account the thermal photons, then treats the bulk-motion up scattering and Compton scattering of these photons. The fit parameters are the characteristic temperature of the blackbody, the energy spectral index, an illumination parameter describing the amount of in-falling material illuminated by the blackbody, and the normalization of the model. Details of these parameters can be found in Shrader & Titarchuk (1999). The BMC was the best fitting model to most of our data. See Figure 4.5 for a typical spectral fit plot. After fitting a model to the data we obtained the model flux in the $0.2 - 30.0$ keV band (after setting any absorption to zero to get the true model source flux). Using the USA background subtracted, yoke and collimator corrected counting rate for the given observation the flux was calculated for, we are able to calculate a conversion factor from USA rate to source flux. Table 4.3 shows the fit parameters for the spectral fits for each of the sources.

$$1 \text{ USA cts s}^{-1} \approx C \times 10^{-12} \text{ergs cm}^{-2} \text{ s}^{-1} \tag{4.12}$$

Where C is the measured conversion factor. C is between $7 - 12$ for most sources. This method yields a flux of 2.9×10^{-8}ergs cm^{-2} s^{-1} for the Crab Nebula in the $2-10$ keV band, which is within 5% of the accepted value of 2.8×10^{-8}ergs cm^{-2} s^{-1}. Based on this result, we believe the value of C to be correct in our observations at

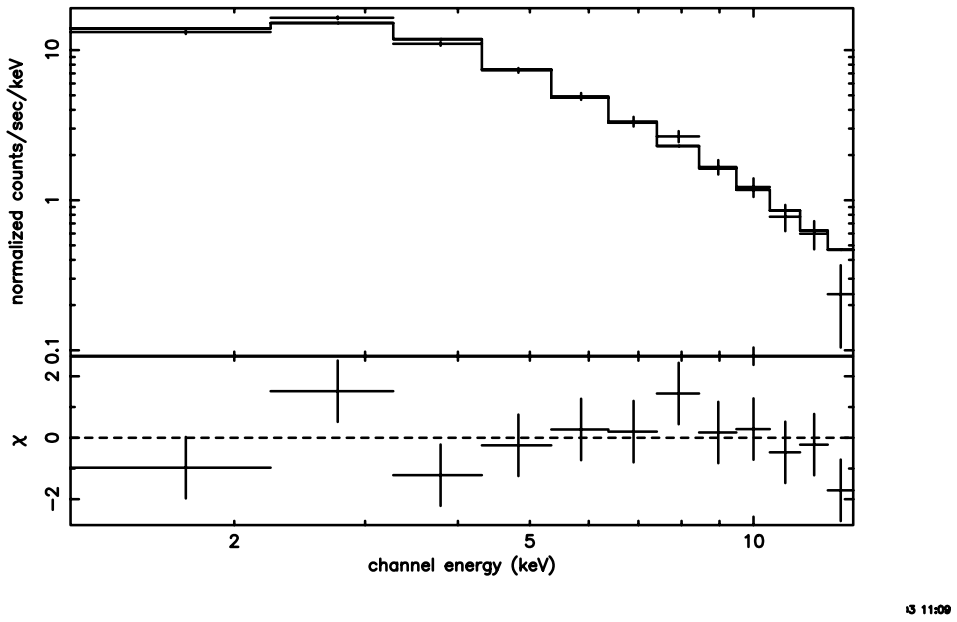

Figure 4.5 Spectral fit to Aquila X-1 in the hard state with USA data. The BMC model was used and the flux predicted from this model was used to calculate the luminosity of the source.

the 10% level. Utilizing this conversion and assuming isotropic radiation we find:

$$\log\left(\frac{L}{L_{\rm Edd}}\right) = \log\left(\frac{(\text{USA rate})(C\times 10^{-12})(4\pi d^2)}{1.3\times 10^{38} M}\right) \tag{4.13}$$

where d is the distance to the source in cm and M is the mass of the compact object in $M_\odot$. For the RXTE BHC data, a conversion factor was calculated to match the count rate per PCU in the PCA standard one data to the count rate seen by USA in the same source for an observation during the same day. The average count rate per observation was used to calculate this conversion. This conversion was calculated for each source to account for different detector response between the two experiments. After the RXTE data were converted to USA rate then the $\log\left(\frac{L}{L_{\rm Edd}}\right)$ was calculated following the method above.

Table 4.3. Fit Parameters for Burst Luminosity Calculation

source	state[a]	C for eq. 4.12	XSPEC Model	Fit Parameters[b]	χ^2/d.o.f[c]	USA Observation
Aquila X-1	soft	6.4	diskbb[d]	2.0 15	3.3	2000_D317_004102_D317_005436
	hard	5.1	bmc[e]	0.7 0.3 0.5 .005	1.0	1999_D207_134455_D207_135341
Cygnus X-1		5.5	bmc	0.31 1.16 0.9 0.05	2.0	1999_D222_041037_D222_042023
Cygnus X-2		6.5	diskbb	1.9 53	1.3	1999_D227_005825_D227_011732
EXO 0748−676		7.5	bmc	1.6 5.4 -7.2 9.1E-4	0.7	2000_D141_130156_D141_131131
GRS 1915+105		14.0	wabs[f]×bmc	4.75 0.68 2.33 0.93 0.27	0.9	2000_D162_110748_D162_111955
GX 17+2		11.8	wabs×bmc	1.2 0.8 0.7 0.4 0.1	1.9	1999_D176_105004_D176_110658
GX 3+1		7.3	bmc	1.24 2.95 0.38 0.08	0.9	2000_D285_233426_D285_234410
GX 340+0		9.8	wabs×bmc	5.68 0.85 2.61 0.98 0.15	0.7	1999_D272_230120_D272_231103
GX 349+2		5.0	bmc	1.07 3.78 8.0 0.11	1.8	1999_D264_151457_D264_152157
GX 354−0		18.2	wabs×bmc	1.05 0.8 0.6 0.75 0.015	0.7	2000_D210_080512_D210_081906
GX 5−1		8.2	wabs×bmc	1.99 1.07 2.51 1.51 0.21	0.6	2000_D271_205630_D271_210501
Rapid Burster		20.4	wabs×(bmc+gaussian[g])	4.37 0.64 1.06 0.18 0.013 7.8 0.9 0.012	0.9	2000_D311_072918_D311_073631
Scorpius X-1		9.7	bmc+gaussian	0.3 1.06 0.44 0.069 5.3 2.5 0.3	0.3	2000_D126_094902_D126_095501
X0614+091		7.9	bmc	0.45 0.02 1.1 0.07	1.5	1999_D351_111731_D351_112803
X1636−536		5.6	bmc	7.2 5.3 0.3 1.1 0.33 0.01	1.3	1999_D172_091440_D172_092953
X1659−298		13.7	bmc	0.68 0.12 0.66 0.019	1.8	2000_D276_210845_D276_211930
X1735−444		6.3	wabs×highecut[h]×bmc	1.2 7.9 8.9 0.39 0.79 0.13 0.019	1.7	1999_D297_122617_D297_124226
XTE J1118+480		4.3	bmc	0.47 0.91 0.42 0.004	2.1	2000_D112_234455_D113_000040
XTE J1550−564	soft	6.1	bmc+gaussian	0.59 0.80 -0.87 0.19 6.74 0.0 0.016	1.4	2000_D123_010701_D123_011501
XTE J1550−564	hard	10.0	diskbb	0.5 85	5.0	2000_D162_101021_D162_102031
XTE J1859+226		10.4	wabs×bmc	0.69 0.52 2.4 -0.76 0.10	1.8	1999_D338_072451_D338_074320

[a]If separate regions were distinct in the USA dataset from HR plots

[b]Notes on individual model components describe parameters.

[c]A 5% systematic error was assumed in the USA spectral data.

[d]Diskbb parameters: temperature at inner edge of disk (keV), normalization, $(R/D)^2 \cos\theta$ where R is the radius of the inner edge of the disk in km, D is the distance in 10 kpc, and θ is the disk inclination.

[e]Bmc parameters: temp of thermal photon (keV), energy spectral index, log of the 'A' parameter, normalization. See Borozdin et al. (1999, Shrader & Titarchuk (1999) for more details on the bmc model.

[f]Wabs parameters: equivalent H column density in 10^{22} nH cm^{-2}.

[g]Gaussian parameters: Centroid value (keV), sigma, normalization.

[h]Highecut parameters: Cutoff energy (keV), e-folding energy (keV).

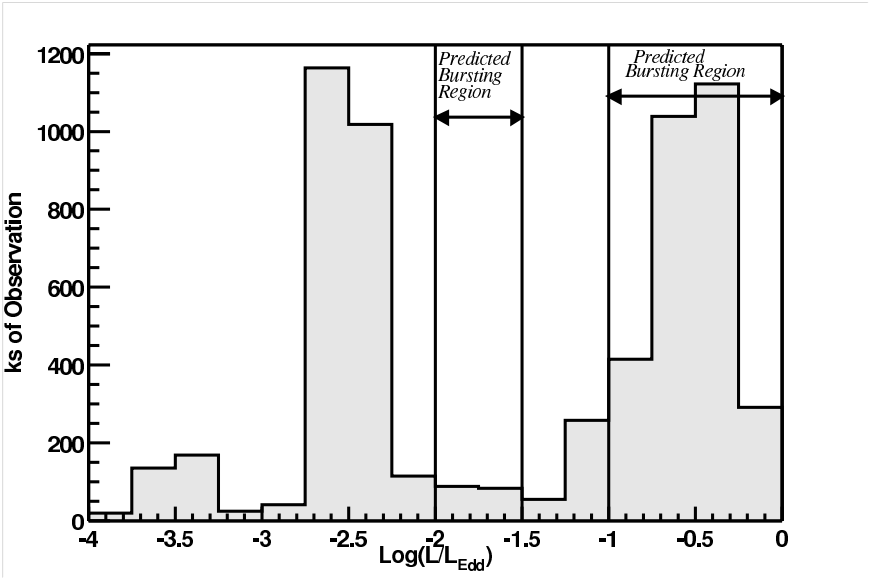

Figure 4.6 Distribution of the log $\left(\frac{L}{L_{\rm Edd}}\right)$ for the USA & RXTE BHC observations. The regions labeled "Predicted Bursting Region" are where NH02 find unstable burning that should lead to type I X-ray bursts if a surface exists on a 10 $M_{\odot}$ object.

Figures 4.6 and 4.7 give the resulting values of log $\left(\frac{L}{L_{\rm Edd}}\right)$ for the BHC data and neutron star data analyzed in this paper. Figure 4.7 also shows the distribution of where we observed bursts in the data.

Luminosity Uncertainties

Minimizing Systematic Errors in the USA Data The first issue in correcting any systematic errors in the data was to estimate the background for each of the observations analyzed. To estimate the background, the USABCK program described in Saz Parkinson (2003) was used. This program creates a file that contains estimated background count rates for each channel and layer in the USA detector. This method of background estimation works very well for most sources in most observing modes. The background model overestimates the background for some observations where the satellite is in an ascending observation with respect to the Earth (see §3.1.4).

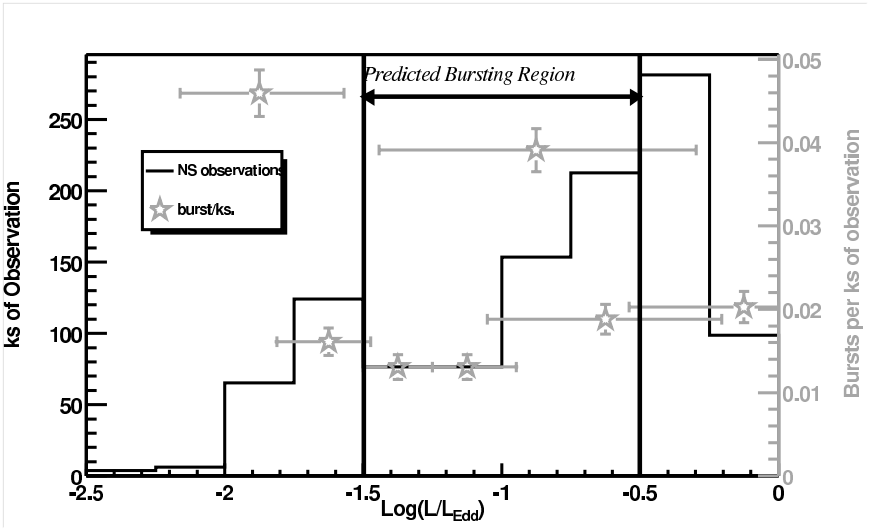

Figure 4.7 Distribution of the log $\left(\frac{L}{L_{\rm Edd}}\right)$ for the USA neutron star observations. The solid histogram contains all the observations of the seventeen neutron stars that we analyzed in this paper. The region labeled "Predicted Bursting Region" is where NH02 find unstable burning that should lead to type I X-ray bursts. The gray stars and the right ordinate show where the nineteen bursts detected by USA were observed, and show a bursting rate in that particular bin. The error bars reflect the uncertainties in the luminosity of the source(s) that had the burst(s) that went into the particular luminosity bin.

For observations where this was found to be a problem, only channels $2-10$ were used, as the model worked quite well in this range. However, a better background model was often needed to get good spectral fits on the sources. If a good spectral fit, χ^2 per d.o.f. ~ 1, was not obtained with a source using the calculated background model then the measured background was used. The instrument pointed off-source for nearly a minute before each observation. These off-source data were used to estimate the background when a more precise subtraction was required. Poorly subtracted background usually shows up in spectral fits as large positive residuals in the hard portion of the spectrum. Background flux makes up anywhere from 1–30% of the total flux for our observations and the uncertainty on the background rate is typically $\sim$ 10%.

The USA data were filtered with a series of cuts after the background was estimated but before any analysis was performed on the data. The cuts were implemented using the MkTimeUSA program described in Reilly (2002). The cuts were designed to select only data that had an acceptable level of background, and sufficient amount of continuous data to be useable. The complete cuts along with a description can be found in Table 4.4. The cuts used in this analysis were lenient, as we wanted the most data possible to detect any and all bursts in a source. Accurate timing and spectral analysis of this data were not essential.

After filtering the data based on the cuts in Table 4.4 the average count rate in each layer and each channel for data and background were calculated for each individual observation. The data were then background subtracted and then corrected for yoke and collimator obstructions, using the average values for that particular observation. These corrected light curves were then compared with RXTE ASM light curves of the same source to correct discrepancies. For some observations, large yoke obscuration or improper background modeling would cause the average USA light curve for a given observation to be obviously in error. When this was discovered, the average count rate for this observation was calculated by interpolating between USA observations and comparing to the ASM light curve. The background subtracted, yoke & collimator corrected count rate is the rate used to calculate the value of C in eq. 4.12. After making these corrections, a reliable conversion from count rate to luminosity can be obtained.

Table 4.4. List of Cuts Used for X-ray Burst Search

Cut parameter	Value	Short Description[a]
MinimumHV	2600	This is the minimum acceptable high voltage in the chamber.
PoleRatioMultiplier	3	In polar observations **RatioMultiplier** = **RatioMultiplier** × **PoleRatioMultiplier**
MaximumOffset	0.5[b]	Maximum allowable pointing offset (in degrees) from directly on source.
MinimumOffset	0	Minimum pointing offset in degrees.
MinimumLimbAngle	5	Minimum angle between the Earth's limb and the pointing vector.
RatioMultiplier	10.5	Maximum ratio between hardest channel top and bottom layers. The higher, the more lenient the cut on soft electron background.
FracAboveBckgnd	3.5	Data are cut where any veto rate is greater than (1+**FracAboveBckgnd**) × (**minimum calculated background**)
MaximumCh15Diff	16	Similar to **RatioMultiplier, but uses** a difference instead of a ratio
TimeBeforeOnSource	4	Amount of time to wait after slewing onto the source before accepting the data.
NbinsAVG	2	Number of seconds to be used in calculating average quantities used for cutting
MinDataLength	2	minimum number of consecutive seconds to be considered a good segment of data
TimeBeforeOffSource	1	Ignores the last 1 second of data before slewing off of the source
MinimumYawAngle	-70	Used to cut out data that are heavily obstructed by the yoke.
MinPVtoTCVRatio	0.58	Minimum ratio of perimeter veto to Coincidence veto rates, to help cut out soft electron data.
RateMultiplier	100	If the current second has a count rate this many times higher than the average rate in channel 15 then it is cut.
PoleMaxCh15DiffMultiplier	3	Same as **PoleRatioMultiplier applied to MaximumCh15Diff**

[a]For a more detailed description of the cut parameter see Reilly (2002).

[b]This parameter was relaxed to 0.7 for some observations.

In order to estimate the uncertainty in the amount of data that fall within the bursting region we use eq. 4.13 to calculate an uncertainty in $\log\left(\frac{L}{L_{\rm Edd}}\right)$ for each source and use this uncertainty with Monte Carlo techniques . The distance and the mass contribute the largest systematic uncertainties to $\log\left(\frac{L}{L_{\rm Edd}}\right)$. The distances and masses used and the errors are given in Table 4.1. Uncertainties in L are estimated using an error estimate on the mass of $\sim 20\%$, if a definite uncertainty is not quoted in Table 4.1, and an uncertainty on the distance of $\sim 20\%$, if a definite uncertainty is

not quoted in Table 4.1. We assume an uncertainty in C of 10%, based on estimates of the Crab luminosity, and assume the uncertainty in USA rate is negligible for all sources except GX 354−0 and the Rapid Burster. For these two sources the counting rate of one was contaminated with counts from the other as discussed in §4.2.2. We were able to deconvolve the two sources since we know the total USA counting rate while pointed at each source and we know the factor of contamination from the source off axis. For observations where one of these two sources was directly observed and the other was not directly observed within a few days, the RXTE ASM counting rate was used to estimate the rate of the off axis source. To do this, the ASM rate was converted to USA rate using 72 ASM counts s^{-1} as one Crab, and 3500 USA counts s^{-1} as one Crab. Therefore, for the Rapid Burster and GX 354−0, an error on the USA rate of 20% was used to calculate the errors on luminosity. This accounts for changes in counting rate of the off axis source between observations, and/or errors in the ASM counting rate.

Monte Carlo Estimate of Data in Bursting Region For each observation, a Gaussian deviate was calculated with the same mean as the measured value of $\log\left(\frac{L}{L_{\rm Edd}}\right)$ and a σ equal to the uncertainty value calculated for that source. Then the fraction of this simulated data in the bursting region was measured. We performed $10,000$ iterations in this manner and calculated the distribution of the fraction of data in the bursting region. We found that the distribution of the amount of data within the bursting region was rather tight, even though the individual errors on $\log\left(\frac{L}{L_{\rm Edd}}\right)$ were large. Figure 4.8 shows the distribution of the Monte Carlo data for 10,000 simulations superimposed over the actual data. Figure 4.8 also shows the distribution of the amount of data in the bursting region for these 10,000 simulations. We found that, to a confidence level of 99.5%, 25% of our BHC data and 42% of our neutron star data fall within the region where one would expect bursts according to Narayan & Heyl (2002). Our analysis assumed that each of the sources analyzed were accreting hydrogen rich material. If the accreted material has a large fraction of helium, as do some bursters, then this will increase the value of $L_{\rm Edd}$.

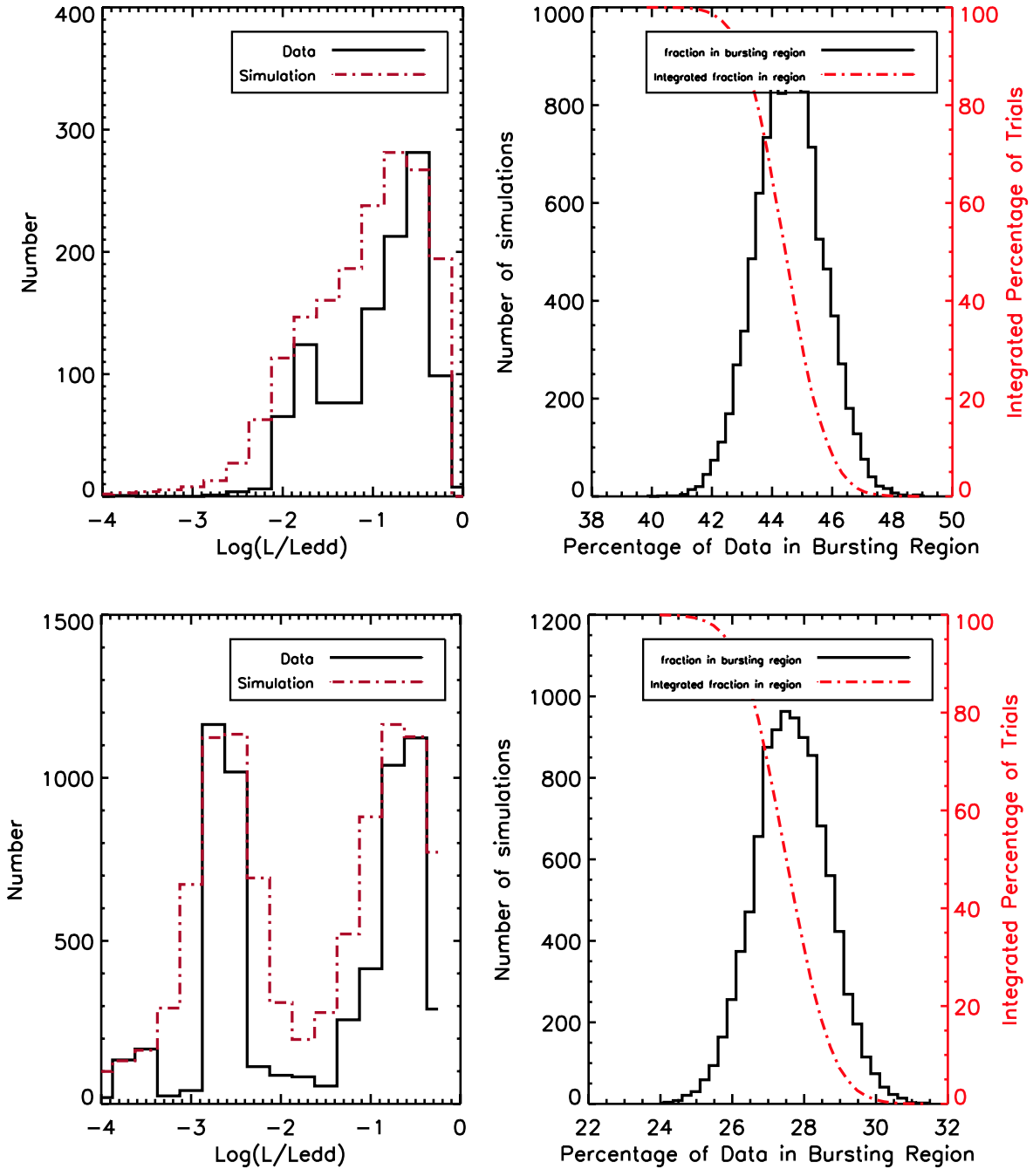

Figure 4.8 Distribution of 10,000 simulated events plotted over the actual data (Neutron star top, BHC bottom). Also shown are the distributions of the amount of data in the bursting region for the 10,000 simulations.

4.3.3 BHC Surface Limit

Narayan & Heyl (2002), calculated what would occur in a $10M_{\odot}$ object if it were assumed to have a surface similar to that of a neutron star, and showed that the rate of bursts should be comparable to the rate in neutron stars. However, they find different regions of $\frac{L}{L_{\rm Edd}}$ where bursts should occur. For a 10 $M_{\odot}$ object with a surface and a base temperature of 10^7 K, the regions where they expect to see bursts are approximately: $-2 \leq \log\left(\frac{L}{L_{\rm Edd}}\right) \lesssim -1.5$ and $-1 \lesssim \log\left(\frac{L}{L_{\rm Edd}}\right) \lesssim 0$. For the BHC data analyzed, at least 25% (1512 ks) of the data fall within this range to a confidence level of 99.5% using Monte Carlo estimates of uncertainty described above. Figure 4.6 shows the distribution of the observations analyzed in this paper in the units $\log\left(\frac{L}{L_{\rm Edd}}\right)$.

Considering only the neutron star data that fall in the luminosity range corresponding to unstable nuclear burning, we find that the 19 bursts occurred in 464 ks of data. This 464 ks value is the 99.5% confidence level on the amount of data within the bursting region based on the Monte Carlo techniques described above, thus accounting for uncertainties in the value of $\log\left(\frac{L}{L_{\rm Edd}}\right)$.

Using these data, we calculate the rate of bursting of neutron stars in the unstable region $\lambda_{\rm NS} = 4.1 \pm 0.9 \times 10^{-5}$ bursts s^{-1}, $R_{NS} = 24 \pm 5$ ks or ~ 7 hours. NH02 predict that a BHC with a surface would display similar bursting behavior to a neutron star, provided both the neutron star and the BHC are within regions of unstable L. In order to estimate the probability that BHCs show/do not show the same bursting behavior as neutron stars in the context of NH02 we used a Bayesian analysis. Given the data we have reported for the number of bursts and the effective observation times for neutron stars and BHCs, the probability for α in a model in which the BHC burst rate is α times that for neutron stars, assuming a flat prior distribution for α, is,

$$P(\alpha) = \int_0^{\infty} \lambda^n e^{-\lambda(T_{NS}+\alpha T_{BHC})} d\lambda \tag{4.14}$$

yielding :

$$P(\alpha) = C(T_{NS} + \alpha T_{BHC})^{-20}; \tag{4.15}$$

Table 4.5. X-ray Burst Rates and Limits from the USA & RXTE Experiments

	All Data [**bursts s^{-1}**]	**Data in Predicted Bursting Range** [**bursts s^{-1}**]
Neutron Stars	$1.7 \pm 0.4 \times 10^{-5}$	$4.1 \pm 0.9 \times 10^{-5}$
Black Hole Candidates[a]	$< 4.9 \times 10^{-7}$	$< 2.0 \times 10^{-6}$

[a]The 95% confidence level upper limit on the bursting rate in the BHCs.

where n is the number of bursts observed, T_{NS} and T_{BHC} are the observing times of neutron stars and black hole candidates respectively, and C is a normalization constant, ensuring that $\int_0^\infty P(\alpha)d\alpha = 1$. Using this result, we find a 95% confidence level upper limit that BHCs have a bursting rate less than 5% of our measured neutron star rate. This is strong evidence that BHCs do not show similar bursting behavior found in neutron stars (as discussed in NH02). Therefore, in the context of NH02 BHCs do not have a surface. The limits and measured X-ray bursting rates can be found in Table 4.5. The columns are the bursting rate or limit calculated using all data analyzed, and then the bursting rate or limit calculated using only the data whose luminosity is within the bursting range calculated by NH02. This is the first such quantitative observational limit placed that quantifies what the lack of bursts means to the BHC theories.

This is not definitive proof of the existence of black holes. Other authors have pointed out that there are other states of matter that may exist in these massive compact objects that do not show X-ray bursts but also do not possess event horizons. See Abramowicz, Kluźniak, & Lasota (2002) for several arguments along these lines. The authors in Abramowicz, Kluźniak, & Lasota (2002) outline arguments that the accreted material could immediately be converted to some exotic form that would not show X-ray bursts (Alford, Rajagopal, & Wilczek 1998; Rapp et al. 1998).

In addition, the argument is made that gravastars, if they exist, (Mazur & Mottola 2002) would be observationally indistinguishable from black holes even though a gravastar exists without an event horizon or a singularity. However, NH02 calculate the density and pressure do not exceed a few times 10^8 g cm^{-3} and 10^{26} ergs cm^{-3}, respectively, even in the most extreme cases considered. It is unlikely that exotic physics is important under these conditions (Glendenning 1997).

4.3.4 Comparison of Narayan & Heyl Theory to Neutron Star Observations

In order to test the validity of the Narayan & Heyl (2002) predictions, we compare the occurrence of the X-ray bursts in neutron stars to the predicted occurrence calculated in Narayan & Heyl (2002). Specifically, after accounting for errors in measuring $\frac{L}{L_{\rm Edd}}$, we see no evidence that any of the observed neutron star bursts occurred when the source was not in the region of unstable burning where bursts would be expected. We investigated the neutron stars in which bursts were not observed, to determine if we expected to see bursts based on the theory put forth in Narayan & Heyl (2002). Of the neutron stars analyzed where we did not see bursts, we acquired 60 ks of data on GX 349+2 when it was in the region of luminosity where one would expect bursts. This is the largest amount of individual neutron star data in the bursting region in which we did not detect any bursts. Again, using Poisson statistics and assuming a bursting rate of $\lambda_{\rm NS} = 4.1 \pm 0.9 \times 10^{-5}$ bursts s^{-1} calculated above, we find that we only have an $\sim$ 10% chance of not seeing a burst in this source. This brings into question the accuracy of bursting region boundaries calculated by NH02. Or, we could have large systematic errors in our calculation of $\log \frac{L}{L_{\rm Edd}}$ for this source. It is worth noting that the USA data of X-ray binaries Scorpius X-1 and GX 349+2 are in the bursting region 43% and 74% of the time respectively (99.5% confidence level). In fact, one could use the fact that these are neutron stars that have never been observed to burst to place limits on the distances to these sources. Assuming a mass of 1.4 M$_\odot$, GX 349+2 must not reside between $5.9^{+0.6}_{-0.5}$ – $9.7^{+1.0}_{-0.8}$ kpc and Scorpius X-1 must not reside between $2.5^{+0.6}_{-.4}$ – $4.1^{+1.1}_{-0.6}$ kpc. The errors are based on 1 σ deviations in the

observed rate from these sources. Previous distance estimates for GX 349+2 place it around the galactic center 5–8.5 kpc (Christian & Swank 1997; Cooke & Ponman 1991), and estimates place Scorpius X-1 at 2.8 ± 0.3 kpc (Geldzahler, Fomalont, & Bradshaw 1999). Both of these estimates place these sources near the boundaries of our excluded region. The other two neutron star systems that we analyzed and have never been observed to burst, GX 340+0 and GX $5-1$ only spend $< 15\%$ and $< 2\%$ of their time in the bursting region. Therefore, it is likely that these sources are neutron stars that rarely, if ever, burst.

4.4 Burst Rates and Limits Conclusions

We present the burst catalog of the USA experiment X-ray binary data, and calculate limits on the rate of X-ray bursts in BHCs. We detected nineteen X-ray bursts in seven neutron stars. From our neutron star data we conclude that the average time between bursts in neutron stars is 59.1 ks, $\lambda_{NS} = 1.7 \pm 0.4 \times 10^{-5}$ bursts s^{-1}. The BHC data scanned showed no evidence for bursts. Therefore, we place a 95% confidence limit on the burst rate in BHCs to be $\leq 4.9 \times 10^{-7}$ bursts s^{-1} or $R \geq 470$ ks between bursts, based on USA and RXTE BHC data. The value of this upper limit is that it is at a level that is not easily pushed lower. This is because most BHCs are transients that, with some exceptions, last less than a few megaseconds. The few BHCs that are relatively steady (primarily Cygnus X-1 but arguably GX 339−4 and GRS 1915−105) do not have more than a few tens of megaseconds of observation. Thus, $10^{-6} - 10^{-7}$ bursts s^{-1} is a rough order of magnitude for the attainable limit. A sensitive all sky monitor might eventually reach a slightly lower value.

Applying the theoretical framework of Narayan & Heyl (2002), who claim that if BHCs have surfaces they will burst similarly to neutron stars if both are in a regime of unstable nuclear burning, we find that the BHCs in this regime do not burst with a rate greater than 5% of the rate of neutron star bursting to a confidence level of 95% based on our limits. Therefore, these observations, analyzed according to the theory proposed by Narayan & Heyl (2002) leads us to believe that BHCs do not have a surface, as described in NH02, to a very high confidence level.

4.5 Analysis of USA Type I X-ray burst data

4.5.1 Spectral Analysis

We performed spectral analysis on the nineteen X-ray bursts detected in the USA data (Table 4.2). For all the analysis, the persistent emission was used as a background file for the burst. Therefore, the persistent emission is subtracted from all burst data giving us the best measurements of the true burst emission.

Each X-ray burst was broken down into 0.5 s segments. These segments were then converted to pulse height analysis (PHA) channels using the FTOOL *extractor*. Then, each segment was analyzed using XSPEC (Dorman & Arnaud 2001) to fit a blackbody spectrum to the segment. The burst will show temperatures hotter than the true blackbody temperature due to hardening of the spectrum from the surrounding hot plasma. Details of this effect are described in Titarchuk & Shaposhnikov (2002), Haberl & Titarchuk (1995), and Lewin, van Paradijs, & Taam (1995). One can perform calculations to estimate this hardening factor to get the actual temperature and radius of the neutron star. This method can be used to place constraints on the mass-radius relation of neutron stars (Haberl & Titarchuk 1995; Titarchuk & Shaposhnikov 2002). This analysis is beyond the scope of this dissertation and is suggested for future study by the USA experiment science working group.

This analysis was originally performed to distinguish between X-ray bursts from the Rapid Burster and GX 354−0, as described in §4.2.2. However, the only sure distinguishing characteristic between the two bursters is the presence of radius expansion in the GX 354−0 bursts. Unfortunately, we were not able to detect radius expansion in any of the bursts that we measured in the Rapid Burster/GX 354−0 field of view[4]. Therefore, these calculations did not allow us to separate the bursts from the two sources. However, we were able to measure the blackbody temperature and normalization[5] throughout the bursts for each of our nineteen bursts. The results

[4]Radius expansion is evident when the temperature of the blackbody decreases at the same time the blackbody normalization increases (Galloway 2003).

[5]*Bbody* normalization gives information about the luminosity of the source. Normalization = L/D^2 where L is the luminosity of the source in units of 10^{39} ergs s^{-1} and D is the distance to the source in units of 10 kpc.

are plotted in Figures 4.9, 4.10, 4.11. These figures show the burst temperature and normalization from spectral fitting for fits that had a reduced χ^2 less than 2.0 (for 3% systematic errors), calculated error on the temperature less than 1.0 keV, and a calculated error on the normalization less than 1.0, (10^{37} ergs s^{-1} kpc^{-2}). For one burst, from a Rapid Burster observation, we were not able to calculate good blackbody parameters throughout the burst. This was due to contamination from a type II burst from the Rapid Burster occurring at the same time.

4.5.2 Timing Analysis

Timing analysis was performed on each X-ray burst by creating a noise subtracted, dead time corrected, power spectrum density distribution (PSD) for each 0.5 s segment in every burst. The PSD were made using data from USA PHA channels 1–14, with 96 μs bins, rebinning from 1.04–2000 Hz. The PSD were searched for oscillations in the range 100–1000 Hz by visually scanning each PSD for evidence of a peak, the signature for a QPO. No burst oscillations were detected in any of the nineteen bursts searched. Burst oscillations have been detected before in some of our sources: MXB 1659−298 at 567 Hz in $\sim$ 33% of its bursts, Aquila X-1 at 549 Hz in $\sim$ 18% of its bursts, GX 354−0 at 363 Hz in $\sim$ 40% of its bursts, and a possible detection in GX 3+1 at 589 Hz (Muno et al. 2002; Strohmayer & Markwardt 1999).

Given the fraction of the bursts that oscillations have been detected in for past observations it is likely that the USA data do not contain any bursts that contained oscillations. More detailed studies could be performed by trying to use Z-transforms which consist of period folding the light curve onto itself with a varying period to account for the changes in the burst oscillation. Detailed studies such as these, may find oscillations that were not detectable in the PSD. This analysis is, however, beyond the scope of this dissertation and is reserved for future researchers.

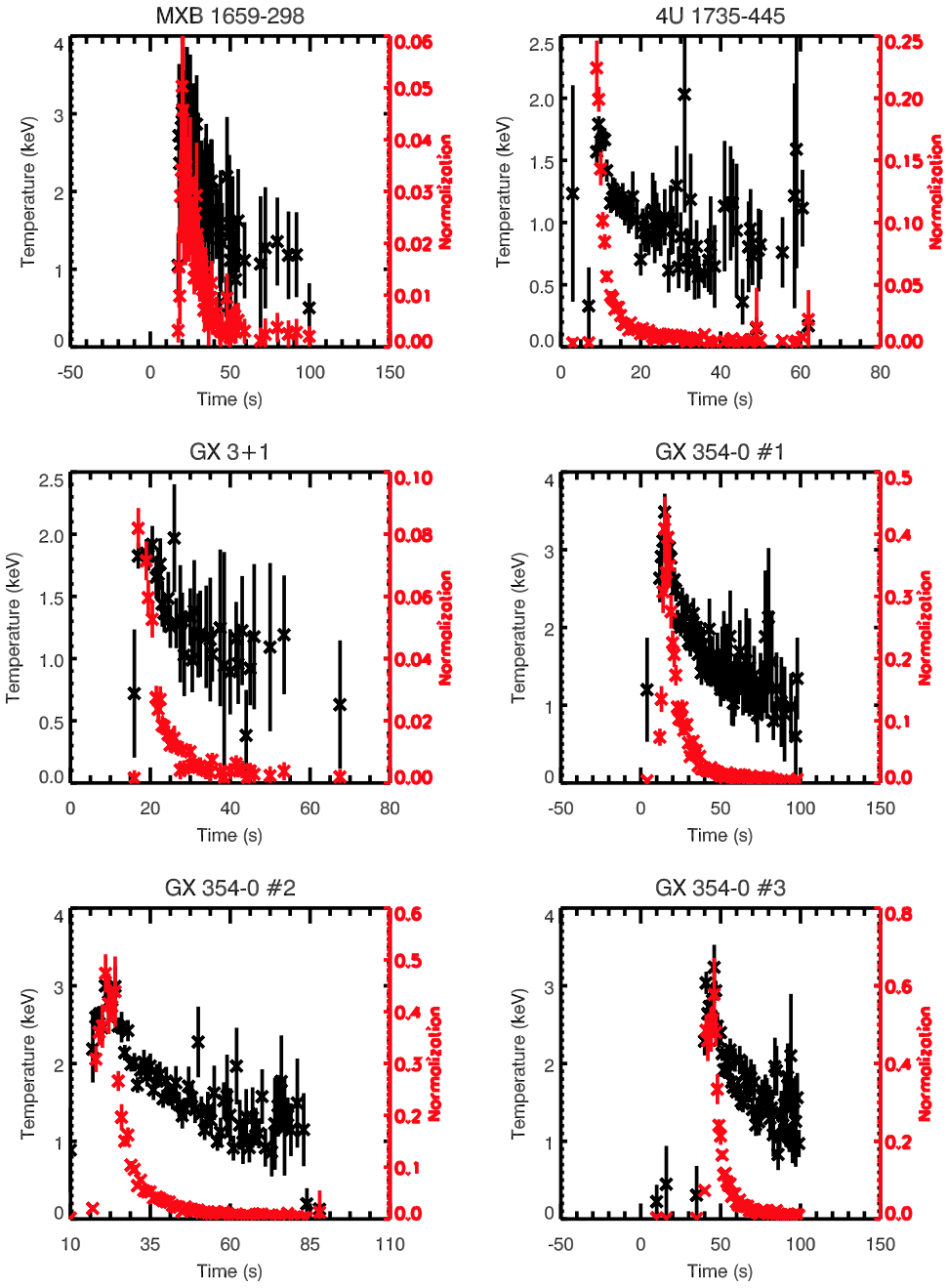

Figure 4.9 Blackbody temperature and normalization during type I X-ray bursts as measured by the USA experiment. The temperatures and normalizations were calculated in XSPEC using the *bbody* model. Labels above the plots tell which X-ray burst is being analyzed in the plot. More details of the X-ray burst can be found in Table 4.2.

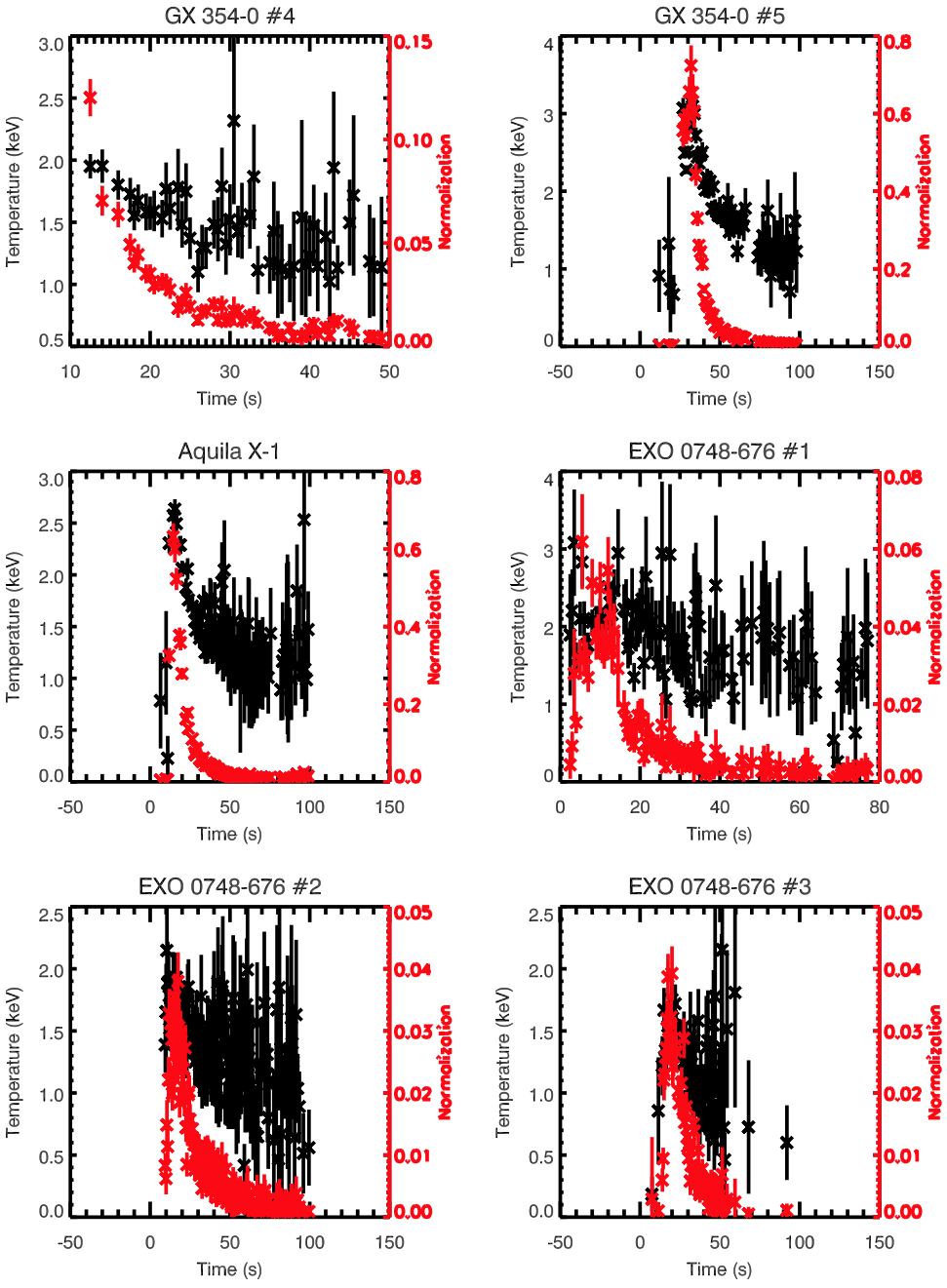

Figure 4.10 Continuation of Figure 4.9 showing the blackbody behavior of type I X-ray bursts.

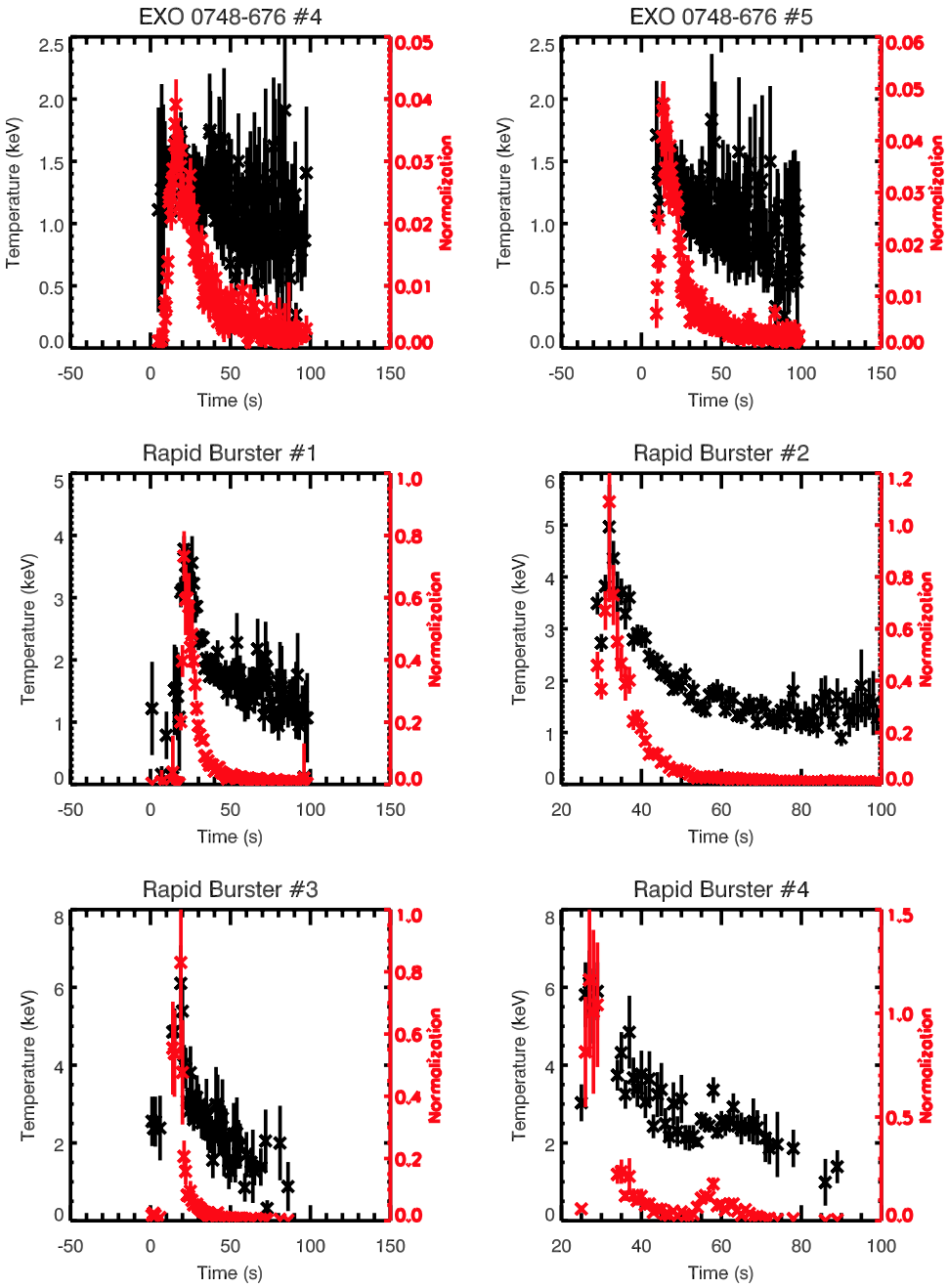

Figure 4.11 Continuation of Figures 4.9, 4.10 showing the blackbody behavior of type I X-ray bursts.

Chapter 5

Soft X-ray Transient Outbursts

5.1 Introduction to SXT Theory in LMXBs

A Black hole or neutron star in a LMXB system accretes matter away from its companion and surrounding plasma. Infalling matter accumulates in an accretion disk as it spirals toward the compact object if the matter's angular momentum is too large to allow the matter to fall directly to the surface. This condition is satisfied when the circularization radius

$$R_{\rm circ} = \frac{J^2}{GM}, \tag{5.1}$$

is larger than the size of the accretor, where J is the specific angular momentum of the infalling material, and M is the mass of the central object. In other words, for a given J, the material can orbit at $R_{\rm circ}$. As the accreting matter falls inward it must lose energy faster than it loses angular momentum to stay in a disk geometry, therefore the angular velocity of the infalling material increases. Thus, accretion proceeds as a series of circular orbits with decreasing J. Some process often modelled as viscosity in the disk allows for dissipation of the energy and transport of the angular momentum outward back towards the companion star.

Theories about the properties and causes of this viscosity are debated. Overwhelming evidence suggests that the viscosity is far greater than expected from ordinary molecular viscosity. For a detailed review on this subject see Lewin, van

Paradijs, & van den Heuvel (1995), Done (2002) and references therein. Friction in the accretion disk caused by the viscosity makes the material get hot and emit a blackbody spectrum. This spectrum can be seen in X-rays with temperatures near one keV.

The story does not end there. If the inner edge of the disk were the only radiator then we would see sharp total eclipses and few partial eclipses in LMXB systems. However, the opposite is seen (Lewin, van Paradijs, & van den Heuvel 1995), partial eclipses are sometimes seen and steep-sided total eclipses are rare. This gives way to a corona model where the inner edge of the disk heats up and gives off a blackbody spectrum, and the more extended corona, made up of high energy electrons, Compton upscatter the photons produced by the blackbody and radiate higher energy photons with a power law spectrum. The exact position of the optically thin hot corona is not well known. Some theories place the corona between the inner edge of the accretion disk and the innermost stable orbit. This region is referred to as the transition layer (TL). Other theories involve the corona surrounding the entire accretion disk. Some theories even predict the corona will form in loops winding in and out of the accretion disk. In 4U 1630−47 X-ray dips were observed in its 1998 outburst lasting from 4–160 seconds (Tomsick, Lapshov, & Kaaret 1998). These dips were seen to only occult the soft blackbody photons, therefore lending support that there is an extended corona responsible for the harder component of the spectra (Tomsick, Lapshov, & Kaaret 1998). No dips were seen in the X-ray light curves during the 1999 outburst.

The behavior of these two components of a LMXB are what lead to changes in the spectrum during an outburst. The following paragraphs will give the reader a general idea of the progression of different states throughout an X-ray outburst. More detailed reviews can be found in Reilly (2002), Done (2002) and Homan et al. (2001).

At the beginning of the outburst, the accretor is in a low-hard state (LS). The LS is characterized by a hard spectrum, dominated by a power law, with a low X-ray flux. Timing properties measured by power spectral density (PSD) during the LS will show large broadband variability often accompanied by low frequency quasi-periodic oscillations (LFQPOs). The X-ray spectrum is the result of inverse Comptonization of the seed photons from the accretion disk occurring within the corona. Relativistic

jets are sometimes seen during this state in some sources, which are then called microquasars.

During the outburst, the accretor may pass through an intermediate state (IS), and even a very high state (VHS). In these states the energy spectrum is dominated by the blackbody component originating from a very hot inner-edge on the accretion disk. There is often a weak power law component. The PSD during this state usually show low variability. The X-ray intensity is higher in the VHS than in the IS. If the VHS is present in an outburst it will be during the brightest portion of the outburst. These states are not observed in all outbursts.

Next, the source goes into a high-soft state (HS). The energy spectra of this state is very close to the IS, however the inner edge of the accretion disk is in as close to the inner-most stable circular orbit (ISCO) as it can get and the blackbody component totally dominates the spectrum. A very weak power law component may be detected. There is slightly less timing variability in this state than the IS, with possible LFQPOs and/or HFQPOs.

As the outburst fades, the flux decreases and the spectrum gets harder, the source returns to the LS and then enters the quiescent state (QS). The source is usually barely detectable in the QS, the inner edge of the accretion disk is far away from the compact object, and the emission that does come from the source is dominated by the optically thin corona giving a power law energy spectrum. See Figure 5.1 for a cartoon outlining the main properties and differences in each of the X-ray transient's states.

It has been found that when a LMXB is in a HS, the hardness and flux are correlated (Zdziarski et al. 2002). This supports the theory that when the BHC is in the soft state, the inner radius of the disk extends to the innermost stable orbit (Meyer, Liu, & Meyer-Hofmeister 2001). The temperature near the inner radius is very hot and the spectrum of the source is dominated by this blackbody contribution. Consequently, changes in the accretion disk itself dictate the behavior of the system. As a result, as the temperature of the disk increases the flux increases and the spectrum shifts to a harder spectrum.

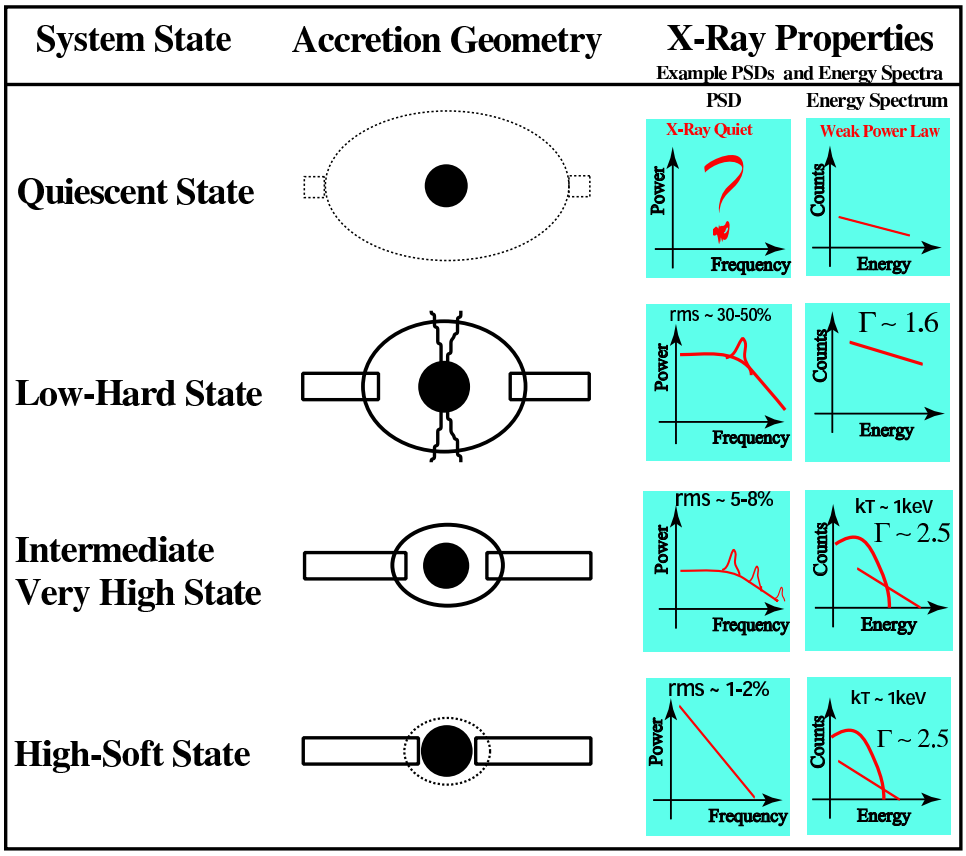

Figure 5.1 A cartoon showing one common model geometry, timing and spectral properties of a soft X-ray transient in its various states. The filled black circles in the geometry cartoon represent the compact object. The lines coming from the compact object in the hard state represent jets. The column labeled PSD gives an example power spectrum density distribution (PSD) of the transient in that state. The Energy Spectrum column shows the main properties of the X-ray spectrum of a source in the given state, where T is the blackbody temperature and Γ is the power law index (count rate $\propto$ energy$^{-\Gamma}$). Figure courtesy Reilly (2002).

On the other hand, in the LS, the hardness and flux have been found to be anti-correlated. When a BHC is in this state, the inner radius of the accretion disk is far away from the least stable orbit (Meyer, Liu, & Meyer-Hofmeister 2001), so the temperature of the inner disk is not as high. Thus, the relative contribution of the blackbody emission to total energy emission is low. Consequently, changes in the plasma of the corona, not the disk itself dictate the behavior of the spectrum. Therefore, if the amount of photons from the disk increase, the net result is to increase cooling of the corona by Compton upscattering, resulting in a softer power law spectrum.

5.2 4U 1630−472 Outburst Analysis

5.2.1 Introduction

4U 1630−47 is a member of the transient class of low mass X-ray binaries (LMXBs). The class of the compact object and the companion is, however, unknown (R.N.Ogley 1998). The lack of type I X-ray bursts in addition to characteristics in the X-ray timing and spectrum suggest that the compact object is a black hole candidate (BHC) (see §4.1, §4.3, Parmar, Stella, & White (1986), and Kuulkers, van der Klis, & Parmar (1997)). The interstellar reddening of 4U 1630−47, measured by X-ray absorption, is high. The source is assumed to be at the distance of the Galactic center or beyond, ($\sim$ 10 kpc) making detection of the companion star difficult. 4U 1630−47 was first discovered in 1972 (Jones et al. 1976) and has undergone frequent outbursts since, recurring every 450–700 days. These semi-regular outbursts with such a short recurrence time are uncommon in BHCs. In these soft X-ray transient (SXT) sources such as 4U 1630−47 the outbursts are important to study since the source nearly disappears in quiescence and we can gain information on the physical properties of the source by looking at different timing and spectral features as the source becomes bright and then decays to quiescence.

The spectrum of 4U 1630−47 has two main components: an (ultra) soft blackbody component and an (ultra) hard power law component. Near the maximum of

the outburst the soft component dominates and fades away as the hard component dominates towards the end of the outbursts. See Tomsick & Kaaret (2000) for a review of the 1998 outburst. LFQPOs of a few Hz have also been detected in this source near the maximum of its outburst (Tomsick & Kaaret 2000).

We see hard X-ray emission in one *Compton Gamma Ray Observatory* BATSE occultation observation occurring at the very beginning of the 1999 outburst. Better detection from BATSE occured during the 1998 outburst (Hjellming et al. 1999). During the 1998 outburst, radio emission was detected just as the source was making a transition from hard to soft emission (Hjellming et al. 1999). The radio data were able to get a precise location of this source: (J2000) RA = $16^h34^m01^s.6\pm0.05^s$, Dec = $-47°23'33'' \pm 2''$ (VLA) or RA = $16^h34^m01.61^s \pm 0.02^s$, Dec = $-47°23'34.8'' \pm 0.3''$ (ATCA). In 1998 a detection of the IR component of 4U 1630−47 was reported using SOFI by Augusteijn in (Augusteijn, Kuulkers, & van Kerkwijk 2001). We were not able to find IR or radio data on the 1999 outburst.

In this section, we discuss the timing and spectral properties of the 1999 outburst of 4U 1630−47 using data from the *Rossi X-ray Timing Explorer* (RXTE) (§3.2) and the *Unconventional Stellar Aspect* (USA) (§3.1) experiments. We compare the results of the 1999 outburst to the results of previous outbursts. During the beginning and middle of the outburst the soft X-ray flux is high, but then gets dominated by the hard power law tail as the outburst decays with an e-folding time of 13.8 days. In the 1999 outburst there is a second peak that is brighter than the first peak. This is also the case in the 1996 outburst, but opposite the 1998 and 2001 outbursts where the second peak is dimmer than the first peak. In the 1999 outburst we also see a ~ 1 Hz QPO at the beginning of the outburst. Similar QPOs of a few Hz were seen in the 1998 outburst (Dieters et al. 2000; Tomsick & Kaaret 2000).

5.2.2 RXTE Observations

Data from all three instruments aboard the RXTE experiment were used in analysis of the 1999 outburst. The outburst can be clearly seen in the ASM light curve of this source, and ASM observations triggered the target of opportunity (TOO) observations

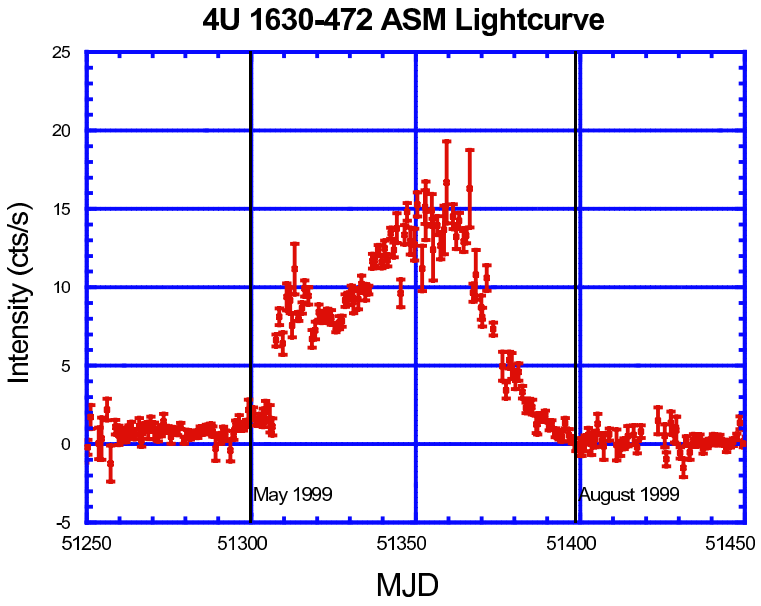

Figure 5.2 The ASM dwell by dwell light curve of the 1999 4U 1630−47 outburst.

that collected data throughout the outburst. Figure 5.2 shows the ASM observations of 4U 1630−47 during the 1999 outburst. Figure 5.3 shows the ASM light curve for 4U 1630−47 from 1996–2001. The PCA and HEXTE data were used to fit X-ray energy spectra to characterize the changes of the states of the source. The PCA data were also analyzed for timing information to characterize the source state and search for QPOs. See §3.2 for more information on the RXTE experiment. Figure 5.4 shows the PCA light curve superimposed over the ASM light curve in the top pane; the bottom pane shows the HEXTE light curve, and data from the BATSE hard X-ray experiment (Paciesas et al. 1989).

We looked at a total of 47 RXTE observations of 4U 1630−47 during the 1999 outburst. The observations were, on average, 2.8 days apart, spanning from 1999 May 8 to 1999 September 15. Each observation was, on average, 800 seconds long. For spectral analysis we used Standard 2 mode data and looked at energy ranges 3–50 keV with PCA and 28–264 keV with HEXTE. For timing analysis, no energy cuts were made. The datamode used was E_125us_64M_0_1s for all observations that were observed with this mode. For observation 40418-01-01-00 we used datamode

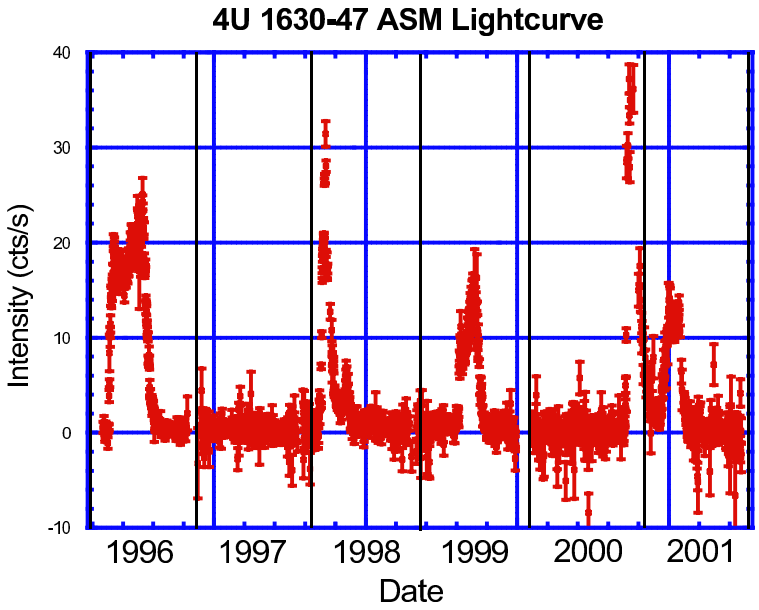

Figure 5.3 The ASM dwell by dwell light curve of 4U 1630−47 showing outbursts in 1996, 1998, 1999 and 2000/2001. The profiles of the 1996 and 1999 outbursts are similar, and the profiles of the 1998 and 2000/2001 outbursts are similar.

B_8ms_16A_0_35_H_4P. These datamodes correspond to event data with 125 μs resolution with 64 energy channels starting at channel 0, and binned data with $\sim$ 8 ms resolution with 16 energy channels starting at channel 0, respectively. For more information on how RXTE data is organized and RXTE datamodes see §3.2.2.

5.2.3 USA Observations

We looked at a total of 101 USA observations of 4U 1630−47 during the 1999 outburst. The observations were taken in two main groups. The first 20 were taken very near the peak of the outburst with the remaining taken during the end of the decline of the outburst. The total time of USA data after cutting out periods of high background is $\sim$ 46 ks. The USA observations in relation to the outburst can be see in fig 5.4 in the top pane. All USA data analyzed were taken in either datamode one or two, best for timing analysis. See §3.1 for more information on the USA experiment.

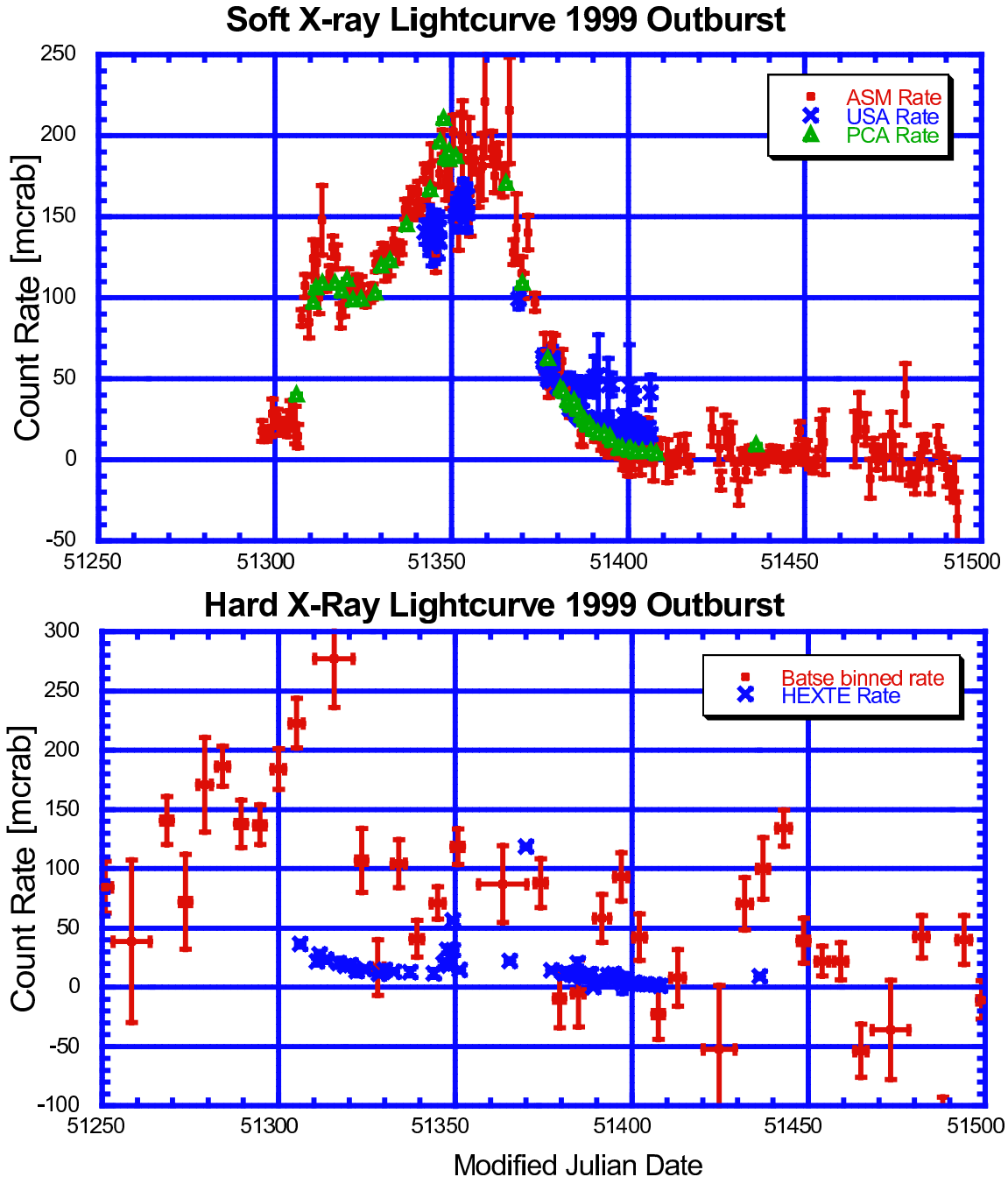

Figure 5.4 The 1999 outburst light curve of 4U 1630−47. The top pane shows the behavior of the soft X-rays. Including data from the ASM, PCA and USA detectors. The bottom panel shows the behavior of the hard X-ray flux, including data from BATSE occultation data and the HEXTE detectors. The BATSE data are binned so that for every point there are six occultation measurements.

The USA data were used in addition to the RXTE data to search the 1999 outburst for signs of X-ray dips. X-ray dips have been seen in the past in this source, however, we did not detect any dips in the RXTE or the USA light curves.

5.2.4 Data Analysis

Spectral Analysis

The RXTE PCA and HEXTE data were used for spectral analysis. The USA data were analyzed also, but the spectral fits from the USA data were not as good as the combined PCA/HEXTE fits, and we did not glean much useful information from these fits. Therefore, all of the energy analysis we discuss will be results from the RXTE data.

PCA channels 0–3 and 85–128, were ignored as bad, therefore we used PCA data in the energy range $\sim 3 \sim 50$ keV. HEXTE channels 14–62 were used in analysis, corresponding to the energy range $\sim 30 \sim 250$ keV. Therefore, using RXTE data we were able to fit spectra in the range $\sim 3 \sim 250$ keV. We placed the following cuts on the data so that we only analyze data taken with the:

- *TIME_SINCE_SAA* > 30.0 or < 0.0
- *ELECTRON0* < 0.1
- *ELV* > 10.0
- *OFFSET* < 1.5

These cuts were designed to minimize background contamination, which was estimated following the standard RXTE data analysis cookbook described in §3.2.2.

After selecting the data and creating pulse height analysis (PHA) files for each observation, we began to analyze the X-ray spectrum using XSPEC (Dorman & Arnaud 2001). We fit the X-ray spectra with a model that has a component for the soft thermal radiation coming from the inner edge of the accretion disk, and a component for the non-thermal component coming from the hot optically thin corona. We obtained good results with the model: $constant \times wabs(diskbb + comptt + gaussian)$

for nearly all observations[1] For some observations reflection of the X-rays by the accretion disk was evident and the component *pexriv* was added to achieve a good fit. See Titarchuk (1994) for a description of the *comptt* model, Mitsuda et al. (1984) for the *diskbb* multi-color blackbody model, and Magdziarz & Zdziarski (1995) for information on the *pexriv* model. The *wabs* model component accounts for the hydrogen absorption to the source, and *gaussian* accounts for a strong iron line emission that is sometimes seen in the spectrum of 4U 1630−47. Table 5.1 shows the results of the various fits to the different observations of this source. For the *comptt* model the redshift was fixed to zero, the seed photon temperature was locked to the *diskbb* temperature, and the geometry switch was fixed to one, to represent a system with a disk geometry. For the *pexriv* model component the temperature of the disk in Kelvin was fixed to $1.16 \times 10^7 \times$ the *diskbb* temperature (given in keV).

[1]We were not able to obtain good reduced χ^2 values for eleven of the RXTE observations for any spectral model. We believe these observations may have had incorrect background information, other data problems, or the models were not sufficient to describe the data.

Table 5.1. Energy Spectra Fit Parameters From 4U 1630−47 1999 Outburst

Obs. 40418_01	Time (MJD)	χ^2 per DOF[b]	H[d] Col.	Disk T (keV)[c]	Disk Norm	CompTT kT (keV)	Optical Depth	CompTT Norm	Line E (keV)	Line σ (keV)	Line Norm	HEXTE A constant	HEXTE B constant
_01_00	51306.1	0.9	6.1	1.0	1.8E+01	20	2.5	1.2E-02	6.4	0.6	2.7E-03	0.8	0.8
_03_00	51310.8	0.9	6.7	1.2	1.6E+02	41	0.8	5.6E-03	–	–	–	0.8	0.8
_04_0	51311.6	1.4	6.6	1.2	1.6E+02	44	0.9	4.5E-03	5.8	0.5	2.8E-04	0.8	0.8
_05_0	51313.4	1.6	6.6	1.2	1.9E+02	40	0.9	5.3E-03	5.9	0.5	3.3E-03	0.8	0.8
_07_00	51316.9	1.1	8.0	1.2	2.9E+02	43	0.7	3.1E-03	6.4	0.5	1.9E-03	0.8	0.8
_08_00	51318.9	1.2	8.0	1.1	2.9E+02	18	2.0	9.8E-03	–	–	–	0.8	0.8
_09_00	51320.3	0.8	8.7	1.2	3.0E+02	52	0.7	3.0E-03	–	–	–	0.8	0.8
_10_00	51322.0	1.2	9.3	1.1	4.6E+02	43	0.7	3.1E-03	6.4	0.5	1.9E-03	0.8	0.8
_11_00	51324.3	1.0	9.3	1.1	4.1E+02	18	2.0	7.5E-03	6.4	0.5	1.5E-03	0.8	0.8
_13_00	51328.5	0.9	9.2	1.1	3.8E+02	27	1.5	3.3E-03	–	–	–	0.8	0.8
_14_00	51330.0	1.5	8.6	1.1	3.7E+02	51	0.7	2.8E-03	–	–	–	0.8	0.8
_15_00	51332.6	1.1	9.8	1.1	4.3E+02	22	1.7	5.1E-03	6.4	0.1	2.1E-04	0.8	0.8
_16_00	51337.2	0.9	8.9	1.2	3.8E+02	34	1.1	3.6E-03	–	–	–	0.8	0.8
_17_00	51344.0	1.1	9.1	1.2	4.1E+02	75	0.4	1.3E-03	–	–	–	0.8	1.0
_18_00	51348.2	1.6	9.4	1.2	4.0E+02	67	0.6	2.3E-03	–	–	–	0.8	0.8
_18_03[a]	51347.7	1.5	9.6	0.1	5.8E-02	54	0.9	3.2E-02	6.4	0.6	3.8E-03	0.8	0.9
_18_04	51365.4	1.2	9.6	1.2	4.5E+02	56	0.5	2.5E-03	6.4	0.5	4.1E-03	0.8	0.8
_18_05	51351.2	1.9	9.3	1.2	4.0E+02	63	0.6	1.9E-03	–	–	–	1.0	0.8
_21_0	51377.3	1.1	6.7	1.0	2.2E+02	32	1.1	4.7E-03	6.4	0.2	1.0E-04	0.8	0.8
_23_0	51381.6	1.4	6.0	1.0	1.7E+02	35	1.0	4.1E-03	6.4	0.5	8.7E-04	0.8	0.8
_24_00	51382.7	1.3	6.0	0.9	1.9E+02	101	0.3	1.2E-03	–	–	–	0.8	0.8
_25_00	51383.7	1.8	6.0	0.8	2.9E+02	139	0.1	1.1E-03	6.4	0.6	1.5E-03	1.0	0.8
_26_00	51384.7	1.7	9.8	0.7	1.5E+03	113	0.3	2.0E-03	6.4	0.6	3.4E-03	0.8	0.8
_27_00	51385.5	1.1	6.0	0.8	1.7E+02	18	2.0	9.4E-03	6.4	0.6	1.6E-03	0.9	0.8
_28_00	51386.6	0.9	6.0	0.7	3.5E+02	42	0.9	4.2E-03	6.4	0.6	1.9E-03	1.1	0.9
_29_00	51387.6	1.0	6.0	0.8	2.4E+02	32	1.2	4.7E-03	–	–	–	1.0	1.1
_30_00	51388.3	1.1	6.0	0.6	5.6E+02	30	1.2	5.5E-03	6.4	0.6	2.0E-03	1.2	1.2
_32_00	51390.1	1.3	6.0	0.8	1.4E+02	21	1.8	5.1E-03	6.4	0.6	1.4E-03	0.8	0.8
_33_00	51391.5	1.2	6.0	0.6	5.3E+02	38	1.0	3.7E-03	6.4	0.6	1.5E-03	0.9	0.8
_34_00	51393.2	0.9	6.0	0.6	3.3E+02	28	1.8	4.7E-03	6.4	0.6	1.5E-03	0.8	0.8
_36_00	51395.5	1.0	10.0	0.6	7.4E+02	51	0.9	2.1E-03	6.4	0.6	1.3E-03	0.9	1.2
_38_00	51398.2	0.7	10.0	0.4	9.2E+03	31	1.4	3.0E-03	6.4	0.6	7.5E-04	1.1	0.8
_39_00	51400.1	1.6	6.0	0.0	7.2E+03	38	0.8	4.2E-02	–	–	–	1.1	0.8
_40_00	51400.7	0.9	9.5	0.5	9.1E+02	61	0.9	9.5E-04	6.4	0.6	1.3E-03	0.8	0.8
_42_00	51404.0	1.0	7.9	0.6	3.9E+02	47	0.9	9.7E-04	6.4	0.4	7.7E-04	0.8	0.9
_45_00	51436.1	1.4	9.8	0.3	6.0E+03	18	2.2	8.5E-03	6.4	0.4	7.4E-04	0.8	0.8

[a]The model for this fit also included *pexriv* in order to get a good fit.

[b]All of these fits include a 0.02% systematic uncertainty used to calculated the χ^2.

[c]The *comptt* T0 value was set equal to this value.

[d]10^{22} atoms cm^{-2}.

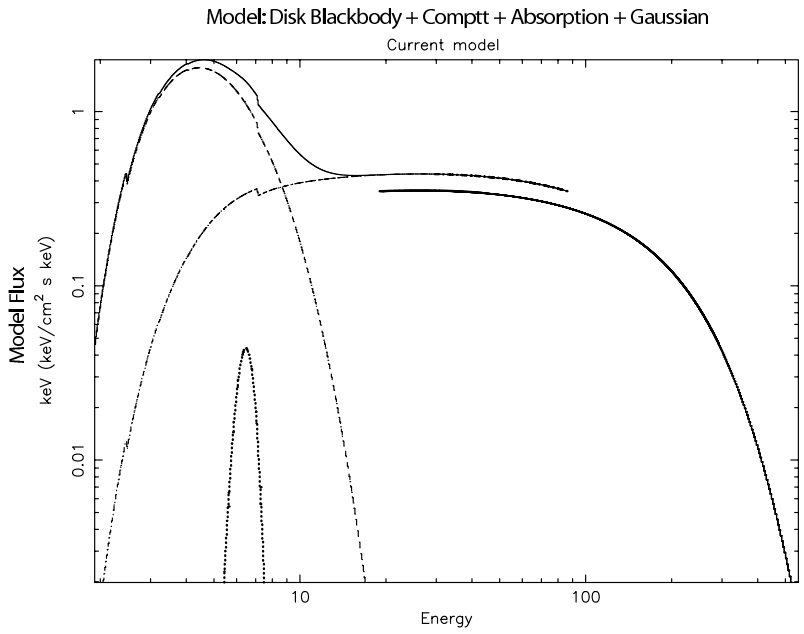

Figure 5.5 The contribution to overall flux by the individual model components of observation 40418-01-09-00.

Figure 5.5 shows the contributions of the various components of this spectral model (without *pexriv*). The different components are clearly seen, with the blackbody emission dominating the lower portion of the spectrum, and the Comptonization dominating out to $\sim$ 250 keV. The iron line contribution can also be seen. Figure 5.5 shows the spectrum as predicted from the model. The discontinuity at the overlap between the HEXTE and PCA model components is an artifact in allowing floating normalization between the two instruments. Figure 5.6 shows a fit of this model to the RXTE data, after running the model through the detector response matrices.

Towards the end of the outburst, the source was in the LS, as expected. During this state, the blackbody component contributes little to the X-ray spectrum. The spectrum can be fit equally well with a powerlaw spectral model describing the emission coming from the hot corona. Figures 5.7 and 5.8 show the RXTE data fit with a simple power law spectrum, and the assumed source spectrum of this model. The iron line and absorption were still included in these models.

The different states of this outburst are clearly shown in Figure 5.9. This figure

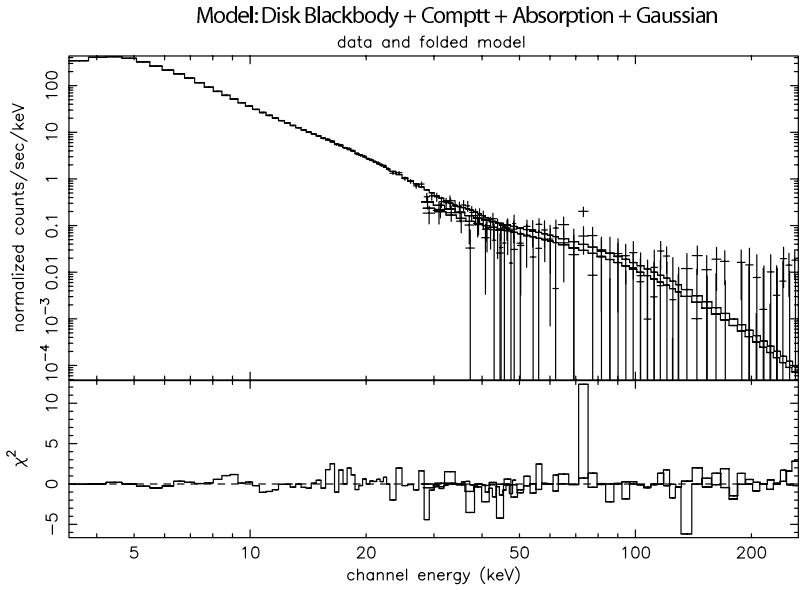

Figure 5.6 An example of a good fit of the model Wabs(DiskBB + CompTT + Gaussian) to RXTE PCA and HEXTE data. This is observation 40418-01-09-00, occurring towards the peak of the 1999 outburst. Soft X-ray data are PCA, two hard X-ray datasets are from the two HEXTE clusters.

shows how the outburst progresses through each state starting with the HS then transitioning into the LS and finally the very dim quiescent state. Figure 5.9 shows the different states color-coded to demonstrate where these states appear during the outburst and to show where they appear on a plot of the hardness (HEXTE rate / PCA rate) vs. the intensity (HID diagram).

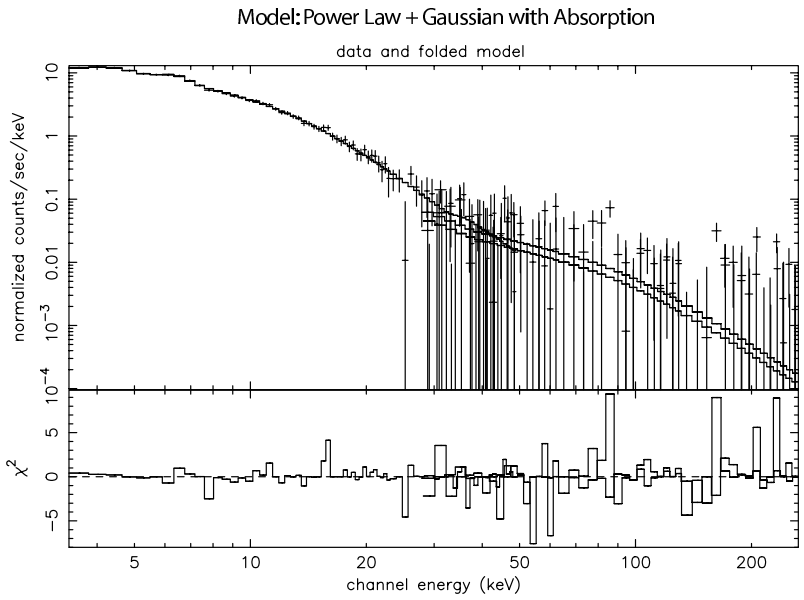

Figure 5.7 An example of a good fit of the model Wabs(Powerlaw + Gaussian) to RXTE PCA and HEXTE data. This is observation 40418-01-42-00, occurring in the tail after the outburst has levelled off. Soft X-ray data is PCA, two hard X-ray datasets are from the two HEXTE clusters.

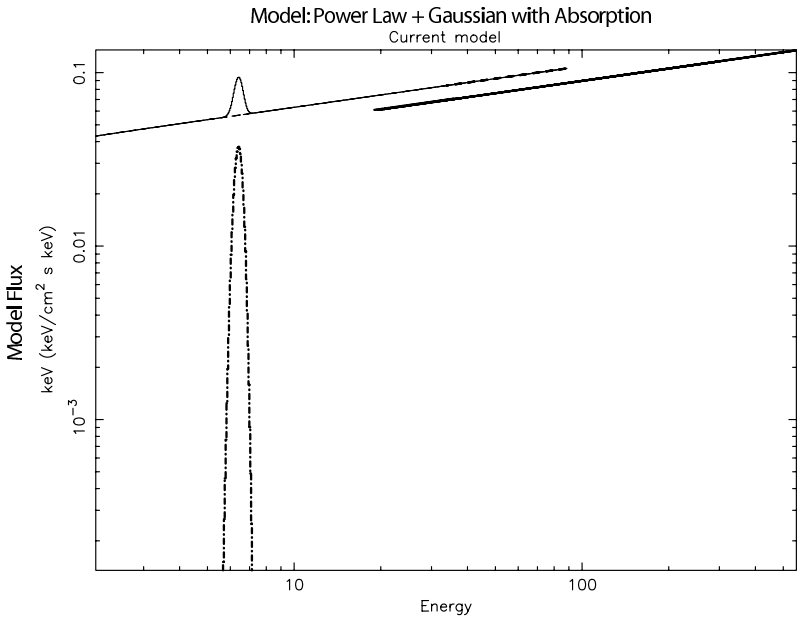

Figure 5.8 The contribution to overall flux by the individual model components of observation 40418-01-42-00.

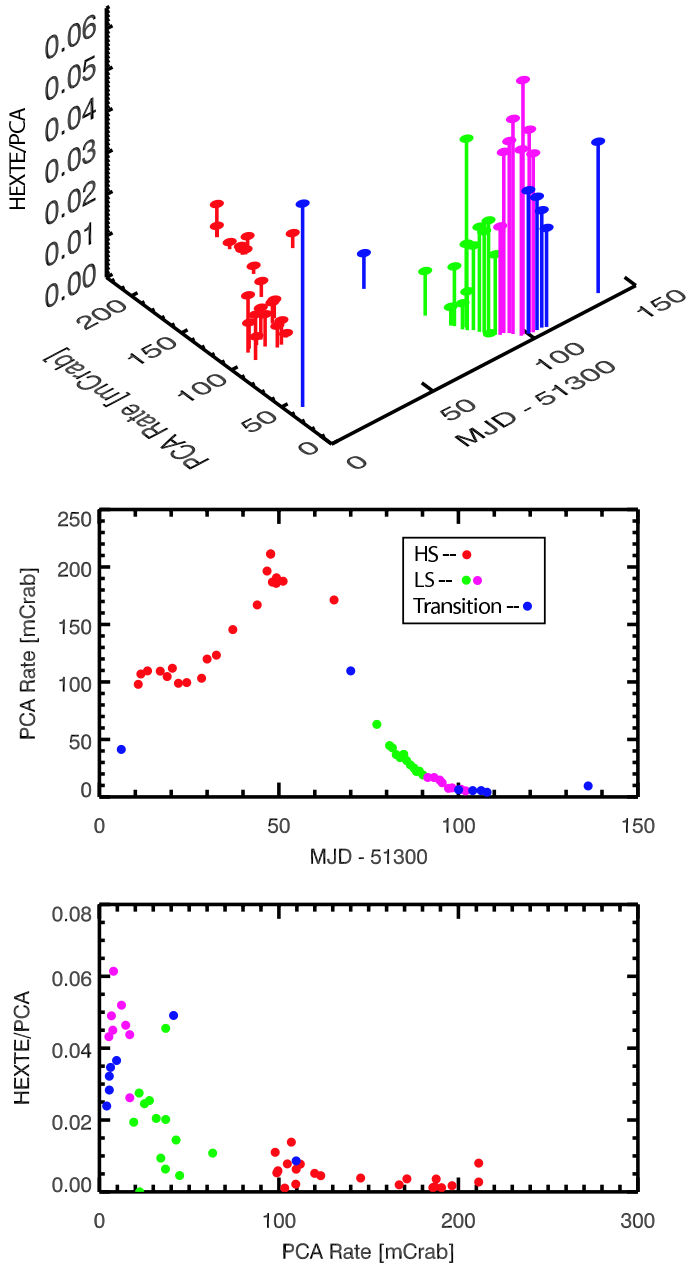

Figure 5.9 These three plots show different representations of RXTE data for the 1999 outburst. The top pane shows how the hardness (HEXTE rate/PCA rate) varies with intensity and time throughout the outburst. There are at least three fairly well defined regions in this plot. The **red** represents the HS, the **green** represents the LS, and the **purple** represent a harder subdivision of the LS. The **blue** points represent transition points, either between HS↔LS or between the LS and the quiescent state. The middle pane shows the PCA light curve of the outburst and where the different states come into play. The bottom pane shows the hardness vs. intensity (HID), this plot is often used to distinguish the states of the source. The conversion to units of the Crab Nebula from PCA counts is ~ 2600 ct s^{-1} per PCU.

From the spectral analysis we were able to calculate some parameters for the 4U 1630−472 system during the outburst. From the *diskbb* model we obtained the temperature of the inner edge of the accretion disk. Figure 5.10 shows how this temperature starts out high ≈ 1.2 keV (top middle pane) and then fluctuates slightly between 1–1.2 keV then rapidly drops off to $\lesssim 0.6$ keV as the source dramatically changed to the low-hard state. Figure 5.10 also shows the hardness ratio during the outburst (bottom middle pane). The hardness ratio clearly shows that the source is softer during the high-soft state then quickly gets hard when the source switches to the low-hard state before going into quiescence. The bottom pane in Figure 5.10 shows the light curve during the outburst.

In addition to the disk temperature, the radius of the inner edge of the accretion disk can be calculated from the *diskbb* model. From the *diskbb* normalization, the radius of the inner edge is calculated by $R = D\sqrt{k/\cos\theta}$, where R is the radius in km, D is the distance to the source[2] in units of 10 kpc, k is the *diskbb* normalization, and θ is the inclination of the accretion disk[3]. Figure 5.10 shows that the inner edge begins very close to the compact object and then recedes as the source changes from the HS to the LS (top pane). The main focus of the radius plot in Figure 5.10 is to show that the inner edge moves out at the beginning of the HS, and stays nearly constant until it recedes in the LS.

This is similar to behavior observed in outbursts of GS 1124–68, GRO J1655–40, and GS 2000+25. In each of these sources the best-fit inferred inner disk radius stayed nearly constant during the peak of the outburst. This is different than the 1998 outburst of 4U 1630−47, where the inferred radius changed throughout the outburst (Oosterbroek et al. 1998). The theoretical model for a standard Shakura-Sunyaev disk would have $T \propto r^{-3/4}$ where T is the disk temperature and r is the radius (strictly speaking only valid for radii much larger than $R_{\rm ISCO}$). This is described by assuming a constant mass accretion rate through the disk, $\dot{M} = 8\pi r^3 \sigma T^4/3GM$. Therefore, if the mass accretion rate is fairly constant, one would expect the temperature profile to vary as $r^{-3/4}$ as you move along the disk. It is interesting to point

[2]4U 1630−47 is estimated to be near the galactic center at a distance of ~ 10 kpc.
[3]Inclination here and in *pexriv* is assumed to be 75° (Kuulkers et al. 1998).

out that this is qualitatively what Oosterbroek et al. (1998) measured during the 1998 outburst. We observe that there is not a single-valued function that describes this relationship during the 1999 outburst (see Figure 5.11). Figure 5.11 shows the measured values for the inner edge temperature plotted against the inferred inner edge radius. Also plotted is the theoretical curve showing the $T \propto r^{-3/4}$ relationship that would be expected for a constant mass accretion rate. This observation provides evidence that the mass accretion rate is not constant during the 1999 outburst even though it may have been during the 1998 outburst. This could be a clue in explaining the differences in the light curves between the 1996, 1999 outbursts and the 1998, 2001 outbursts as discussed in §5.2.5.

Timing Analysis

Timing analysis was performed on both the RXTE PCA data and the USA data. The USA data were filtered based on the cuts described in §4.3.2. The filtered data were then analyzed using *SPECAN*, a power spectral density program designed by Dr. Warren Focke to create PSD from USA event data performing dead time corrections as described in Shabad (2000). We created Poisson noise subtracted, dead time corrected, RMS normalized[4] power spectra from 0.0156 – 256 Hz. The power spectra were each visually inspected for evidence of quasi-periodic oscillations (QPOs). In one RXTE observation, one QPO was detected with centroid, FWHM, and RMS of 0.84 Hz, 0.98 Hz, 13.3% respectively. QPOs have been detected in this source during the 1998 outburst (Tomsick & Kaaret 2000). This is the first reporting of a QPO during the 1999 outburst. The QPO is present for only one RXTE observation at the very beginning of the outburst. This QPO is shown in Figure 5.12. The fit to the power spectrum includes a broken power law with the index of the first leg being fixed to zero. The position of the break, and the second index are allowed to float.

[4]RMS normalized means the units of the power spectrum will be fractional RMS power per Hz.

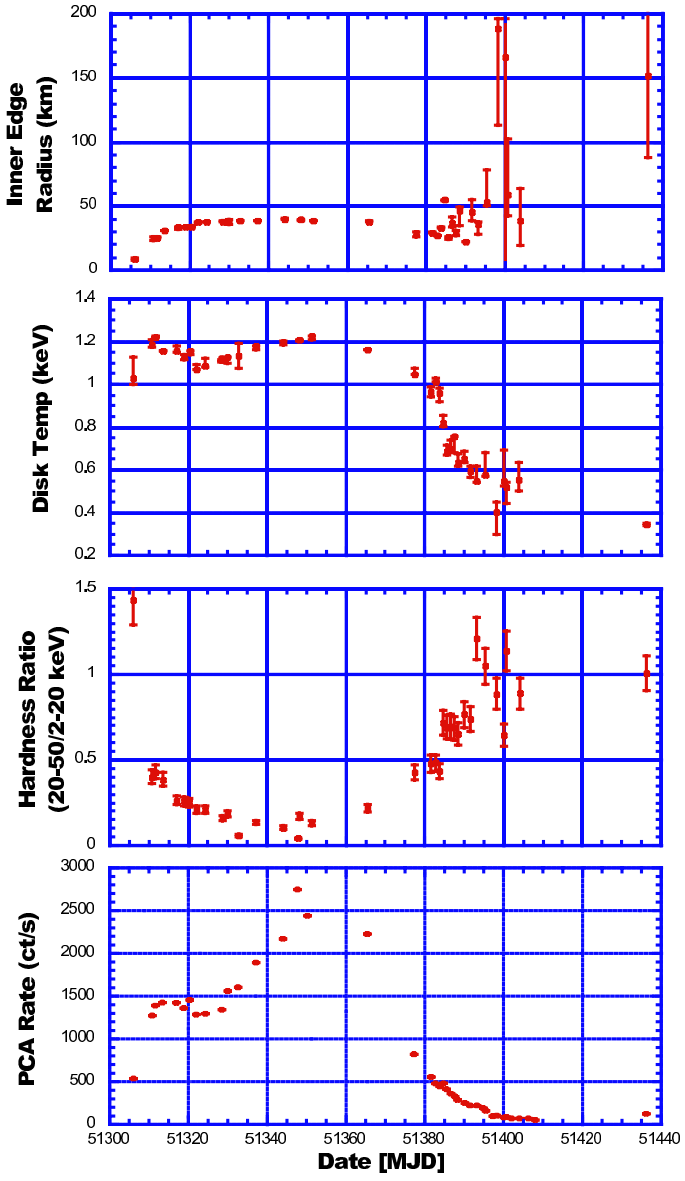

Figure 5.10 Plot showing the evolution of the inner edge of the accretion disk inferred radius (top pane), disk temperature (top middle pane) and hardness ratio (bottom middle pane) during the 1999 outburst (bottom pane). The hardness ratio is based on the calculated model flux from the source using the ranges 20–50 keV over 2.5–20 keV.

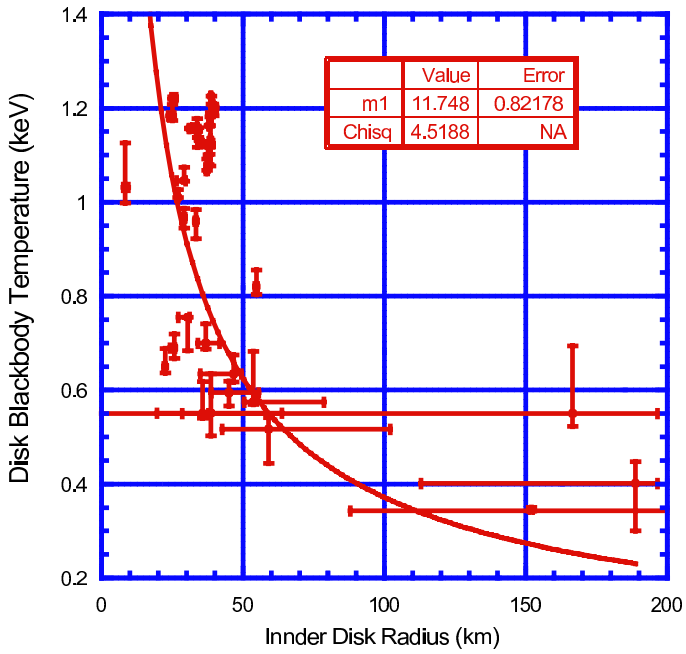

Figure 5.11 The relation between the inner disk temperature and the best fit inner disk radius. The inner disk radii were obtained assuming a distance of 10 kpc and $\theta = 75°$. The line represents the theoretical relationship $T \propto r^{-3/4}$ that would be expected for a constant mass accretion rate.

The relevent broken power law equation is:

$$\text{if} x \leq P_2 \quad \text{Power} = \quad P_3 e^{\left(P_0 \ln \frac{\text{Freq}}{P_2}\right)} \tag{5.2}$$

$$\text{if} x \geq P_2 \quad \text{Power} = \quad P_3 e^{\left(P_1 \ln \frac{\text{Freq}}{P_2}\right)} \tag{5.3}$$

where P_0 is the index at low frequency, P_1 is the index at high frequency, P_2 is the break frequency, and P_3 is the power at the break. For the QPO, a Lorentzian was added to the broken power law fit. The power from a Lorentzian power distribution is:

$$\text{Power} = P_4 / \left(\left(\frac{\text{Freq} - P_5}{P_6} \right)^2 + 1 \right) \tag{5.4}$$

where P_4 is the height of the QPO, P_5 is the QPO centroid frequency, and P_6 is the QPO HWHM.

The fractional RMS variability for each USA observation was calculated for the range 0.0156–256 Hz. The results are shown in Figure 5.13. The RMS variability during the LS is seen to be anti-correlated with the intensity. The RMS variability during the LS is also higher than the variability during the HS. The variability in the hard state is believed to be coming from random emissions of radiation from the optically thin hot corona. The shape and details of this corona are not known. The emission in the HS is from a relatively uniform thermal disk. The variability in this configuration should be much smaller as the emission will be less discrete and more distributed over the surface of the disk. The increase in the variability during the LS gives evidence to support that the corona is not a uniform plasma distributed evenly around the disk, but perhaps more localized in it's distribution. There is some evidence for correlation between flux and RMS variability in the HS state, however, the statistics limit us from making a definitive statement about this.

5.2.5 Discussion

Since the discovery of 4U 1630−47, quasi-periodic outbursts have been observed in this source every 450–700 days (Kuulkers et al. 1997). The 1999 outburst occurred significantly earlier than predicted, with $\sim$ 700 days between the onset of the 1996 and 1998 outburst and only $\sim$ 450 days between the onset of the 1998 and 1999 outburst, and again $\sim$ 550 days between the 1999 and 2001 outburst, with $\sim$ 700 days between the 2001 and 2002 outburst. Since the outburst recurrence is not well defined it is unlikely that the outbursts have anything to do with the binary orbit of the system.

From Figure 5.3, one sees an interesting relationship. The 1996 and 1999 outbursts have similar shapes to their light curves. Both have a double peaked structure with a broad plateau connecting them. In both outbursts the initial peak is slightly lower than the second peak. However, the 1998 and 2001 outbursts show similarities in *their* light curves. Both show twin peaked structures with the second peak 3–4 times higher than the first peak, with no plateau between the two. 4U 1630−47 is

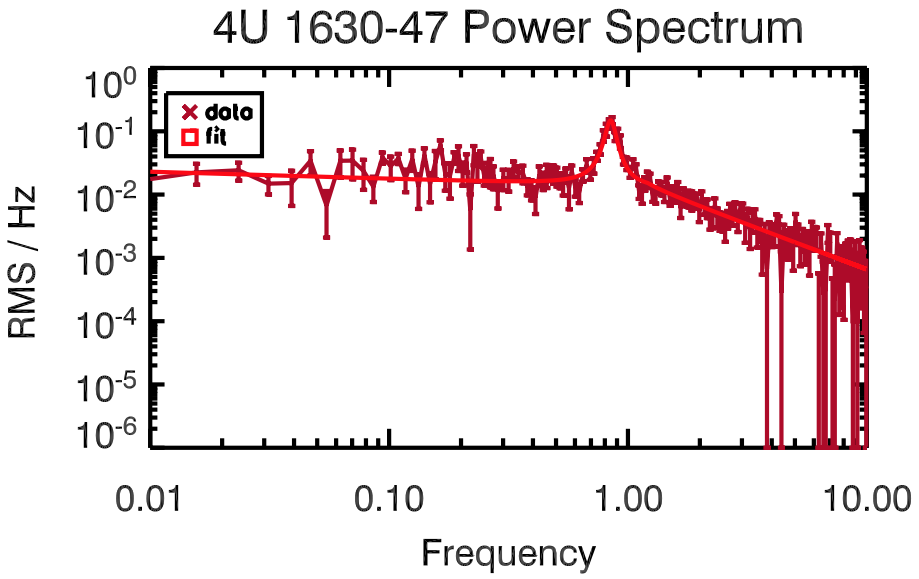

Figure 5.12 QPO found during the onset of the 1999 outburst. The QPO is only detected in RXTE observation 40418-01-01-00. The fit shown is a broken powerlaw with a Lorentzian to describe the QPO.

in outburst currently, and the light curve of the current outburst is brighter than even the bright 2001 outburst, but it is still too early to compare the shape of the outburst to see if it continues the pattern and matches the 1996 and 1999 outbursts. The e-folding time of 13.8 days is similar to those found in 1996 (14.9 days), 1998 (14.4 days), and 2001 (14.8 days for the decay of the second peak). This may suggest that the e-folding time is related to a physical property of the the system that does not change between outbursts (Tomsick & Kaaret 2000). The e-folding time may be related to the mass of the compact object (Cannizzo, Chen, & Livio 1995), or the radius of the accretion disk (King & Ritter 1998). Note that outbursts measured in the 1970's–1980's were recorded with e-folding times of $\sim$ 50 days (Parmar, Stella, & White 1986). In these cases, it is likely the double peak was misinterpreted as a single long peak in these observations.

Spectral differences separate the 1998 and 1999 outbursts also. The 1998 outburst

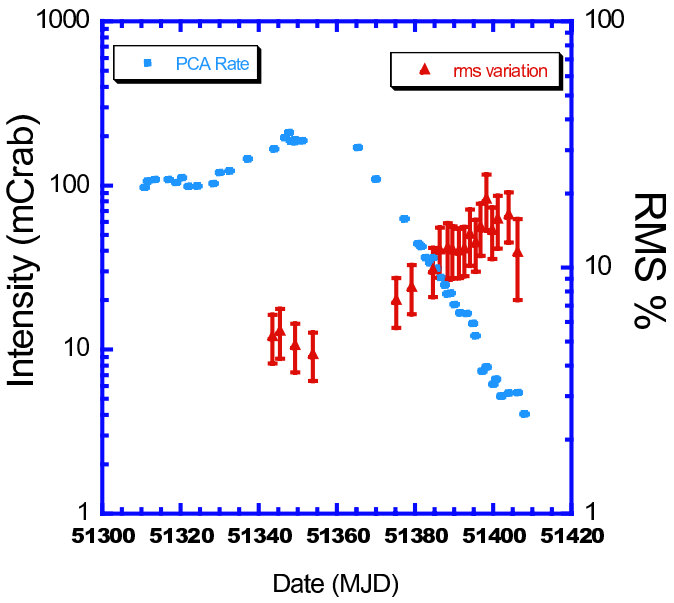

Figure 5.13 The RMS in percent of the power density spectra of the 1999 outburst calculated from USA data (0.156–256 Hz). The light curve of the outburst, measured by the PCA $\sim 2-50$ keV, is also plotted. One can see that during the LS the RMS is *anti-correlated* with the intensity.

clearly became softer throughout the outburst (Trudolyubov, Borozdin, & Priedhorsky 2001) whereas the 1999 outburst did not. There is also evidence that the mass accretion rate changed during the 1999 outburst, where other authors have given evidence that this may not have been the case during the 1998 outburst as described in §5.2.4. A very hard state dominated by a power law was also detected during the peak of the 1998 outburst (Trudolyubov, Borozdin, & Priedhorsky 2001). No such state was detected during the peak of the 1999 outburst. The source stayed in a high-soft state during the entire peak of the outburst. The 1999 outburst follows a well-defined hard to soft back to hard transition, as was the case during the 1996 outburst.

5.2.6 Conclusions

We have analyzed 47 RXTE and 101 USA observations during the 1999 outburst of 4U 1630−47. We found that the source underwent a transition to the high-soft state and made an abrupt transition to the low-hard state after spending several days in a plateau. We found that the 1999 outburst was similar in its energy spectrum and light curve to the 1996 outburst. We detected a low frequency QPO in one RXTE observation of the source during the initial rise of the outburst.

We found that in the hard state the hardness and intensity are anti-correlated. This is understood because the hard emission comes from the hot corona, and an increase in relatively cool seed photon flux will have the tendency to cool the corona. In the soft state we would expect the opposite. The flux is due to the thermal emission from the inner edge of the accretion disk. As it heats up, it increases in intensity and in temperature, thereby getting harder. We were not able to verify this in our data. The hardness ratios were too scattered and the high state was too stable to see a trend.

We found that the RMS variability is anti-correlated with the intensity in the hard state. We also find the RMS variability in the LS to be much higher than in the HS. This is attributed to the origin of the emission in the HS originating near a smooth hot accretion disk edge, and emission in the LS is coming from non-thermal processes occurring in the corona surrounding the compact object and disk.

Chapter 6

Conclusions and Perspectives

6.1 Summary

6.1.1 Type I X-ray Burst Summary

In chapter 4, we presented an analysis of type I X-ray bursts. This short timescale non-quiescent behavior found in neutron stars is the result of rapid thermonuclear burning. We concluded, from the USA data archive, that the bursting rate in neutron stars is $\lambda_{NS} = 1.7 \pm 0.4 \times 10^{-5}$ bursts s^{-1}. Using data from both USA and RXTE we calculate an upper limit on the bursting rate in BHCs to be $\lambda_{BHC} \leq 4.9 \times 10^{-7}$ bursts s^{-1}. We used the theoretical interpretation of Narayan & Heyl (2002) to calculate regions of luminosity where the neutron stars are expected to burst and the BHCs would be expected to burst if they had a similar surface. In this luminosity region 464 ks of neutron star data yield an averaged mean burst rate of $4.1 \pm 0.9 \times 10^{-5}$ bursts s^{-1}, and 1512 ks of BHC data yield a 95% confidence level upper limit of 2.0×10^{-6} bursts s^{-1} and a strong limit that BHCs do not burst with a rate similar to the rate of neutron stars in these regions. This gives evidence that BHCs do not have surfaces. This only applies to surfaces as described in Narayan & Heyl (2002), that have ordinary nuclear states of matter at the surface. Narayan & Heyl defend this assumption by showing that the pressures and temperatures they calculate for a theoretical surface are not outside the range of normal matter. However, other authors have speculated

that other states of matter may exist here, see §4.3.3.

We conclude chapter 4 with a brief analysis of the timing and spectral properties of the type I X-ray bursts detected in the USA data archive. The timing analysis consisted of searching the PSD of each burst in 0.5 s intervals for evidence of oscillations that would show the presence of burst oscillations that have been interpreted as modulations from the surface of a neutron star due to the star's rotation. Each 0.5 s segment of each burst was also fit with a blackbody spectrum to catalog the temperature and flux as the burst progressed. This opens up a method that can be used to calculate the radius and mass of the neutron star once a distance and spectral hardening factor are calculated. We encourage this study to be performed on the USA X-ray burst data.

6.1.2 4U 1630−47 Outburst Summary

From spectral analysis of RXTE data we found that 4U 1630−47 underwent a transition from quiescence to LS to HS then an abrupt transition to the LS then back to quiescence. Our data showed that the source had an anti-correlation of intensity to hardness in the LS. We calculated that the inner-disk radius moves very close to the compact object in the HS and very quickly moves away during the sharp LS transition. Analyzing the disk temperature and radius show that the accretion rate changed during the 1999 outburst, which was not believed to be the case during the 1998 outburst.

From timing analysis of RXTE and USA data, we found one ~ 1 Hz QPO at the initial rise of the outburst. No other QPOs, and no X-ray dips were observed during the 1999 outburst. We see a dramatic rise in the RMS variability in the source as it goes into and throughout the LS. The RMS variability is anti-correlated with the intensity in the LS.

Comparing the 1999 4U 1630−47 outburst to other outbursts in this source, we detect a pattern that consists of two outbursts per cycle. The 1996 and 1999 outburst have similar light curve shapes and had similar spectral properties. Whereas, the 1998 and 2001 outburst have similar shapes, and the 1998 outburst had distinct spectral

differences during the outburst as compared to the 1999 outburst. However, RXTE era outbursts have similar *e*-folding times as the outburst wanes, all $\sim$ 14 days. In contrast, outbursts measured with the EXOSAT satellite recorded *e*-folding times of $\sim$ 50 days (however, this may not have correctly interpreted the twin peaked profile). The outbursts do not seem to be triggered by orbital modulations, as the period between outbursts is variable, between 450–700 days. The source is currently in outburst, and it is too early to tell if the outburst is going to follow the previous pattern. At this time, it appears to be much brighter than any previous outburst, but the shape cannot be determined. This source is an interesting link between persistent sources and transient sources as its outbursts are frequent and it shows similar spectral properties to both types of sources. This source should be studied in more detail to determine the companion type, and to estimate the mass to try to understand this system more fully.

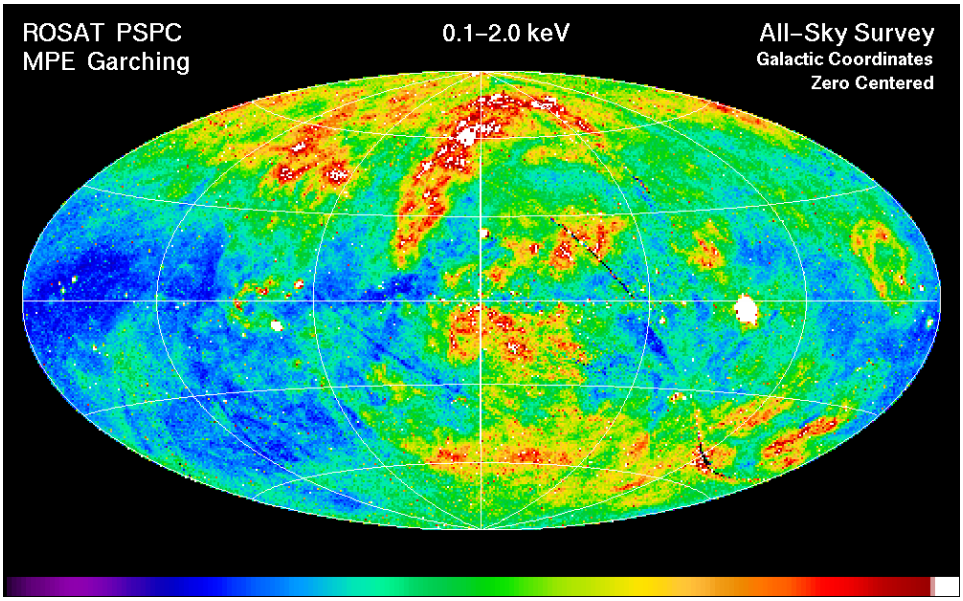

Figure 6.1 The entire X-ray sky in the 0.1–2.0 keV energy band as observed with the position sensitive proportional counters (PSPC) during the All-Sky Survey performed during the first 1/2 year (1990–91) of the ROSAT Mission.

6.2 Future Developments

6.2.1 X-ray Astrophysics

We are protected from X-rays on Earth by the Earth's atmosphere. Unfortunately, this also means that we must design and launch space-based missions to study the X-ray universe. Figure 6.1 shows the X-ray sky as seen by the satellite observatory ROSAT. RXTE will continue to collect precision timing data for some time to come until the PCA eventually runs out of gas. The future of X-ray astronomy is rapidly forming into precise spectral and imaging capabilities. This future was ushered in with the launch of the Chandra X-ray observatory in 1999 July, the XMM-Newton observatory in 1999 December, and INTEGRAL in 2002 October. Planned observatories include Astro-E2, and Constellation X. A general overview of the capabilites of each of these experiments is outlined in this section to give the reader an idea of the possibilities for the future of X-ray astronomy.

Chandra X-ray Observatory

The combination of high resolution, large collecting area, and sensitivity to high-energy X-rays make Chandra able to study faint sources, in crowded fields, even if highly absorbed. Chandra is in an elliptical, high-Earth, 48 hour period, orbit allowing long uninterrupted observations. Chandra is very strong in X-ray imaging and good in spectroscopy. Chandra is the X-ray "Hubble" with $\sim 0.5''$ point spread function.

Chandra has a single grazing incidence imagine telescope with a FOV $\sim 30'$ circular, and effective area of 800 and 400 cm^2 at 0.25 and 5 keV respectively. Four detectors can be placed individually in the telescope. Two detectors are imaging & spectral and two are grating instruments for high resolution spectroscopy. Therefore, Chandra can be used to both image and perform detailed spectroscopy on X-ray targets. Chandra can also perform timing analysis with a resolution of $\sim$3 ms. Details of the Chandra mission and calibration can be found in R.N.Ogley (1998). Chandra is expected to have a lifetime of at least 5 years.

X-ray Multi-mirror Mission (XMM-Newton)

XMM-Newton is a European Space Agency X-ray telescope with an optical monitor that was launched 1999 December. XMM-Newton has three grazing incidence telescopes with two X-ray imaging cameras sensitive in the 0.1–15 keV range, with effective areas of 922 and 1227 cm^2 at 1 keV. The spatial resolution of the telescopes is 6 arcseconds. The third detector is a reflection grating spectrometer, 0.35–2.5 keV E/dE 200–800, with effective area of 185 cm^2 at 1 keV. The optical monitor is sensitive in the 180–650 nm band with a 17 arcmin FOV and resolution of $\sim$ one arcsec. XMM-Newton is very strong in X-ray spectroscopy and good in imaging.

XMM-Newton can perform imaging of X-ray sources, X-ray spectroscopy, and X-ray photometry timing with an accuracy of 30 μs. Details of the XMM-Newton mission and calibration can be found in Lumb et al. (2003) and references therein. XMM-Newton is planned to have a nominal 10 year mission.

International Gamma-Ray Astrophysics Laboratory (INTEGRAL)

INTEGRAL was launched 2002 October. INTEGRAL has four main instruments: an imager (IBIS), a spectrometer (SPI), an X-ray monitor (JEM-X), and an optical monitoring camera (OMC). The IBIS will image in the range 15 keV – 10 MeV with a spatial resolution of 12 arcmin. The SPI is effective in the 20 keV – 8 MeV energy range with a resolution of $E/dE = 500$. The JEM-X is a coded mask proportional counter. JEM-X is sensitive in the 3–35 keV band with 1000 cm^2 effective area. JEM-X has an energy resolution of 1.2 keV at 10 keV and an angular resolution of 3 arcmin, and a timing accuracy of $\sim$ 120 μs. The OMC will observe the optical emission (500–600 nm) from the prime targets of the two INTEGRAL Gamma-ray instruments. Details of the INTEGRAL mission can be found in Parmar et al. (2003) and references therein. The INTEGRAL mission is designed for a lifetime of 5 years.

Astro-E2

The Astro-E2 mission will be an improved version of the Astro-E mission that was lost during launch in 2000 February. Astro-E2 is a joint effort between NASA and the Japanese ISAS to be launched 2005 February. Astro-E2 will have five foil telescopes with three main detectors. First, the X-ray spectrometer (XRS) is a system of cryogenic bolometers that will cover the energy range of 0.4–10 keV with a resolution of $\sim$ 10 eV, with an effective area of about 150 cm^2. Second, there are four X-ray imaging spectrometers (XIS) which cover 0.4–12 keV, with 120 eV resolution. The XIS has an effective area of about 300 cm^2 and can image with a spatial resolution of 1.5 arcmin. Third, the hard X-ray detector (HXD) is a non-imaging detector sensitive in the 10–700 keV range, with a very low background. The HXD has an effective area of about 300 cm^2 and energy resolution of about 30% at 10 keV and 9% at 662 keV. Details of the Astro-E2 instrument can be found in Stahle et al. (1999) for the XRS, Dotani et al. (2003) for the XIS, and Tanihata et al. (1999) for the HXD.

Constellation-X

Constellation-X is going to be a revolutionary way to perform X-ray astronomy and spaced based astronomy as a whole. Constellation-X will consist of four coordinated independent satellites that will form a very large X-ray telescope. The minimum effective area of this telescope will be 1,000 cm^2 from 0.25–10 keV, 15,000 cm^2 at 1.25 keV, 6,000 cm^2 at 6.0 keV, 1,500 cm^2 from 10–40 keV. The minimum spatial resolution will be 15 arcsec from 0.25–10 keV, 1 arcmin from 10–40 keV. The spectral resolving power (E/dE) will be > 300 from 0.25–6.0 keV, 1,500 from 6.0–10 keV, $>$ 10 from 10–40 keV. The timing resolution of Constellation-X will be ~ 100 μs. For details on the Constellation-X design see White & Tananbaum (2003). Constellation-X is not scheduled to launch until after 2010.

X-ray Polarization Experiments

Polarimetry of X-rays and gamma-rays is one of the last unexplored realms in astrophysics. Gamma-ray bursts (GRBs) are one of the areas of increased interest for X-ray polarimetry. Hard X-ray polarization measurements of the flash phase of the GRB will allow us to probe the geometry of the emission at earlier times. There are basically three types of X-ray polarimeters being developed. Detectors based on scattering X-rays with a crystal (e.g., McConnell et al. 2003), detectors based on Compton scattering in silicon (e.g., Kotthaus et al. 1999), and detectors based on micro-strip gas chambers (MSGC) (e.g., Bellazzini et al. 2003). There are several planned and developing instruments that are being designed to open this area of research in the near future.

6.2.2 Gamma Ray Astrophysics with GLAST

The GLAST mission will greatly increase the data in the 20 MeV–300 GeV energy range. GLAST will have an imaging capability in this range much better than any previous mission. The main focus of GLAST will be extragalactic sources, and the diffuse galactic and extragalactic background, with secondary focus on aspects of galactic sources. The primary focus of the physics in this thesis involve processes

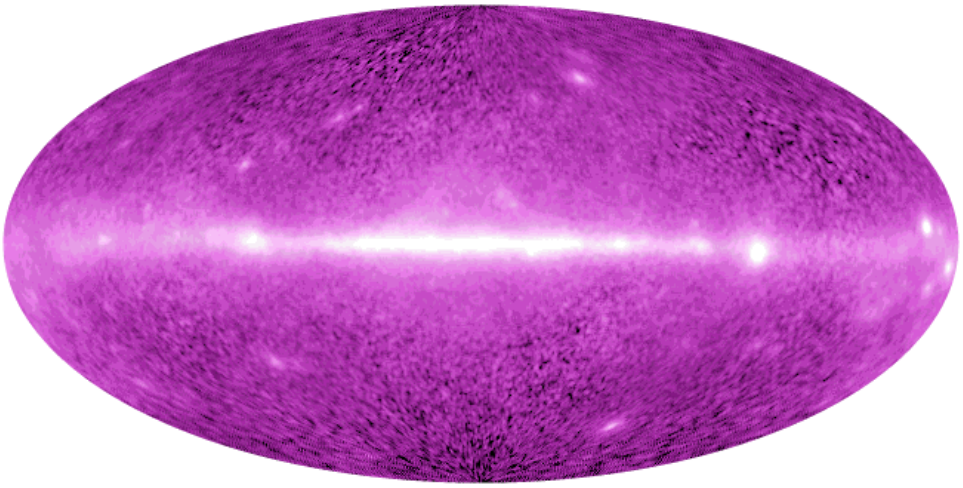

Figure 6.2 EGRET all-sky map in Galactic coordinates for energies > 100 MeV. The broad central band across the center of the image is diffuse emission from cosmic-ray interactions in the Milky Way. The brightest sources close to the plane are gamma-ray pulsars. The bright sources away from the plane are active galactic nuclei or unidentified.

occurring within galactic binaries. However, the physics processes to be studied by GLAST are strongly related, as the largest black holes formed in active galactic nuclei (AGNs) are powered by accretion similar to the way the stellar black holes and neutron stars are powered in our own galaxy. As with X-rays, all but the highest energy gamma-ray universe is blocked from ground observation by the Earth's atmosphere. Therefore, GLAST must be a satellite based instrument to explore these energies. GLAST was designed to build on discoveries made by the Energetic Gamma-Ray Experiment Telescope (EGRET) which operated from 1991–2000. Figure 6.2 shows the gamma-ray sky as seen by EGRET. In this section, an outline of the astrophysics goals that will be tackled with GLAST are discussed.

Active Galactic Nuclei

GLAST will study details of the AGNs, esp. the blazar-class AGNs. Blazars show intense, flat-spectrum radio-loud emission, with a relativistic jet pointed nearly straight toward us. The bulk of the luminosity for many blazars is emitted in the GLAST

energy range. This emission is believed to be powered by accretion onto a supermassive black hole ($\sim 10^7 - 10^9$ $M_\odot$) at the core of a distant galaxy (see e.g., Blandford & Rees 1978). GLAST observations of the inner regions of jets in these sources will advance studies of the jet-disk relationship. This is especially topical when comparing to the galactic microquasars such as GRO J1655−40, 1E 1740−2942, GRS 1758−258, and GRS 1915+105 which was searched for bursts in §4. Microquasars are galactic X-ray binaries which eject relativistic jets. Microquasars behave like AGNs, but on a smaller scale. These sources are an important link to tie binary studies by X-ray experiments to studies to be performed with GLAST.

GLAST observations will allow new tests to explain the beaming phenomena in jets. Studies based on the correlated emissions of the synchrotron X-ray and Compton gamma-ray components of blazars using GLAST in coordination with XMM, Chandra, Astro-E II and Integral X-ray experiments will provide accurate measurements of the bulk Lorentz factors in the jets (Catanese et al. 1997). GLAST will probe the physics within these relativistic jets with time resolved energy and power spectra at an accuracy not possible before.

GLAST will detect many more blazars than EGRET, possibly detecting them back to the time of their formation. These studies will be used to compare the evolution of blazars with radio quasars and star formation history.

Cosmology and the Diffuse Background

EGRET confirmed the presence of an isotropic extragalactic gamma-ray background that is well described by a power law with photon spectral index $\alpha = 2.10 \pm 0.03$ over EGRET's range of 20 MeV–30 GeV. This diffuse emission could be from unresolved blazars throughout the sky, or it could be from particle physics interactions. The diffuse emission could be relic radiation from some unknown high-energy process in the early Universe, such as neutralino decay, which would violate some versions of supersymmetric extensions of the standard model of particle physics (SUSY). GLAST could also be in a position to detect Kaluza-Klein graviton decays. This detection would give evidence that could be used to limit the size of extra dimensions implied by particle physics (Hannestad & Raffelt 2002). GLAST will be able to resolve

more point sources than EGRET, testing this hypothesis on the origin of the diffuse isotropic emission. In addition, detailed spectra should be able to resolve between AGN emission and emission from relic radiation.

Unidentified Sources

More than 60% of the gamma-ray sources are unidentified. GLAST will provide the sensitivity and angular resolution to correlate the gamma-ray emission to known sources at longer wavelengths. GLAST may find these unknown sources to be undiscovered blazars, undiscovered gamma-ray pulsars, X-ray binaries that also produce gamma-ray emissions, or belonging to a new source class.

Gamma-Ray Pulsars

High-energy gamma rays represent the bulk of energy output from many pulsars. Pulsars also make up the brightest persistent sources in the gamma-ray sky. There are two competing methods for gamma-ray emission from pulsars. The outer gap model (e.g. Romani 1996) with the gamma rays being produced at high altitudes allows viewing of the gamma-ray at large angles to the spin axis. And, the polar cap model (e.g. Harding 1981) with emission occurring closer to the neutron star surface. GLAST will test these two models by providing high quality phase resolved spectra.

Dark Matter Annihilation

Measured rotation curves of galaxies, and gas confinement in galaxy clusters provide evidence for the existence of dark matter, see Ashman (1992) and Trimble (1987) for reviews on evidence for dark matter. A promising candidate for dark matter is the lightest supersymmetric particle, χ, the neutralino. Current limits place the mass of the neutralino between 30 GeV $< M_\chi <$ 10 TeV. This is outside the realm of current particle accelerators, but if neutralinos exist at these energies and annihilate, the signature of annihilation would be detectable in the galactic diffuse energy spectrum measured by GLAST. The neutralino signal in its various guises is discussed in detail in Ullio et al. (2002).

Gamma-Ray Bursts (GRBs)

GLAST is composed of the LAT and the GBM described in §3.3. The LAT in conjunction with the GBM will measure the energy spectra of GRBs from 10 keV to hundreds of GeV during the short time after the GRB onset when the vast majority of energy is released. GLAST will also promptly alert other observers to the GRB and measure the gamma-ray afterglow. Most GRBs release over 100 times more energy than a supernova, $\sim 10^{51-54}$ ergs. Current models for the GRB engine include hypernova (Paczynski 1998), collapsars, and neutron star/black hole or neutron star/neutron star binary mergers (Janka et al. 1999).

EGRET detected ~ 30 GRBs, simulations show that GLAST may detect ~ 200 GRBs per year. GLAST will also detect many more photons per GRB, and not be deadtime limited as EGRET was for bright outbursts. In addition, the LAT and GBM will measure the spectra from X-rays through gamma rays.

Cosmic Rays and Interstellar Emission

Cosmic rays (CRs) are relativistic charged particles from space. GLAST will have the potential to detect cosmic ray production sites, believed to be supernova remnants (SNRs). GLAST will also study the diffuse gamma-ray emission from the interaction of CRs with interstellar gas and photons. GLAST will be able to resolve the gamma-ray emission of SNRs. This will help to distinguish the emission from the shell of the SNR or a compact source. The presence of a so called π^0 spectral bump in a SNR would also yield evidence that CRs are produced in SNRs. The π^0 bump occurs when the neutral pions decay after being produced in nuclear interactions between high energy nucleons (Hunter et al. 1997). GLAST will also be able to measure the shape of the CR spectra.

GLAST will also advance the study of the dense interstellar medium by looking at emission from clouds illuminated by CRs. Gamma-ray observations are useful for calibrating the relationship between CO and H_2.

Solar Flares

The processes that accelerate particles to GeV energies in the Sun are not well understood. GLAST will contribute by resolving where the acceleration takes place. For large flares, GLAST will be able to resolve whether the acceleration is extended or point-like. A π^0 bump at 68 MeV would give evidence of proton acceleration. A sharp break in the gamma-ray spectrum would be evidence for electric fields causing the acceleration. The GBM on GLAST will be able to track flares from X-ray to gamma-ray energies. The LAT will be able to detect much smaller flares than have been studied before.

Further Information

More information about the science capabilities of GLAST can be found in Gehrels & Michelson (1999), and at the NASA GLAST website http://glast.gsfc.nasa.gov/. Instrument details can be found in §3.3 and details on GLAST testing and construction are given in §B.1.

We have a habit in writing articles published in scientific journals to make the work as finished as possible, to cover up all the tracks, to not worry about the blind alleys or describe how you had the wrong idea first, and so on. So there isn't any place to publish, in a dignified manner, what you actually did in order to get to do the work.

– Richard Phillips Feynman (1918-1988)

Appendix A

Systems of Time Used in Astrophysics

Does anyone really know what time it is?
– Chicago Transit Authority (1969)

One of the oldest branches of astronomy has been time keeping and calendar construction. Until the advent of atomic clocks, there was no earthbound process of time keeping more accurate than time determinations from observations of the Sun, planets and stars. Even now, data suggests that millisecond pulsars are more accurate over long periods of time than the best atomic clocks.

Sidereal Time

One of the first methods to devise a system of time is based on the *sidereal day*. A *sidereal day*, to first order, is the time interval between two successive passes of the same star through the meridian of the celestial sphere. The duration of the *sidereal day* in units of *Universal Time* is 23 h 56 m 04.0905 s. *Sidereal Time* is based on the *hour angle*, which is the angle a great circle containing the celestial poles and a star makes when it cuts the meridian at celestial poles. *Solar Time* is based on the time it takes the Sun to cross this meridian, a *solar day*. However, since the Earth

also travels in its orbit during the course of one day, the *solar day* is 4 minutes longer than a *sidereal day*. In addition, the duration of the *solar day* varies with the seasons due to the eccentricity of the orbit and the tilt of the Earth's axis of rotation. In an effort to obtain a more even time scale, the *Mean Sun* was defined to take the same amount of time from vernal equinox to the next as the true Sun, but moves with constant velocity along the celestial equator in between. This defines the *mean solar day*.

Universal Time

The *Universal Time* was established in 1926 to replace Greenwich Mean Time (GMT). *Universal Time (UT)* is counted from zero hours at the Greenwich reference meridian, and has a duration of one *mean solar day*.

The *UT* is actually calculated from the more precisely measured *sidereal time* because we know the difference between the *sidereal day* and the *mean solar day*. *UT0* is the time calculated from the measured *sidereal time* to the Greenwich reference meridian.

The Earth does not rotate uniformly. The movement of the Earth's poles must be corrected for to get the correct time on all places on the Earth. After correcting *UT0* for these effects, one gets the time system *UT1*. The *Universal Time* commonly used in astronomy is *UT1*.

Atomic Time (TAI & UTC)

The second derived from *UT1* varies noticeably due to irregularities in the rotation of the Earth. Therefore, the SI second was defined as 9,192,631,770 cycles of radiation corresponding to the transition between two hyperfine levels of the ground state of ^{133}Cs. The weighted mean of many atomic clocks across the Earth is used to define *TAI* (Temps Atomique International). *TAI* is currently the best time system based on the SI second, accurate to $\pm 2 \times 10^{-14}$. *TAI* refers to a location at sea level rotating with the Earth. *Coordinated Universal Time (UTC)*, differs from *TAI* by an integral

number of seconds. *UTC* & *TAI* differ because *UTC* is required to be within ±0.9 s of *UT1*. This requires leap seconds to occasionally be inserted into or dropped from *UTC* (to date all leap seconds have been positive) twice a year as needed. *UTC* offers both a highly constant unit of time as well as agreement with the position of the Sun. Therefore, *UTC* is the basis for all civil timekeeping today.

Dynamical Time (TDT & TDB)

The rotation of the Earth is erratic, hence any timescale based in it will be erratic. Application of Newton's laws of motion require a smoothly flowing time variable. Therefore, *Dynamical Time* was defined as a timescale that could be used with the laws of motion to correctly predict the positions of celestial bodies, and is therefore used as the argument when calculating ephemerides. In 1977 the *Terrestrial Dynamical Time (TDT)* was defined such that a unit of duration is 86400 SI seconds on the geoid, and $TDT = TAI + 32.184$ seconds. *TDT* is an idealized uniformly flowing time independent of any fluctuations in Earth rotation or atomic fluctuations in *TAI*.

The independent time variable for dynamical theories usually needs to be taken at the center of mass of the solar system (*barycenter*). *Barycentric Dynamical Time (TDB)* is the *TDT* calculated after considering the constraints of the motion of the clock around the *barycenter*. *TDB* varies from *TDT* only by periodic variations due to this motion.

Coordinate Times (TCG & TCB)

In 1991 in an attempt to clarify relations between space-time coordinates, *Geocentric Coordinate Time (TCG)* and *Barycentric Coordinate Time (TCB)* were introduced. These two times are proper-times in the diction of General Relativity. *TCG* is the proper time at the center of the Earth's mass:

$$\mathrm{TCG} = \mathrm{TDT} + 6.969291 \times 10^{-10} \times (\mathrm{JD} - 2443144.5) \times 86400\mathrm{s} \qquad \text{(A.1)}$$

Where JD is the *Julian Day*, described below. *TCB* is the proper time at the *barycenter*.

$$\mathrm{TCB} = \mathrm{TDB} + 1.550505 \times 10^{-8} \times (\mathrm{JD} - 2443144.5) \times 86400\mathrm{s} \qquad \text{(A.2)}$$

Julian Day (JD & MJD)

The *Julian Day* is a continuous count of days since Greenwich mean noon on 4713 B.C. January 01. Astronomers usually use the *Modified Julian Day (MJD)*.
MJD = *JD* - 2400000.5. The zero point of *MJD* is 1858 November 17 00:00:00 UT. *MJD* can be expressed in *UT, TAI, TDT* etc. so for precise appliations the timescale should be specified *i.e.* MJD 50450.0000 TAI. *UT* is assumed if no other is specified.

Global Positioning Time (GPS)

GPS time is automatically steered to *UTC* on a daily basis to keep *GPS* time within one μs of *UTC* (plus or minus an integer number of leap seconds). During the last several years the difference between *GPS* and *UTC* has been within a few hundred ns. *GPS* time is *not* adjusted for leap seconds. Therefore, as of 1999 January 01, *GPS* is ahead of *UTC* by 13 seconds.

Unix Time

Time returned and used by many computer routines including the common routine *time_t* is *Unix Time*. *Unix Time* is a continuous count of SI seconds starting with zero at 1970 January 01 00:00:10 TAI. Timezone issues become seriously complicated in dealing with time in computer programs. Microsoft Windows© time routines store timezone information as minutes from GMT, after correcting for any Daylight Savings Time (DST). Various Unix routines keep track of timezone information as seconds from GMT, and have a flag to tell the system whether or not to correct for daylight savings time (DST). These differences must be taken into account if one is to successfully implement timing code using system time calls.

USA Time

The Time stored in the USA experiment is recorded in the local (satellite) time frame in UTC units. The reference for the start of counting is $MJDREF = 50454.0000$, which corresponds to 1997 January 06 00:00:00 UTC. Therefore, to convert from *USA* time to *MJD*, MJD = 50454.0 + USAtime/86400.0. *TIMEZERO* in the fits file header should be added to all time, but this value is zero for all USA observations.

The USA event time-tag is created in two parts. The first part consists of a 1 Hz pulse from ARGOS. This 1 Hz pulse is synchronized either from the internal ARGOS IEU oscillator or the higher quality 11 MHz temperature-controlled crystal oscillator (TCXO) in the GPS receiver. See §3.1.3 for more details on the USA GPS system. Each 1 Hz pulse is associated with a time in the corresponding NAV message sent from ARGOS. The second part of the time-tag is created by USA's event timer built into the Detector Interface Board (DIB). This counts microseconds from the last 1 Hz pulse and records these into the event time tag. The counting starts over when a new 1 Hz pulse is received.

Conclusion

The purpose of this appendix is to give the reader a general understanding of the complexities needed to be understood to perform detailed timing of astronomical events. Systems of time used in astrophysics may be taken for granted, but careful attention to coordinates must be taken into account if one is going to do precision timing. Also, this chapter gives the reader some useful information needed to convert from *USA* time to *MJD* and knowledge of intricacies of the time routines returned by commonly used computer programs. This knowledge is essential if one is creating a computer code to do time calculations or timing analysis in astronomy. For more detailed information on systems of time see ch. 2 of Seidelmann, Guinot, & Dogget (1992).

Appendix B

GLAST Beam Test Engineering Model (BTEM)

In this appendix my involvement with the GLAST BTEM is highlighted. I was involved in the mechanical testing (§B.2), electrical testing (§B.4), and analysis of BTEM data (§B.3). My testing work verified and improved methods of construction that will be used in the final GLAST instrument. The analysis work I performed is being used to develop new methods of background rejection and pair-production vertex location.

B.1 GLAST BTEM Overview

B.1.1 Introduction

The Gamma Ray Large Area Space Telescope (GLAST) mission is a silicon tracker, satellite based, gamma ray pair conversion telescope to be launched in 2006 (Michelson 1996; Atwood 1994). For more information on the planned mission see §3.3. The principal objectives of the GLAST mission involve the observation of energetic gamma rays, starting at 20 MeV and extending as high as TeV energies (Atwood et al. 2001; Michelson 1996; Atwood 1994).

The silicon tracker for the GLAST telescope will consist of $\sim$ one million readout

channels. To verify the design, and construction techniques, a beam test engineering model (BTEM) was constructed and tested at a fixed target end station at the Stanford Linear Accelerator Center (SLAC) and in a balloon flight. The BTEM corresponds structurally to 1/16 of the final instrument and about 4% of the total silicon. The BTEM tracker is a large, 2.7 m^2 silicon tracker, with 41600 readout strips and during it's operation was the largest inventory of good quality high yield detectors from 6 inch wafers. All the detectors, ladders and towers are interchangeable within the GLAST tracker. This is to keep a modular design. The only items not modular are the trays. Trays have different converter thickness reducing modularity (§B.1.2). The results of this beamtest can be found in do Couto e Silva et al. (2001). Results of the balloon flight of this instrument can be found in Kamae (2002).

The BTEM consists of a CsI calorimeter to measure the deposited energy, an Anti-Coincidence Detector (ACD) for background rejection and the tracker for measuring particle direction. The BTEM was tested in a beam of positrons, hadrons, and photons in 1999 December and 2000 January. The details of the tracker construction and plans for future construction are described in Allport et al. (2001). The curious reader can find even more information on the BTEM tracker construction in Tournear (2001).

B.1.2 Construction of the BTEM

Three or five detectors were edge-glued to each other (fig B.1) to form a ladder. As a ladder the detectors were wirebonded together and then the wirebonds were encapsulated. The ladders were then placed onto the top and bottom of aluminum frames that supported the ladders and electronics. There is no structural support or electronics attached to the ladders until they are attached to the trays. The BTEM silicon tracker is a pair conversion telescope, the passive converter is lead (tungsten will be used in the future). There are two thickness converters used, described in §B.1.2. These trays are stacked one on top of the other until they form a single tower with seventeen trays and sixteen $x-y$ layers of silicon (the topmost and bottommost trays only have silicon on the side towards the inside of the tracker). Trays are stacked

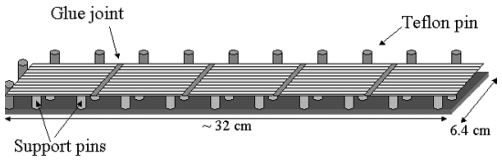

Figure B.1 Cartoon of the jig used for gluing detectors into 32 cm long ladders. In the future the detectors will be pushed against the pins by springs and held in place by vacuum.

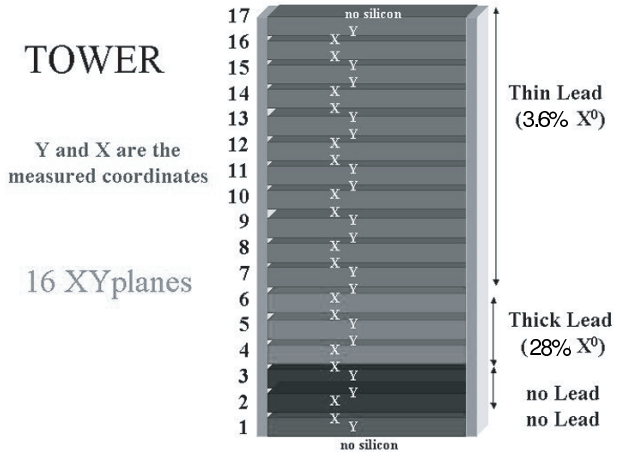

Figure B.2 Arrangement of the silicon layers in the BTEM tracker design.

such that there is only one plane of silicon after each converter. Each plane is made from two layers of silicon 3.2 mm apart, whose strips are oriented perpendicular to each other so that both an x and y position can be measured after each conversion (fig B.2).

The tracker also employs a self trigger mechanism that triggers an event when three consecutive planes are hit (six consecutive layers of silicon). Details of the front end electronics can be found in Chen (2000). Construction of the GLAST tracker is being led by Professor Robert Johnson of the University of California at Santa Cruz (UCSC)[1]

[1]See the UCSC tracker webpage http://scipp.ucsc.edu/groups/glast/ for more information.

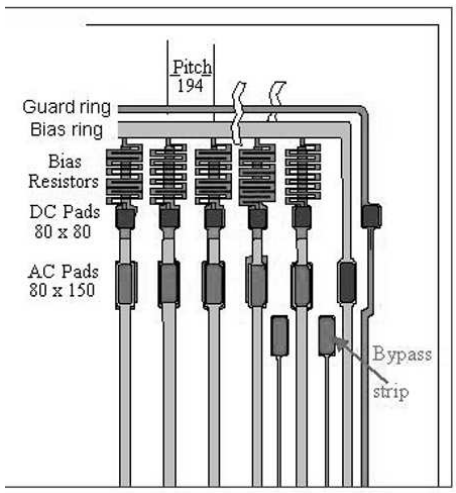

Figure B.3 Drawing showing details of silicon detectors used in the GLAST beamtest.

Silicon Detectors

The silicon detectors used in the beamtest were all single sided 400 μm thick high resistivity n-type silicon with a pitch of 194 μm. A drawing of the detector layout is shown in fig B.3. The silicon for the beamtest came from 6 inch and 4 inch wafers, with detectors sizes of 64.0 $\times$ 106.8 mm^2 and 64.0 $\times$ 64.0 mm^2 respectively. The detectors have 320 AC coupled strips with a 60 MΩ polysilicon bias resistor. The aluminum strip width is 52 μm. Detectors were patterned with bypass strips to allow bad channels to be bypassed. However, the number of bad channels was so small that no bypass strips were used, and they are removed in the final design.

There were 550 detectors ordered from Hamamatsu Photonics: 296 from 4 inch wafers and 254 from 6 inch wafers. In addition we also received 5 detectors from Micron Semiconductor Ltd. from 6 inch wafers, similar in design to the Hamamatsu detectors.

Detector Yield Table B.1 shows the BTEM silicon yield. The numbers in this table only include the 550 detectors from Hamamatsu. Of the 5 Micron detectors, 3 had stable leakage currents and were used in the BTEM tracker. The overall yield

Description	4 inch		6 inch		Total	
	Number	%	Number	%	Number	%
Good quality Detectors	280	94.6	251	98.8	531	**96.2**
Runaway or unstable leakage current	1	0.3	0	0.0	1	**0.2**
Unstable current after ladder assembly	13	4.4	3	1.2	16	**2.9**
Losses due to handling	2	0.7	0	0.0	2	**0.4**
Total	**296**	**100.0**	**254**	**100.0**	**550**	**100.0**

Table B.1 Silicon yield during the GLAST beamtest construction.

Number of Bad Channels			
	Number	**Total channels**	**Percentage**
Before Assembly, individual detectors	25	176000	0.01%
After assembly into ladders	21	41600	0.05%
After Beamtest	42	41600	**0.10**%

Table B.2 Bad channels during testbeam construction.

for silicon detectors was 96.5% (Atwood et al. 2001).

Bad Channels Table B.2 shows the progression of bad channels throughout the BTEM construction. When we received the detectors from the manufacturer the percentage of bad channels was 0.01%. After the ladders were constructed the bad channels were 0.05%. After the beamtest the number of bad channels increased to 0.10%, extremely low compared to typical silicon trackers, see ie. von Toerne et al. (2001).

Leakage Current All leakage currents throughout the testing process were measured at 100V. The average value was 3 nA/cm^2 and 2 nA/cm^2 for the 4 inch and 6 inch detectors respectively. Our initial specifications required the leakage current to be < 50 nA/cm^2, but since the detectors we received were of such high quality, this requirement has been changed to < 10 nA/cm^2 for the future.

Ladders

After receiving and testing the silicon detectors, they were assembled into ladders. All ladders in the BTEM tracker are the same length (32 cm), so ladders made from 6 inch detectors contain 3 detectors, and ladders made from 4 inch detectors contain 5 detectors.

Construction The ladders were constructed using a device similar to the drawing in fig B.1. The detectors were edge glued by referencing the edges of the detectors against Teflon pins. The glue was cured at 60°C for 2 hours. Some detector dicing cuts were inspected and the edges of the wafers were found to have chips on the order of 7 μm

The straightness of all the ladders was measured after the ladders were placed onto the trays. The average straightness of the ladders is 22 μm and most ladders fall within $10 - 30$ μm. The details of the alignment of the ladders is discussed in §B.2. Details on construction can be found in Atwood et al. (2001).

Leakage Current During ladder production the leakage current was measured for

- Detectors: upon delivery (before edge gluing)
- Detectors: after edge gluing (before wire bonding)
- Ladders: after wire bonding
- Ladders: after encapsulation of wirebonds.

Table B.3 shows how the ratio of leakage current per ladder changed before and after steps in production. There was no significant change except after wirebonding when the leakage current nearly doubled. There was also negligible change during the beam test. More details are found in (Allport et al. 2001).

Ladder Yield Table B.4 shows the breakdown of the ladder yield. The overall ladder yield was 97.7%. Details of the repairs can be found in (Allport et al. 2001).

Production Step	$\frac{I_{leak}\ \text{after step}}{I_{leak}\ \text{before}}$
Before Gluing	1
After Gluing	1.08 ± 0.28
After Wirebonding	1.61 ± 0.41
After Encapsulation	0.92 ± 0.29

Table B.3 Leakage current progression for all ladders though the production steps.

Ladder Production Summary		
Good ladders	**130**	**93.5%**
rejected: high current	2	1.4%
rejected: large misalignment	1	0.7%
repaired: leaky detector	1	0.7%
repaired: handling errors	3	2.2%
repaired: glue failure	1	0.7%
repaired: other	1	0.7%
Total:	139	100.0%

Table B.4 Ladder yield during beamtest construction.

Trays

The structural support modules of the GLAST tracker are the trays. An exploded view of the trays can be seen in fig B.4. The trays are made of an aluminum closeout frame with an aluminum hexcel core. Carbon fiber sheets are glued to the top and bottom of the aluminum core to give the tray rigidity. On the top of the tray there is a kapton printed circuit glued to the carbon and the silicon ladders are glued on top of this circuit. On the bottom of the tray, there is a lead converter placed between the carbon sheet and the kapton circuit. Two different converter thickness are used, 3.6% X_0 towards the top of the tracker, 28% X_0 towards the bottom and the bottommost two trays containing no lead converters. The electronics are mounted on the sides of the tray to minimize dead area in the tracker.

The ladders were glued into the trays using shims for alignment. The positions of

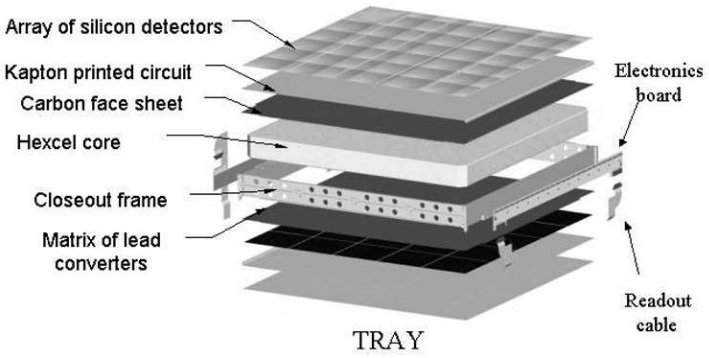

Figure B.4 Drawing showing the construction of the trays.

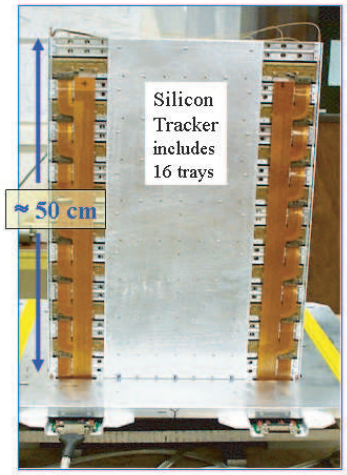

Figure B.5 Picture of the BTEM tracker, plates have been removed to clearly show the seventeen trays stacked on top of each other. The overall tracker size is 32 cm × 32 cm × 50 cm.

the ladders were measured after construction. The results showed that the ladders are systematically rotated within the tray an average of 0.007° with a random rotation of 0.01°. Details of these measurements are described in §B.2.

After tray construction the trays are stacked one on top of each other to make up the entire tracker (fig B.5).

B.1.3 Future Plans

The final GLAST instrument will include 16 towers each somewhat larger than the BTEM and contains 74 m^2 of silicon microstrip detectors. The entire GLAST instrument has a mass of 3000 kg and uses 650 W of power (about 10 modest size lightbulbs worth of power).

Detector changes

The detector design used in the final detector will be similar to the 6 inch wafer detectors used in the BTEM. The differences include: increasing the pitch to 228 μm for power consumption concerns; removing the bypass strips; detector dimensions are 8.95×8.95 cm^2; there will be 320 readout strips per detector. GLAST will contain 9216 detectors in 2304 ladders each with 4 detectors. The silicon to silicon glue also had to be changed to EPO-TEK 2216, a 24 hour room temp cure, to meet space qualifications.

Other changes to the instrument include: optimizing converter thickness, changing converter material to tungsten instead of lead, and changing the way the electronics are mounted onto the trays. Thicker converters collect more photons, but at the price of reducing angular resolution. The converter material must be chosen to minimize thermal expansion mismatch with the silicon and have a small X_0 to convert photons. The way the electronics were mounted to the BTEM required bending the kapton circuit around a corner, making repairs difficult. The new design has the kapton attached to a curved piece that can be replaced, allowing for removal of the electronics.

B.1.4 Conclusion

The GLAST BTEM taught us: single sided 6 inch wafer technology from Hamamatsu is very viable. The detectors from these wafers have an average of 2 nA/cm^2 leakage current at 100V and $< 0.1\%$ bad channels. During the GLAST BTEM high yields were achieved, 96.5% for detectors and 97.7% for ladders. This is attributed to simple robust designs that minimize handling and chances for errors. Having a modular design is very important in maintaining a high yield. Almost all of the components

of the GLAST tracker are interchangeable, the exception coming from the different thickness converters.

B.2 Tray Alignment Measurements

Introduction

As part of the R&D to develop and prove the final GLAST silicon tracker design the GLAST BTEM silicon trays were measured to determine the precision of the alignment of the silicon detectors in a ladder, and the precision of the ladders within a tray. The survey was used to determine the quality of our chosen construction method, and to construct a starting point for the reconstruction software.

Procedure

The surveying was performed using a CCD camera with magnifying optics, mounted on a measuring table. The table can be moved by linear encoders in increments of 1 μm, but the precision of the measurements (5.1 μm in x and y) was limited by the camera resolution ($\approx$ 4 μm). The precision of the vertical measurement, z, was limited by the ability to reliably focus the camera at the same height above the measuring surface. This error was estimated to be $\pm$30 μm. A PC using a pattern recognition algorithm was used to control the moveable table, to identify fiducial marks, measure the corresponding x and y coordinates and store the measurement data to a file. The locations of the fiducials on each detector were measured, and in addition, the locations of the dowel pin holes on the tray were measured for reference.

Analysis

Z measurement calibration

Several cross checks were performed to obtain the aforementioned results. The z values returned by the measuring machine and the actual z values needed to be correlated. Measuring a series of gauge blocks of a known height and fitting the

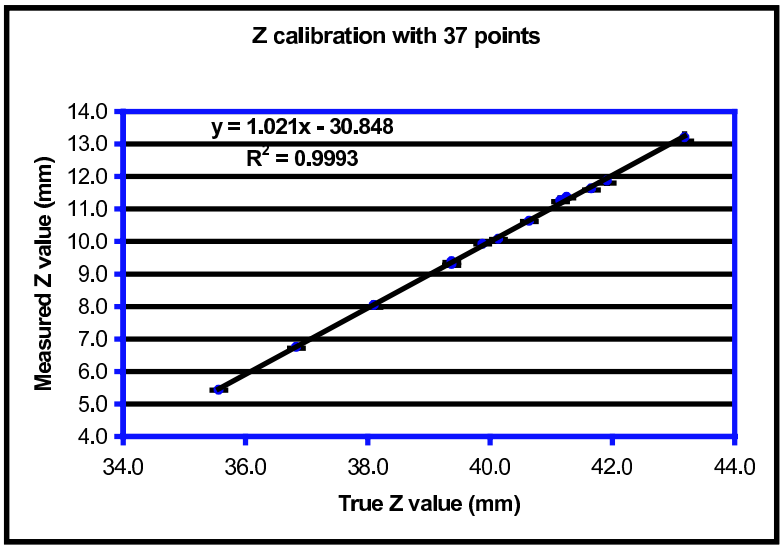

Figure B.6 Calibration of z measurement, obtained by measuring z values of known gauge block heights.

measured value to the known values we obtained a relationship between the two, see Figure B.6.

Alignment of detectors within a ladder

The first step in analyzing construction of the trays was to find the alignment of the individual detectors within the ladder. A straight line was calculated for each side of each ladder, see Figure B.7. These lines were calculated using the method of least squares fitting. Using the equations for these lines an ideal location in y was calculated for each measured value if x. The difference between actual and ideal values of y were calculated; for each line the maximum $-$ minimum deviation was calculated and recorded as the *straightness* of the line. The results of these straightness measurements are plotted in Figure B.8. The abscissa contains the number of lines with a given straightness (two lines per each ladder). A Gaussian fit is applied yielding an average misalignment of 22 μm $\pm$11 μm, with four out of 130 ladders having a misalignment greater than 60 μm, with a reduced $\chi^2 = 1.3$.

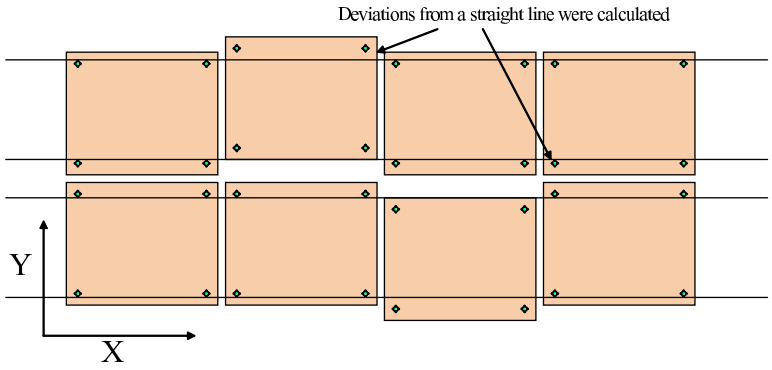

Figure B.7 Drawing showing how measurement of the engineering tolerance *straightness* was calculated. *Straightness* is the total deviation from a straight line.

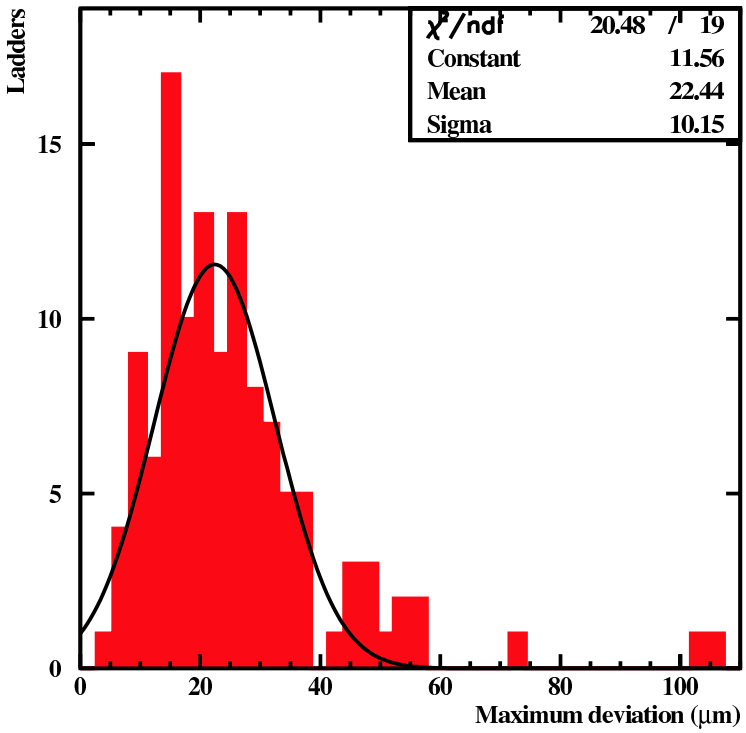

Figure B.8 Distribution of the straightness of the ladders, there are 244 points included in this plot.

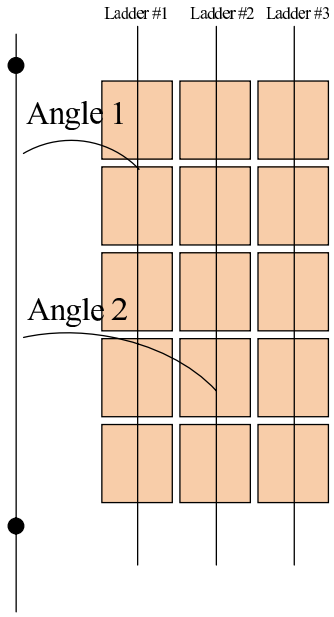

Figure B.9 Drawing showing how the angle between each ladder and the dowel pins describing the tray is measured.

Alignment of ladders within a tray

The second step involved checking the alignment of the ladders within the tray. A reference line, for both the top and bottom of the tray, was calculated using two dowel pin holes on the tray. Using the two lines per ladder calculated above, an average line was constructed. This gives one line that describes each ladder Figure B.9. Using this information the angle between the dowel pin line and the line describing each ladder is calculated. The results from this analysis, shown in Figure B.10, show the trays are misaligned with respect to the corner posts 30 ± 60 μm, where this is the calculated run-out from an angle of 0.01° over 31.8 cm (the length of the ladder). The error is statistical only; any systematic errors can be neglected, the starting point on the trays was measured after measuring the ladders. If any indication of tray motion was detected the values were not used in determining the alignment of the ladders in this analysis.

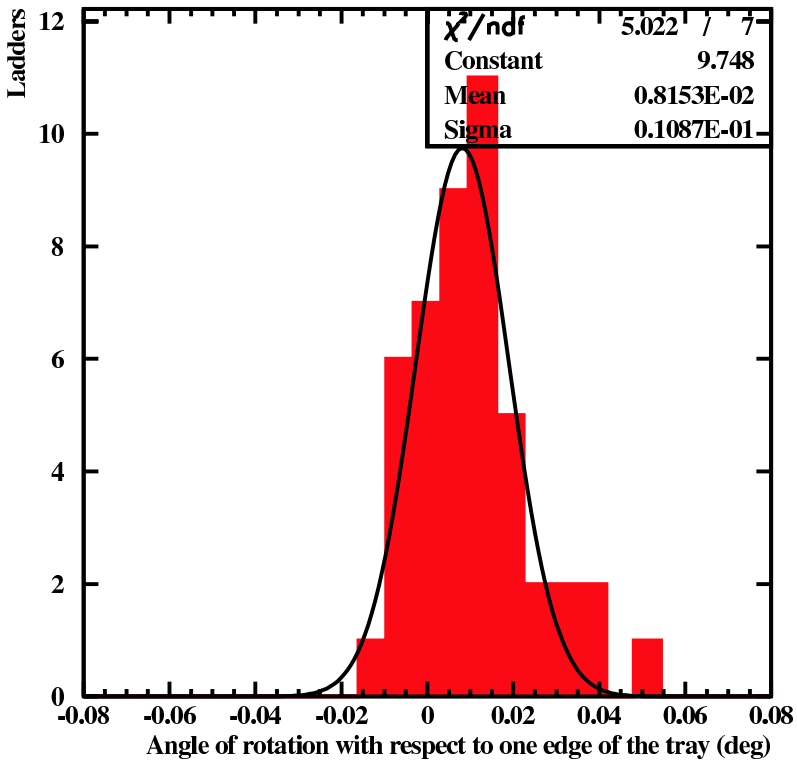

Figure B.10 Distribution of the angles between the assembled ladders and the trays. There are 93 points in this plot, one for each ladder that did not move during measurement. An angle of 0.01° corresponds to a run-out of 55μm along the length of the ladder.

Z measurement of the trays

The third step in analysis was to determine the distance between the planes of silicon on the same tray. The top and bottom could not be measured at the same time, so the distance had to be calculated.

- The distance from the silicon to the granite plate was measured as well as the distance from the corner posts to the granite plate.

- The difference in the two measurements above can be attributed to lead thickness, glue thickness and kapton thickness. The details can be seen in Figure B.11.

- Using this diagram and measured values for the height of silicon and height of corner posts an average value of the glue gap was calculated: 40 μm. This was accomplished by taking the difference in height from the top of the silicon to the top of the corner post, then subtracting the known values from Figure B.11, leaving only the glue gaps as a free variable, found the total thickness of glue. Dividing this value by the number of glue gaps in the calculation gives an average glue gap per tray. All of these values were averaged to obtain an average glue gap of 30 μm, which is what was expected ($25 - 50$ μm).

- Using the calculated average glue gap the difference between top and bottom silicon faces was calculated. This distance = Silicon Z - block + glue thickness + carbon thickness + glue thickness + kapton thickness + spacer + SSD thickness (these values are defined by Figure B.11). The measured distances between SSD surfaces on the same tray are: 29.66 ± 0.20 mm for trays with 0.2 mm of lead (expected 29.65 mm); 29.52 ± 0.11 mm for super GLAST trays (expected 29.45 mm); 29.60 ± 0.15 mm for the trays with no lead (expected 29.41 mm). The differences from nominal values are shown graphically in Figure B.12. There are two measurements for each tray since the plane spacing was calculated independently for both the top plane and the bottom plane.

These values were used to determine the amount of pair creations occurring inside the converter. The value of the z position of the vertex was determined by the BTEM reconstruction software. Using this value, the measured values of the position of the silicon and detailed drawings of the BTEM layout, we were able to construct of map of where the vertex locations were in relationship to position in the tracker. Figure B.13 shows where the conversions occurred. One can see there are significant numbers of vertices outside the converters, but all vertices appear to be tightly distributed near the converters.

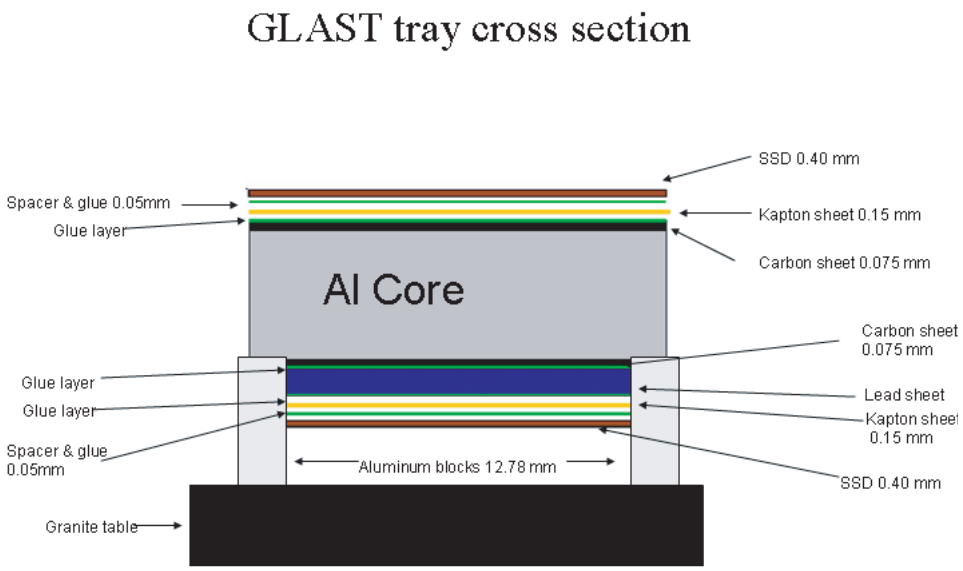

Figure B.11 Drawing showing the components in the cross-section of the GLAST BTEM tray. The thicknesses of the glue layers were unknown and calculated based on the z position measurements.

Creating Map for Monte Carlo

The last step was constructing a map that will be used as a first estimation of where the silicon trays are in the Monte Carlo simulation, Table B.5. The column headings are:

Plane 0 to 15 from bottom to top of tower, corresponding to readout sequence.

Position 1 to 17, physical stager position.

Closeout ID labels in the closeout, done in the clean room.

Tray type :

0 - bottom closeout

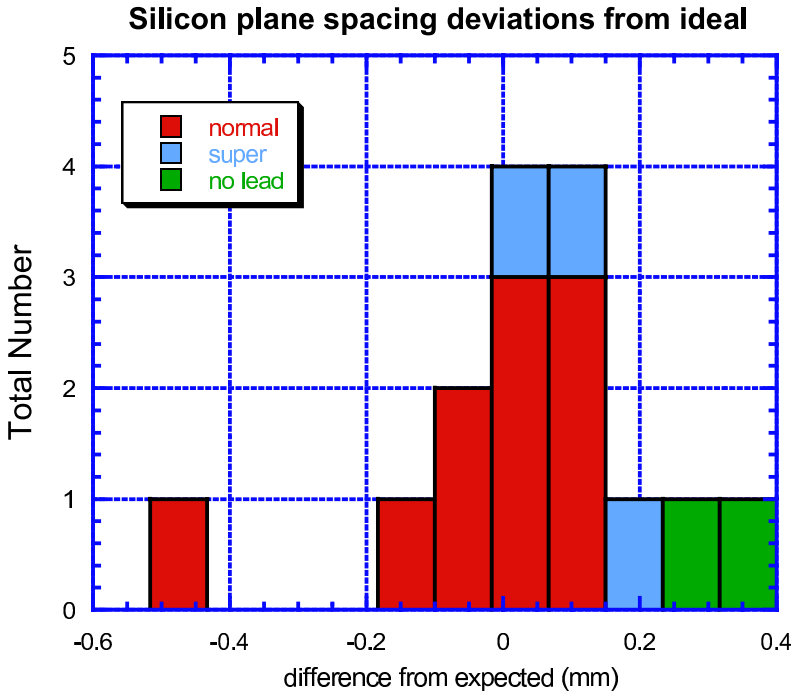

Figure B.12 Distribution of the difference between the ideal position of a layer of silicon in z and the actual position of the silicon. There are two points for each tray, separated on the thickness of the converter in the tray, *normal* converter = 3.6% $X_\circ$, *super* converter = 28% $X_\circ$, *no lead* no converter.

1 - tray with no lead

2 - tray with thin lead 3.6% $X_\circ$

3 - super GLAST tray 28% $X_\circ$

Tray side 0 for bottom 1 for top

Ladder type 0 - 4 inch detectors

1 - 6 inch Hamamatsu detectors

2 - 6 inch Micron detectors

Ladder position $1-5$

Ladder number is the assembly ID of the ladder

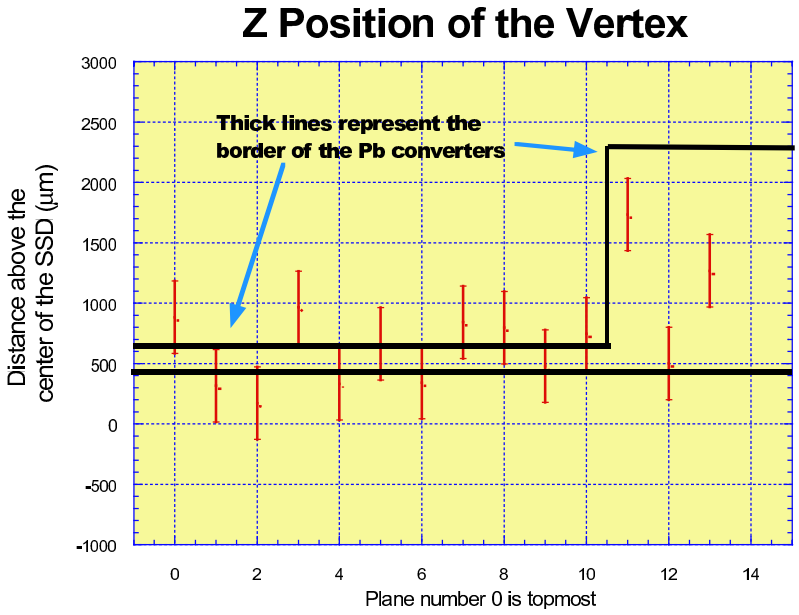

Figure B.13 Distribution of the location of reconstructed pair conversion positions in z for photon candidates in units of microns above the center of the silicon detector. The thick lines represent the borders of the lead converters in the BTEM, where conversions are expected.

Flag for intercept offset This is a flag where the line intercept is not the line through the center of the ladder. In these cases only one side of the ladder could be measured due to constraints of the measuring table.

								with respect to cornerposts		SSD center w/r/t bottom SSD	Offset
Plane	Tray Position	Closeout ID	Tray Type	Tray Side	Ladder Type	Ladder Pos.	Ladder num.	slope	intercept	Z	Flag
15	17	4	2	0	0	1	49	1.6E-04	-35.0	0.00	483.53	0
15	17	4	2	0	0	2	6	4.7E-05	-99.2	0.00	483.53	0
15	17	4	2	0	0	3	18	-5.5E-05	-163.3	0.00	483.53	0
15	16	16	2	1	0	1	30	6.8E-04	-35.1	29.70	481.00	0
15	16	16	2	1	0	2	9	8.6E-04	-99.4	29.70	481.00	0
15	16	16	2	1	0	3	28	1.3E-03	-163.7	29.70	481.00	0
14	16	16	2	0	0	1	8	1.3E-04	-35.0	0.00	451.66	0
14	16	16	2	0	0	2	10	1.1E-04	-99.2	0.00	451.66	0
14	16	16	2	0	0	3	11	1.0E-04	-163.4	0.00	451.66	0
14	15	15	2	1	2	1	139	-1.1E-03	-35.0	29.28	448.93	0
14	15	15	2	1	0	2	13	-1.3E-03	-99.2	29.28	448.93	0
14	15	15	2	1	0	3	14	-1.5E-03	-163.5	29.28	448.93	0
13	15	15	2	0	0	1	15	1.6E-05	-34.9	0.00	419.80	0
13	15	15	2	0	0	2	16	-1.9E-04	-99.1	0.00	419.80	0
13	15	15	2	0	0	3	17	-2.3E-04	-163.3	0.00	419.80	0
13	14	8	2	1	0	1	19	-4.2E-04	-35.0	29.81	416.87	0
13	14	8	2	1	0	2	20	-6.4E-04	-99.2	29.81	416.87	0
13	14	8	2	1	0	3	21	-7.6E-04	-163.4	29.81	416.87	0
12	14	8	2	0	0	1	22	-2.1E-04	-35.0	0.00	387.39	0
12	14	8	2	0	0	2	23	-1.9E-04	-99.2	0.00	387.39	0
12	14	8	2	0	0	3	24	-5.8E-04	-163.4	0.00	387.39	0
12	13	7	2	1	0	1	25	-2.7E-04	-34.9	29.67	384.80	0
12	13	7	2	1	0	2	56	-4.1E-04	-99.1	29.67	384.80	0
12	13	7	2	1	0	3	27	-4.3E-04	-163.3	29.67	384.80	0
11	13	7	2	0	0	1	29	-2.4E-04	-34.9	0.00	355.29	0
11	13	7	2	0	0	2	3	-1.4E-04	-99.2	0.00	355.29	0
11	13	7	2	0	0	3	12	-1.6E-04	-163.4	0.00	355.29	0
11	12	6	2	1	0	1	32	-5.1E-07	-35.0	29.65	352.73	0
11	12	6	2	1	0	2	33	-1.7E-05	-99.2	29.65	352.73	0
11	12	6	2	1	0	3	34	-4.4E-05	-163.4	29.65	352.73	0
10	12	6	2	0	0	1	35	2.1E-04	-35.0	0.00	323.33	0

Plane	Tray Position	Closeout ID	Tray Type	Tray Side	Ladder Type	Ladder Pos.	Ladder num.	with respect to cornerposts slope	intercept	Z	SSD center w/r/t bottom SSD Z	Offset Flag
10	12	6	2	0	0	2	36	7.2E-05	-99.2	0.00	323.33	0
10	12	6	2	0	0	3	37	3.8E-05	-163.4	0.00	323.33	0
10	11	5	2	1	0	1	51	-2.3E-04	-34.9	29.58	320.67	0
10	11	5	2	1	0	2	39	-4.0E-04	-99.1	29.58	320.67	0
10	11	5	2	1	0	3	40	2.8E-04	-163.4	29.58	320.67	0
9	11	5	2	0	0	1	41	3.1E-04	-35.0	0.00	291.21	0
9	11	5	2	0	0	2	42	2.5E-04	-99.2	0.00	291.21	0
9	11	5	2	0	0	3	43	2.1E-04	-163.4	0.00	291.21	0
9	10	3	2	1	0	1	44	8.9E-04	-35.0	29.63	288.60	0
9	10	3	2	1	0	2	45	1.6E-03	-99.3	29.63	288.60	0
9	10	3	2	1	0	3	46	1.7E-03	-163.5	29.63	288.60	0
8	10	3	2	0	0	1	47	7.2E-04	-35.0	0.00	258.84	0
8	10	3	2	0	0	2	48	3.6E-04	-99.1	0.00	258.84	0
8	10	3	2	0	0	3	52	8.8E-05	-163.3	0.00	258.84	0
8	10	3	2	0	0	4	31	-4.2E-04	-227.5	0.00	258.84	0
8	9	9	2	1	1	1	135	-1.9E-04	-35.0	29.65	256.53	0
8	9	9	2	1	1	2	136	-5.8E-05	-99.2	29.65	256.53	0
8	9	9	2	1	1	3	137	-5.8E-05	-163.4	29.65	256.53	0
8	9	9	2	1	1	4	138	-1.1E-04	-227.6	29.65	256.53	0
7	9	9	2	0	0	1	53	2.5E-04	-34.9	0.00	226.77	0
7	9	9	2	0	0	2	54	1.7E-04	-99.1	0.00	226.77	0
7	9	9	2	0	0	3	55	3.0E-05	-163.3	0.00	226.77	0
7	9	9	2	0	0	4	57	-9.4E-05	-227.5	0.00	226.77	0
7	9	9	2	0	0	5	50	-1.4E-04	-260.1	0.00	226.77	1
7	8	12	2	1	1	1	63	5.6E-04	-34.9	29.72	224.47	0
7	8	12	2	1	1	2	64	6.0E-04	-99.1	29.72	224.47	0
7	8	12	2	1	1	3	65	6.2E-04	-163.3	29.72	224.47	0
7	8	12	2	1	1	4	66	5.6E-04	-227.6	29.72	224.47	0
7	8	12	2	1	1	5	67	5.7E-04	-260.2	29.72	224.47	1
6	8	12	2	0	1	1	68	-5.7E-04	-35.0	0.00	195.07	0
6	8	12	2	0	1	2	69	-5.0E-04	-99.2	0.00	195.07	0
6	8	12	2	0	1	3	70	-5.7E-04	-163.4	0.00	195.07	0

Plane	Tray Position	Closeout ID	Tray Type	Tray Side	Ladder Type	Ladder Pos.	Ladder num.	with respect to cornerposts slope	intercept	Z	SSD center w/r/t bottom SSD Z	Offset Flag
6	8	12	2	0	1	4	71	-5.8E-04	-227.6	0.00	195.07	0
6	8	12	2	0	1	5	72	-4.4E-04	-260.3	0.00	195.07	1
6	7	14	2	1	1	1	73	8.2E-06	-35.0	29.61	192.40	0
6	7	14	2	1	1	2	74	-6.6E-05	-99.2	29.61	192.40	0
6	7	14	2	1	1	3	75	8.2E-05	-163.4	29.61	192.40	0
6	7	14	2	1	1	4	76	1.1E-04	-227.6	29.61	192.40	0
6	7	14	2	1	1	5	77	1.3E-04	-260.3	29.61	192.40	1
5	7	14	2	0	1	1	78	-2.7E-05	-35.0	0.00	163.01	0
5	7	14	2	0	1	2	79	-1.1E-04	-99.2	0.00	163.01	0
5	7	14	2	0	1	3	80	-1.4E-04	-163.4	0.00	163.01	0
5	7	14	2	0	1	4	81	-1.3E-04	-227.6	0.00	163.01	0
5	7	14	2	0	1	5	82	8.3E-07	-260.3	0.00	163.01	1
5	6	18	3	1	1	1	83	6.6E-05	-35.0	29.50	160.33	0
5	6	18	3	1	1	2	84	-2.7E-04	-99.2	29.50	160.33	0
5	6	18	3	1	1	3	85	-5.2E-04	-163.4	29.50	160.33	0
5	6	18	3	1	1	4	86	-8.5E-04	-227.6	29.50	160.33	0
5	6	18	3	1	1	5	87	-1.1E-03	-260.2	29.50	160.33	1
4	6	18	3	0	1	1	88	-1.7E-04	-35.0	0.00	130.76	0
4	6	18	3	0	1	2	89	-1.8E-04	-99.2	0.00	130.76	0
4	6	18	3	0	1	3	90	-2.2E-04	-163.4	0.00	130.76	0
4	6	18	3	0	1	4	91	-1.6E-04	-227.6	0.00	130.76	0
4	6	18	3	0	1	5	92	-9.1E-05	-260.3	0.00	130.76	1
4	5	17	3	1	1	1	93	1.9E-04	-35.0	29.57	128.27	0
4	5	17	3	1	1	2	94	2.0E-04	-99.2	29.57	128.27	0
4	5	17	3	1	1	3	95	2.1E-04	-163.5	29.57	128.27	0
4	5	17	3	1	1	4	97	1.3E-04	-227.7	29.57	128.27	0
4	5	17	3	1	1	5	98	2.0E-04	-260.4	29.57	128.27	1
3	5	17	3	0	1	1	119	-4.3E-04	-34.9	0.00	98.83	0
3	5	17	3	0	1	2	120	-5.2E-04	-99.1	0.00	98.83	0
3	5	17	3	0	1	3	121	-5.9E-04	-163.3	0.00	98.83	0
3	5	17	3	0	1	4	122	-7.1E-04	-227.5	0.00	98.83	0
3	5	17	3	0	1	5	123	-8.7E-04	-260.2	0.00	98.83	1

Plane	Tray Position	Closeout ID	Tray Type	Tray Side	Ladder Type	Ladder Pos.	Ladder num.	with respect to cornerposts slope	intercept	Z	SSD center w/r/t bottom SSD Z	Offset Flag
3	4	19	3	1	1	1	104	5.3E-04	-35.0	29.46	96.20	0
3	4	19	3	1	1	2	105	5.0E-04	-99.2	29.46	96.20	0
3	4	19	3	1	1	3	106	5.2E-04	-163.4	29.46	96.20	0
3	4	19	3	1	1	4	107	5.1E-04	-227.6	29.46	96.20	0
3	4	19	3	1	1	5	108	8.2E-04	-260.4	29.46	96.20	1
2	4	19	3	0	1	1	109	2.6E-04	-35.0	0.00	66.98	0
2	4	19	3	0	1	2	110	2.5E-04	-99.2	0.00	66.98	0
2	4	19	3	0	1	3	111	2.5E-04	-163.4	0.00	66.98	0
2	4	19	3	0	1	4	112	5.4E-04	-227.7	0.00	66.98	0
2	4	19	3	0	1	5	113	5.8E-04	-260.3	0.00	66.98	1
2	3	13	1	1	1	1	114	2.0E-04	-35.0	29.55	64.13	0
2	3	13	1	1	1	2	115	1.1E-04	-99.2	29.55	64.13	0
2	3	13	1	1	1	3	116	1.5E-04	-163.4	29.55	64.13	0
2	3	13	1	1	1	4	117	3.8E-06	-227.6	29.55	64.13	0
2	3	13	1	1	1	5	118	-5.6E-04	-260.3	29.55	64.13	1
1	3	13	1	0	1	1	99	-2.6E-04	-35.0	0.00	34.53	0
1	3	13	1	0	1	2	100	-5.6E-04	-99.2	0.00	34.53	0
1	3	13	1	0	1	3	101	-7.7E-04	-163.5	0.00	34.53	0
1	3	13	1	0	1	4	102	-9.2E-04	-227.7	0.00	34.53	0
1	3	13	1	0	1	5	103	-1.3E-03	-260.3	0.00	34.53	1
1	2	10	1	1	1	1	124	4.6E-05	-34.9	29.67	32.07	0
1	2	10	1	1	1	2	125	7.1E-07	-99.1	29.67	32.07	0
1	2	10	1	1	1	3	126	-1.3E-06	-163.3	29.67	32.07	0
1	2	10	1	1	1	4	127	-5.9E-05	-227.5	29.67	32.07	0
1	2	10	1	1	1	5	128	-1.7E-04	-260.2	29.67	32.07	1
0	2	10	1	0	1	1	58	1.5E-03	-34.9	0.00	3.57	0
0	2	10	1	0	1	2	59	1.4E-03	-99.0	0.00	3.57	0
0	2	10	1	0	1	3	60	1.1E-03	-163.2	0.00	3.57	0
0	2	10	1	0	1	4	61	1.1E-03	-227.4	0.00	3.57	0
0	2	10	1	0	1	5	62	1.1E-03	-260.1	0.00	3.57	1
0	1	20	0	1	1	1	129	-4.5E-04	-34.9	35.04	0.00	0
0	1	20	0	1	1	2	130	-5.2E-04	-99.1	35.04	0.00	0

Plane	Tray Position	Closeout ID	Tray Type	Tray Side	Ladder Type	Ladder Pos.	Ladder num.	with respect to cornerposts slope	with respect to cornerposts intercept	with respect to cornerposts Z	SSD center w/r/t bottom SSD Z	Offset Flag
0	1	20	0	1	1	3	131	-5.1E-04	-163.3	35.04	0.00	0
0	1	20	0	1	1	4	132	-6.4E-04	-227.5	35.04	0.00	0
0	1	20	0	1	1	5	133	-6.3E-04	-260.2	35.04	0.00	1

Table B.5: Alignment Map For Monte Carlo Simulation

Conclusion

For the next phase of GLAST construction more care should be made in aligning the ladders to the trays. The ladders are built within the specifications, ± 50 μm in x,y, with the straightness of the ladders being very good at 20 μm. The majority of the error in overall alignment occurred in placing the ladders within the trays. The distance between the planes of silicon within the trays not containing lead and what was expected is outside of measuring error. During production when the trays are measured they should be clamped or held down to the measuring surface during measurement to keep the part from moving while being measured. Table B.5 was used as a starting place during reconstruction and helped in the aligning process using tracks.

B.3 GLAST BTEM Time Over Threshold (TOT) Analysis

B.3.1 Introduction

The information read out from the GLAST silicon tracker will be the layer and channel that were hit, and the Time over Threshold (TOT) per layer, which is the amount of time any of the strips in any given layer contain a deposited charge over some pre-determined threshold value. TOT is an OR circuit, so if more than one strip is hit, the one with the maximum charge is recorded.

One of the main complications affecting GLAST is the large rate of high energy charged cosmic rays that will be incident on the satellite in orbit. If not carefully reconstructed these charged particles can be mistaken for high-energy photons. To help eliminate this background a shroud of plastic scintillators covers the silicon tracker almost completely. These scintillators detect charged particles passing through with > 0.9997 efficiency, and can be used to veto the events caused by these charged particles. This shroud of scintillators and associated electronics is called the Anti-Coincidence Detector (ACD). The ACD is not 100% efficient (Sadrozinski 2001);

so we look to the TOT to improve the charged particle veto rate. If a charged particle enters the tracker the TOT can be non-zero in every plane of silicon through the tracker. Therefore, this can be used as a charged particle signature, in addition to others discussed later. With this information the TOT can be used to increase the veto efficiency (some advantage can be achieved with hit strips only).

Another job of the tracker, its main job, is proper reconstruction of the direction of the incoming gamma rays undergoing pair production. Proper location of the pair-production location aides in the reconstruction of the incoming photon. The gamma ray enters the tracker and moves through converter foils. Inside these converters the gamma ray can pair produce, then the electron and positron are tracked as they move through the tracker. If the electron and positron are close together they should deposit their charge onto one strip (occurs most of the time). This should register a TOT value of twice what a single charged cosmic ray would register on a single strip. This gives us a signature that we can look for to let us know where the pair-production occurred to help aid in the track reconstruction see Figure B.14. This is the value of the TOT over strip hits alone.

B.3.2 TOT Operation

B.3.3 Purpose and Description of TOT

The TOT gives a measurement of the average amount of energy deposited in a silicon strip per layer. The TOT measures the amount of time that the charge on a given strip is above a threshold value. The original motivation for the TOT was to remove background from tracks backscattering from the calorimeter into the tracker. Tracks that come from the calorimeter and stop in the tracker will not have hit an ACD tile and will look like a photon event (Nikolaou 2000). Through more analysis we have found that the TOT can be used to find photon pair conversion points along with helping to aid in charged background rejection.

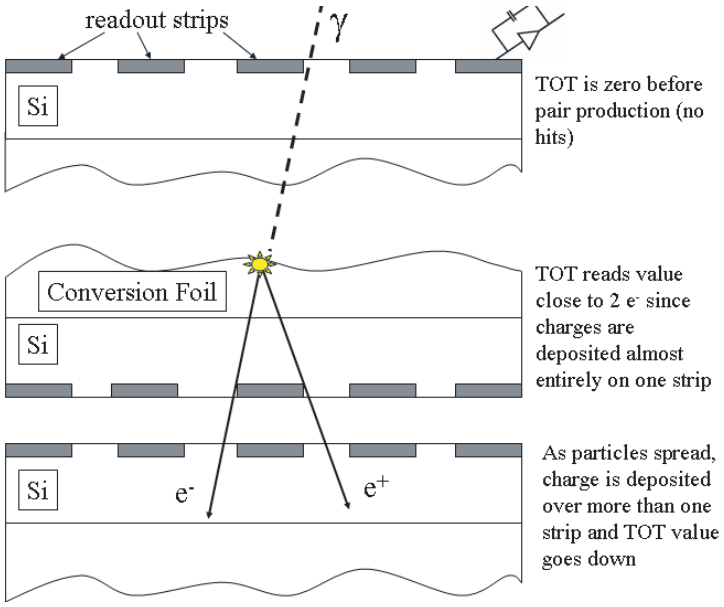

Figure B.14 This drawing shows the progression of a normal photon conversion in the GLAST tracker. Until the photon passes through enough material to pair produce, it will not register any hits, and therefore the TOT value will be zero. Then in the layer just after conversion the e^- and e^+ are close enough together to hit on only one strip, so the TOT registers a value close to 2 MIPs. Then as the particles scatter through the tracker they spread their charge over more than one strip and the TOT goes to a value closer to that corresponding to one MIP.

B.3.4 Readout Process of TOT

The TOT measurement and readout process is mainly carried out by three units: the silicon detector readout strips, the hybrid board electronics and the tower TEM board (Sadrozinski 2001). Some general information on the TOT (Nikolaou 2000):

- The GTRC chip of any silicon layer starts to count the TOT whenever a *channel trigger* triggers the *trigger fast-OR*. The GTRC chip will continue to count the TOT until all of the strips in that layer have returned to a value of charge below the threshold.

- TOT is checked each cycle of the GTRC-chip, every 200 ns (1 count = 200 ns).

- The TOT value calculated in the GTRC-chip will automatically reset and be discarded after approximately 1.5 μs, unless a *trigger acknowledge* signal is received from the TEM.
- If a *channel trigger* has occurred and the *fast-OR* line (from FE-chips to GTRC) becomes low (i.e. end of event) before a *trigger acknowledge* signal arrives from the TEM, the current TOT is discarded and the counter reset.
- By injecting charge into a known capacitor the linearity of the TOT has been measured up to 20 MIPs. A MIP is estimated to be around 6–7 μs (Kroeger, W. private communication).

Now we will step through a typical TOT readout (Nikolaou 2000).
A charged particle passes through the silicon detector. This ionizes electrons within the silicon and they migrate to the readout strips. If the amount of charge that is deposited onto the strips is above a threshold level, a *channel trigger* has occurred (a hit). This channel trigger generates a *trigger fast-OR*, meaning the fast-OR line, connecting FE-chips, controller and TEM-board, is raised. On its way down to the TEM-board, the fast-OR signal starts a counter in the controller chip (GTRC), the TOT counter. This counter continues to count until all of the strips in that layer have returned to a value below the threshold value. When the TEM-board receives the fast-OR signal it checks if a *level-1 trigger* has occurred. A level-1 trigger occurs when the TEM receives fast-OR signals from 6 consecutive layers. When the TEM decides that a level-1 trigger has occurred, it send a *trigger acknowledge* signal back to the FE-chips. The trigger acknowledge signal tells the FE-chips to save their data in a FIFO buffer. Approximately 30 μs later, a *read event* command is sent from the TEM to all the controller chips, this command tells the controller chips to start reading the FE-chip data and store the bit-stream into the controller chip's buffer. Finally, a *readout token* is sent from the TEM to the controller chip of the nearest silicon layer. The token grants the controller chip the exclusive right to start sending it's stored data down to the TEM. The controller chip will wait until all data have been read from the FE-chips, and the TOT is done counting. The bundle of data is sent to the TEM and the readout token is passed to the next layer (Nikolaou 2000).

B.3.5 TOT Calibration

The TOT is stored as clock counts. This can easily be converted to μs (one count = 200 ns). However, to get useful information from these times we need to understand how the time correlates to amount of charge deposited on the strips. The calibration was performed by injecting charge via an external capacitor into a single amplifier channel and measuring the corresponding width of the fast-OR signal. The response was linear up to 20 MIPs (1 MIP $\simeq$ 7 μs) and for larger input signals, saturation was seen with typical widths of the order of 100 μs. To get the relationship between TOT and energy deposited in data we analyzed two positron runs. One, run number 283, had a 20 GeV beam energy; and the other, run number 360, had a 2 GeV beam energy.

For each run, 360 and 283, histograms of the TOT values for each layer were plotted, see Figure B.15. A Landau distribution curve[2] was fit to each plot. The distribution of the means for each layer and both runs are given in Table B.3.5. These numbers are from the Landau fits of positron TOT data (Figure B.15). The average was used as a calibration for each layer to convert TOT from time to MIPs. Layer 17 fell during the beam test, making the data from this layer unusable. Almost all of the values fall between $6-7$ μs. On average the values from the 20 GeV run are 0.5 μs higher than the values from the 2 GeV run, $\lesssim 10\%$ effect. This effect can be attributed to the fact that on the dE/dx vs. Energy curve we are in the logarithmic rise portion, so the relationship between the amount of energy deposited and TOT is small. Therefore, the average value between these two runs can be used as our calibration value. This value roughly corresponds to the amount of time one strip is pushed above threshold by a Minimum Ionizing Particle (MIP) passing through the silicon. We now have measured a calibration value for each layer and this can be used to convert our TOT value from counts to MIPs. MIPs are being normalized to the electron runs. Since the measured values from the electron runs are within 10–20% of the value expected by charge injection, hereafter any TOT analysis will refer to

[2] $\phi(x) = \frac{1}{\pi}\int_0^\infty \mathrm{e}^{-s\log(s)-xs}\sin(\pi s)ds$. Where x is the TOT value and $\phi(x)$ gives the probability density for the Landau distribution. The TOT value for the peak value of $\phi(x)$ was recorded as the conversion from μs to MIPs.

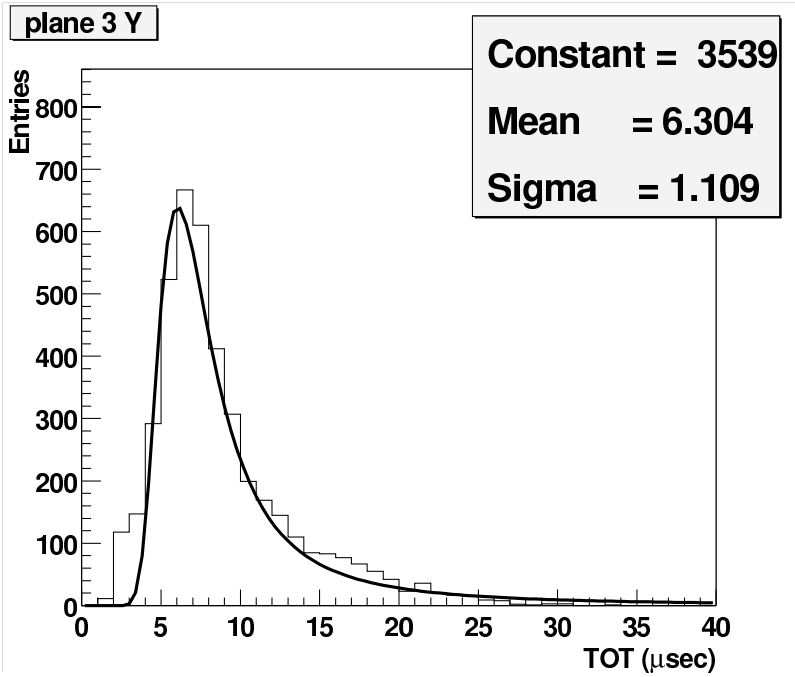

Figure B.15 Distribution showing the TOT for a 20 GeV positron run in one layer. These distributions were used to calculate the calibration constants for each layer of the tracker using a 20 GeV run (run 283) and a 2 GeV positron run (run 360). The mean from the Landau distribution is used as the conversion from μs to MIPs for each layer.

TOT in number of MIPs using the calibrations measured with the electron runs.

B.3.6 Charged Particle Rejection

The first exercise after calibrating the TOT was to see how useful it would be in charged particle rejection. This analysis was done for normal incident particles.

The TOT should be able to accurately tell whether an electron entered the tracker or not. An electron should create hits in all layers as it passes through the tracker. Therefore, the TOT should not be equal to zero for any layer in the tracker. To test this hypothesis we looked at run 360 again, a 2 GeV normal incident positron beam. The raw data from the beam test were processed through the reconstruction program

Table B.6 TOT Calibration

Layer	**Run 283** [μs/MIP]	**Run 360** [μs/MIP]	**average** [μs/MIP]
31	6.2	6.3	6.3
30	6.6	6.0	6.3
29	6.2	5.8	6.0
28	6.2	6.0	6.1
27	6.6	6.7	6.7
26	6.3	6.1	6.2
25	7.7	6.8	7.3
24	5.8	6.1	6.0
23	7.3	7.2	7.3
22	7.0	6.4	6.7
21	7.4	6.9	7.2
20	6.6	6.8	6.7
19	7.2	6.9	7.1
18	8.1	7.4	7.8
17		BAD LAYER	
16	9.0	8.3	8.7
15	8.1	6.9	7.5
14	9.5	8.3	8.9
13	10.0	8.6	9.3
12	8.5	7.3	7.9
11	8.8	7.5	8.2
10	8.0	6.9	7.5

TB_RECON[3]. The reconstruction program reconstructed 91,537 events. This value was used as the number of electrons entering the detector. True, more entered than this, but we are not concerned with events that cannot be reconstructed. Now for the TOT cut, we created an ntuple that contained the TOT value for each layer in each event *and* the TOT value for the layer immediately above that layer (bTOT). This construction makes it possible to cut on the TOT of the layer you are looking at and the TOT of the layer before it. If we require that the bTOT be equal to zero and the TOT be greater than zero in any layer, the number of events that survived

[3]For more information see the TB_RECON web page:
http://www-glast.stanford.edu/cgi-bin/cvsweb-SLAC/~checkout~/tb_recon/doc/centella.html

were 462. The most basic TOT cut rejected 99.5% of the electrons. This same cut could be done by requiring no hits above where the pair-production occurred.

The next exercise was to see how the rejection was affected as we cut on the TOT itself not just the bTOT. In addition to requiring bTOT to be zero we placed minimum values on the TOT itself. So we only accepted events with bTOT = 0 and TOT > *some value*. Figure B.16 shows how the rejection efficiency changed by varying this cut. From this plot we can see that requiring bTOT to be zero and the TOT to be greater than 1.4 MIPs rejects 99.8% of all positrons. This would be an event that had a jump from zero TOT to almost two MIPs in TOT. This is a sign of a photon conversion, discussed below. This rejection capability has only been studied on normal incident positrons into the tracker. This measure of rejection efficiency measurement is a guide to measure true rejection efficiency. To correctly measure efficiency, one needs to really know whether the particle is a charged particle or not. This can only be accomplished through Monte Carlo analysis, at this time the TOT information in the Monte Carlo is not accurate enough for this study.

B.3.7 Position of Photon Conversion

High-energy photons travel through the tracker undetected. The photons can only be detected after they have passed close enough to a nucleus and pair produced, converted into a positron and electron. Lead converters have been placed throughout the tracker to provide a place for this to take place. Every other layer has a lead converter just before it; two layers make up a plane so every plane has a lead converter just above it (except for the bottom three planes that have no lead foils). When the pairs are produced they stay close to each other until they travel through enough material so that multiple scattering can spread them apart. Based on this picture, in a large pitch tracker, one would expect the positron and electron to deposit their energy on the same strip just after the conversion point (vertex) (Figure B.17). Therefore, immediately after the conversion point we expect the TOT to register a value close to two MIPs. As the particles move through the tracker they spread apart and deposit their energy on more than one strip. So, the TOT goes back to one MIP. This is

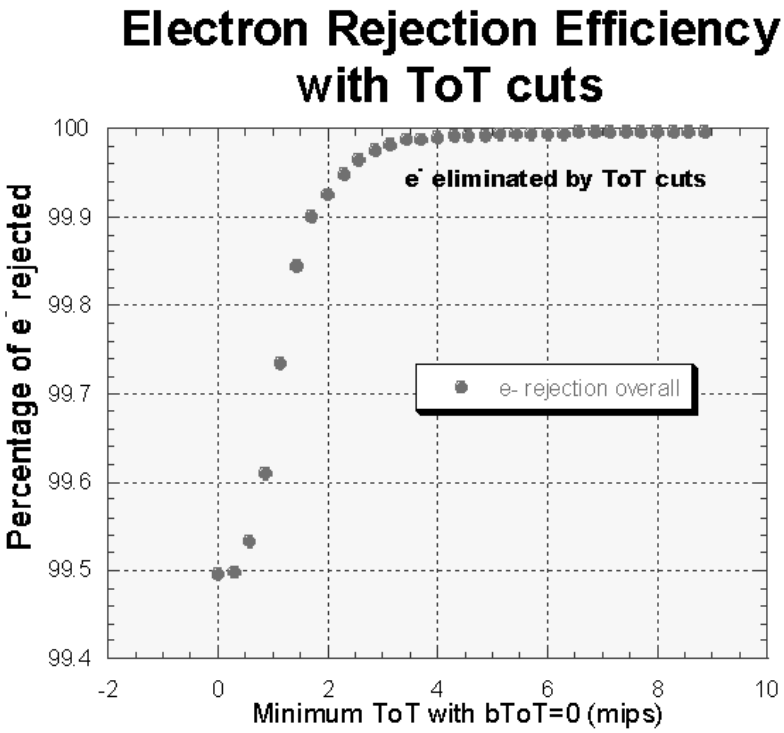

Figure B.16 This plot shows the effectiveness that the TOT can have on rejecting normally incident positrons (or electrons). Similar results were obtained from a 2 GeV positron beam and a 20 GeV positron beam.

what is observed in normal incidence photon runs Figure B.17. These data are from a normal incidence photon run with beam energy of 20 GeV (run 285). This trend was seen in all layers of the tracker for this run, so the TOT could be used to locate a conversion in any layer of the tracker, except the topmost where there is no bTOT information. One may also be able to do a similar analysis looking where the hit patterns show no hits, then one hit, then two hits moving through the tracker.

B.3.8 Position of Photon Conversion: Comparing TOT to Reconstruction

During BTEM analysis the Monte Carlo did not properly calculate the TOT. Therefore, no absolute measure of the TOT reconstructed position can be quoted. However,

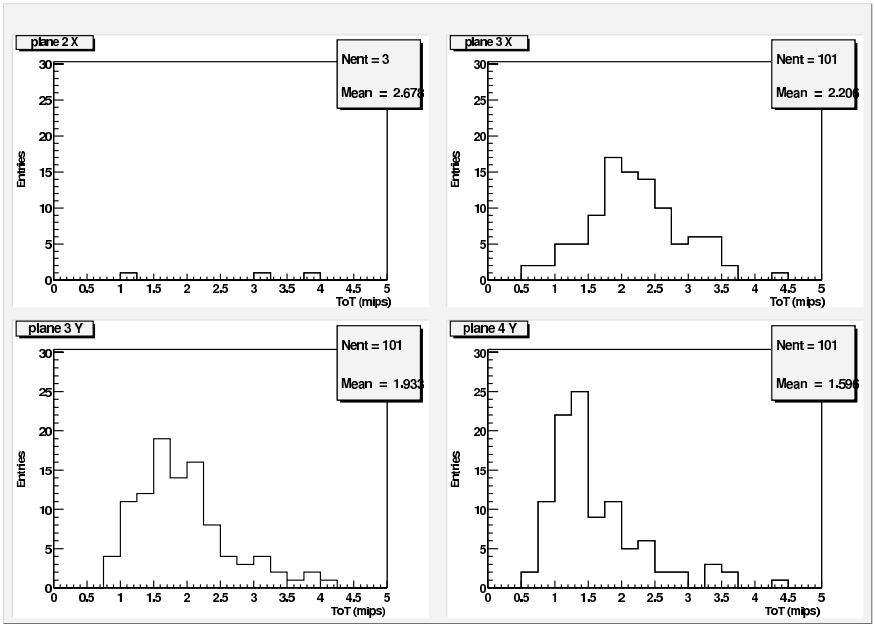

Figure B.17 These distributions show the progression of a normal photon conversion in the tracker. Until the photon pair produces, the TOT value will be zero. Event scanning revealed that the nonzero TOT events here are incorrectly reconstructed. In the layer just after conversion the TOT registers a value close to 2 MIPs. Then as the particles scatter through the tracker the TOT goes to a value closer to that corresponding to one MIP see Figure B.14

the expected photon conversion position using the TOT can be compared to that obtained by the reconstruction program and individual events can be viewed to see if the position of the vertex found using the TOT information is correct. This was done with the BTEM and Balloon flight engineering model (BFEM) data and found good agreement. However, note that we did not have a true particle identification so we cannot be truly quantitative about the results. This will take Monte Carlo analysis to fully quantify.

B.3.9 Analysis of Photon Acceptance

As already stated, the *true* photon acceptance could not be calculated since the TOT information in the Monte Carlo was not correct. However, if we assume that 100%

of all photons are found by the reconstruction program[4] then we can use this as our starting point for photon acceptance. The validity of this assumption will be discussed further in §B.3.10. For this analysis, a normal incident photon run of beam energy 20 GeV was used (run 285). The data from this run were analyzed with the reconstruction program. One layer was looked at, the reconstruction program found 2457 photons that converted above this layer. This is the starting point in the TOT acceptance analysis. The following cut was placed on the data: the TOT before this layer must equal zero (bTOT = 0), and the TOT in this layer must be greater than zero. As discussed earlier, this is a first guess on where a photon converted. After this cut was made, 2155 of the original 2457 events remained. This gives an *acceptance* of $\frac{2155}{2457} = 88\%$. Then, as in the electron rejection studies, the minimum TOT value was increased and the resulting acceptance was graphed (Figure B.18).

When looking at Figure B.18, notice the two different y-axis scales for the two graphs. From this plot we saw that the acceptance started to drop sharply around 1.2 MIPs. When looking for vertex positions we want to look for TOT values close to 2 MIPs, but if a cut was placed too close to 2 than the acceptance would be low, so the TOT value used was 1.4 MIPs. Any hit that occurred on a layer where the plane above had a zero TOT and the layer of the hit had a TOT of > 1.4 MIPs was considered by the TOT to be a photon conversion point. More details of the discrimination between one MIP and 2 MIP TOT events are described in §B.3.11.

B.3.10 Position of Photon Conversion: Comparing TOT to Event Display

Now for the real test of the TOT's ability to find vertices, run the TOT cut described above (bTOT = 0 and TOT > 1.4 MIPs) on a photon run and see how often it is correct. The *true* photon conversion position was detected using an event display looking for evidence of a vertex in the tracks where it appears a photon converted into a positron and electron. More accurate measurements of the *true* conversion point

[4]We Required the reconstruction to find two tracks in both x and y fitted energy > 10 GeV and one vertex. This will not find 100% of all photons, and may find some false photons, see §B.3.10.

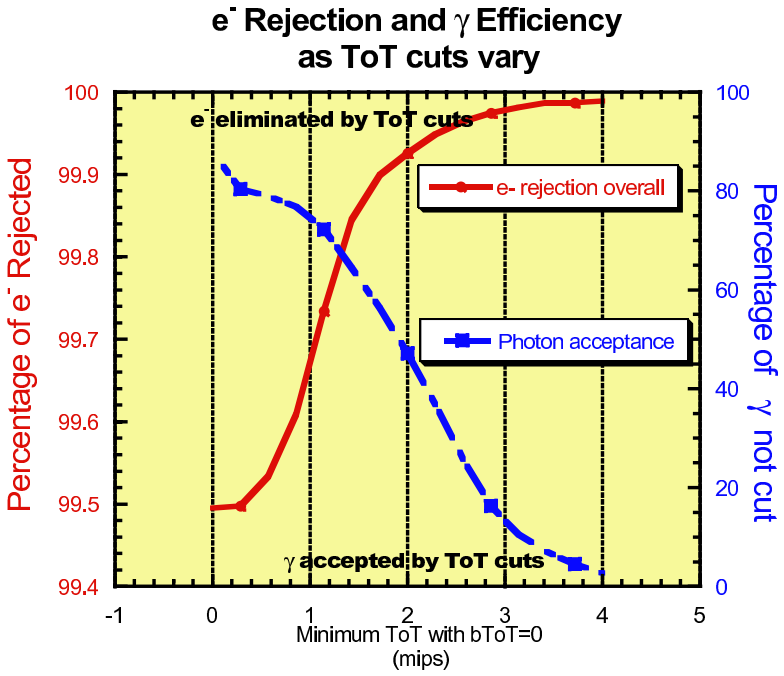

Figure B.18 This figure shows the percentage of electrons rejected with the TOT cut described in the text, rejection scale on the left. The dashed line shows the percentage of photons that were accepted by the TOT cut, acceptance scale on the right. The electron rejection was calculated in a beam of electrons and the photon acceptance was calculated in a beam of photons. To use this information for determining a TOT cut for flight use, the electron rejection curve should be scaled down with the assumed value of the flight signal to background ratio. The expected signal to noise ratio in orbit will be $\sim 10^{-4}$. The ACD will raise the signal to noise to $\sim 10^{-1}$. With the implementation of the TOT cut at 1.4 MIPS, the signal to noise will be raised to $\sim$ 15:1.

are impossible without the fully functional Monte Carlo. Again, a normal incident high-energy photon run was used (run 285). Here only the first 10,000 events were analyzed due to time constraints. The following analysis will refer to only one layer in the tracker, layer 25, in the fourth plane of silicon from the top. However, similar numbers came from looking at layer 9 in the tenth plane from the top.

Of the 10,000 events that were looked at, there were 59 photon conversions directly above layer 25, found by scanning event displays. Using only the TOT algorithm

Table B.7 Comparison of algorithms used to find the location of the photo-conversion point

Algorithm	**Total events detected by algorithm**	**Events determined to be real photons by visual scan**	**Events determined not to be single photons by visual scan**
Recon	75	57	18
TOT	60	50	10
Require Both TOT + Recon	48	48	0

for finding vertices (bTOT = 0 and TOT > 1.4 MIPs) we found 50 of them. The TOT algorithm found 10 other events that were not correct. Therefore, the TOT algorithm was correct 83% of the time, and the TOT algorithm found 85% of all photon conversions.

Now to get an idea of the power of this tool, we compared the efficiency of the TOT algorithm to the reconstruction program. Keep in mind; all of these results are for normal incident photons in the tracker. Of the 59 true photon conversions the reconstruction found 57. However, the reconstruction found 18 other events that were not correct photon conversions. Therefore, reconstruction was correct 76% of the time, and reconstruction found 97% of all photon conversions.

If we only took the events that the TOT algorithm *and* reconstruction agreed on (48 total) then 100% of all events found were correct photon conversions; and 81% of all photon conversions would have been found. Therefore, this is the strength of the TOT algorithm. The TOT can be used to reduce the number of incorrect reconstructions, at the cost of slightly lower reconstruction efficiency. See Table B.3.10 for a comparison of the values found by the two different algorithms of determining pair production location. Poorly reconstructed vertices may contribute to errors on the measurement of the direction of the incoming photon.

B.3.11 One and Two MIP Discrimination

The strength of the TOT algorithm relies on the ability to tell the difference between an event that deposited one MIP in a layer or two.

Figure B.19 shows a distribution of TOT values in one layer for photons produced from a 20 GeV beam. Events were chosen that either converted three planes above the layer observed, or immediately before the layer observed. The TOT values should correspond to one or two MIPs, respectively. The filled circles show the distribution of both events. The dashed histogram shows the distribution of the one MIP events. The solid histogram shows the difference between all events and the dashed histogram and corresponds to the two MIP events. From scanning with the event display the two MIP events that have TOT values $\lesssim 50$ counts, we found that they correspond to three types of events. First, nearly half of the events have hits in two strips in the layer after conversion, therefore, the TOT is lower than a value corresponding to two MIPs since the energy was shared between two strips. Second, the electron and positron can deposit most of their energy onto one strip, but enough can be shared by other strips to lower the TOT, but not enough to register a hit. Third, in some events only one of the two particles (electron or positron) register a hit, and the other particle may be missed completely. Therefore, with improvements in the algorithm we can still increase the significance of the separation between both types of events.

This sets design constraints that will be used in the design of the TOT concerning the amount of resolution in timing that needs to be designed into the chip, and tells where a good place to make a TOT cut to distinguish between one and two MIP events.

B.3.12 Conclusions

The Time over Threshold, TOT, is a useful tool built into the GLAST tracker. The TOT was initially designed to give more ability to reject background events from particles coming out of the calorimeter. However, we found the TOT is a useful tool in rejecting normal incident electrons, up to 99.8%. Then the properties of the TOT were explored to see if TOT values could be used as an aid to reconstruct photon events. We found that the TOT in conjunction with reconstruction can eliminate all false photon conversions, while keeping the efficiency greater than 80%.

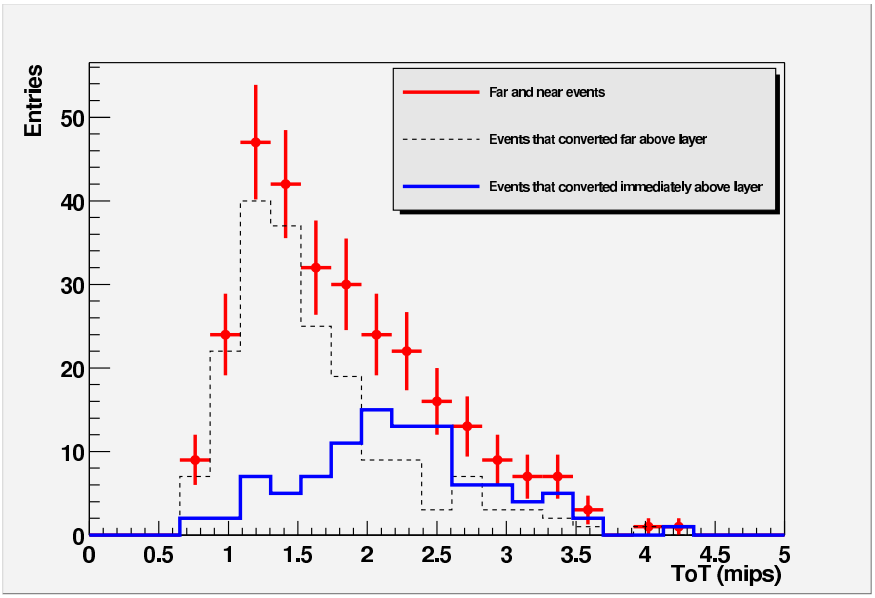

Figure B.19 TOT distributions in one layer for events converting far from the layer (dashed line), all events (data points), and the difference between these two corresponding to events converting immediately before the layer (solid line).

B.4 GLAST BTEM Microdischarge Studies

Introduction

The objective for this exercise was to analyze the BTEM data to see if evidence of microdischarges could be seen as the bias voltage was increased. Runs 81 through 85 were selected; these runs were 170.5 mV threshold, zero degree positron runs, that were operated at different bias voltages, from 150 V to 60 V, respectively, see Table B.8. Only noisy strips that had strip occupancies greater than 0.1% were analyzed.

In run 81 (150 V) we looked at the number of hits in each strip in each layer to determine strips that had a large amount of hits above the baseline (occupancy greater than 0.1%). After determining the noisy strips, using this method, we looked at the same strips and layers in the remaining four runs. From this data, we could obtain the amount of noise above the baseline in the noisy strips and divide this value

Table B.8 Bias Voltages for the BTEM Runs

Run Number	Bias Voltage [V]
81	150
82	120
83	100
84	80
85	60

by the total number of hits in that layer. This normalized value was then analyzed at the five different voltages to see if any trends appeared. The noise is expected to increase as the square root of voltage, since

$$\text{leakage current} \propto \text{width depth} \tag{B.1}$$

Where

$$\text{width} \propto \sqrt{\text{voltage}} \tag{B.2}$$

If, in addition to this growth, an exponential or very sharp increase is seen then this is evidence of microdischarges. (Note: we cannot quantify how much current is actually in a given strip)

After the beam test, the bias voltage was further increased up to 200 V. No evidence of microdischarges was seen in any of these observations except in the 200 V data.

Finding Noisy Strips

In order to track the effect of bias voltage on leaky strips the leaky strips needed to be located. Run 81 was used for this purpose. Run 81 had the highest bias voltage used in the beam test, 150 V. Therefore, if leaky strips occur due to breakdown at higher bias voltages, they should be present in run 81.

Each layer in run 81 was analyzed. The number of hits per strip vs. strip was plotted. Then, leaky strips were located.

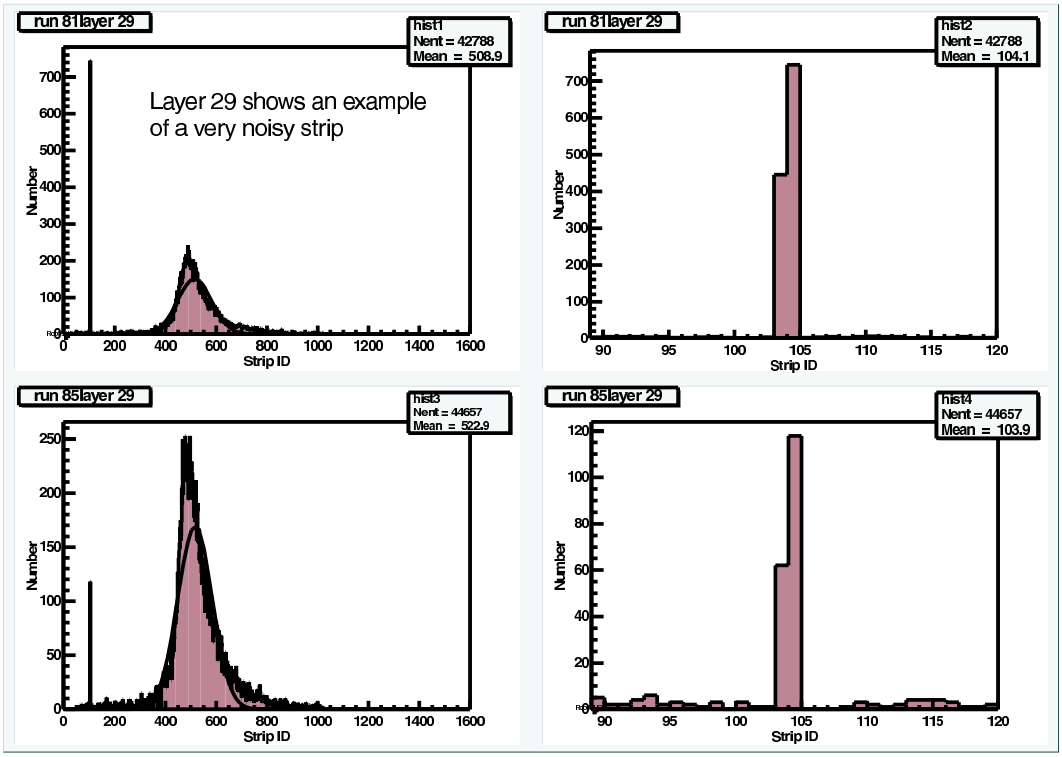

Figure B.20 This figure shows a Large Leaky Strip. The top two graphs are from the 150 V run, the bottom two, from 60 V run. The leftmost plots show all strips to show the picture of the beam, the rightmost plots are zoomed in on the leaky strips 103-104.

As the leaky strips were being tabulated, they were broken down into three categories: Large leaky (Figure B.20), where the noise above the baseline is higher than the actual highest signal from where the beam went through the detector; Medium Leaky (Figure B.21); and Small leaky (Figure B.21), where the noise is less than 100 above the baseline. All categories have occupancy at 150 V greater than 0.1% (Figure B.22)

For each of the leaky strips that were analyzed, 19 total, the normalized noise was calculated.

$$\text{normalized noise} = \frac{\text{noise} - \text{baseline}}{\text{number of hits in layer for all events}} \tag{B.3}$$

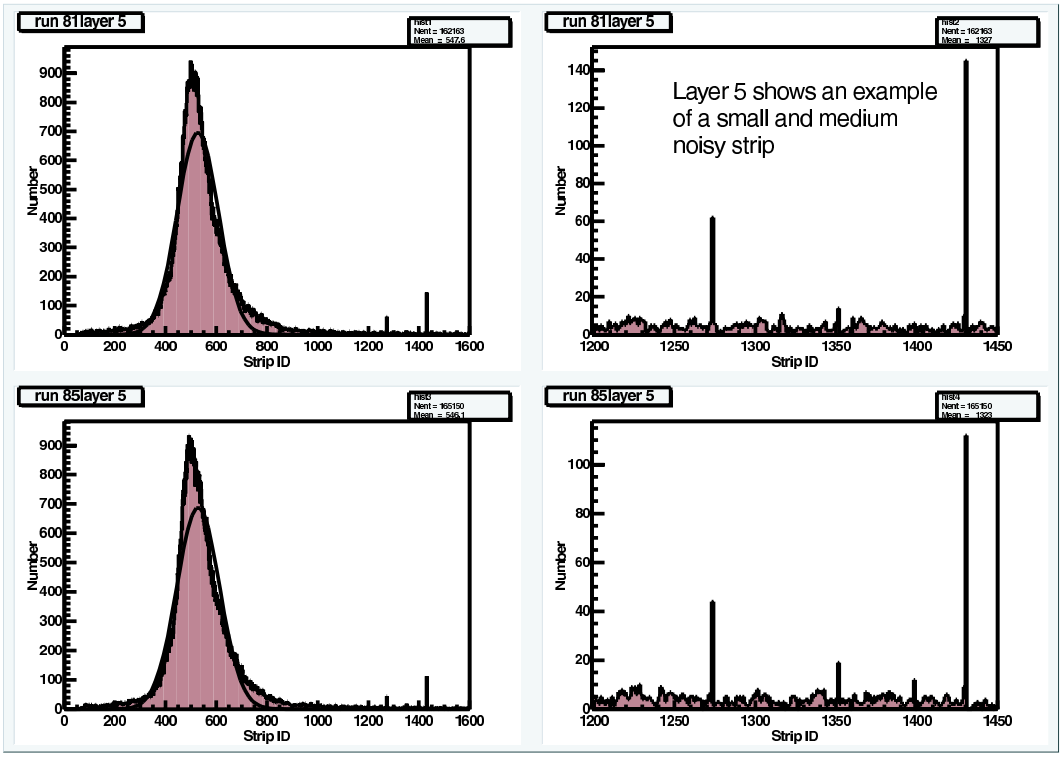

Figure B.21 This figure shows a Medium Leaky strip (1430) and a Small Leaky Strip (1273). The layout of the four plots is the same as in Figure B.20.

The average of the normalized noise for each category of strip (Large, Medium, Small) was plotted as a function of voltage (Figure B.23). And the average of this value for all strips regardless of category was also plotted (Figure B.23).

From these plots we can see the noise above baseline grows almost linearly with voltage, but there is no evidence of a large jump or an exponential increase. No new noisy strips appeared as the bias voltage was increased.

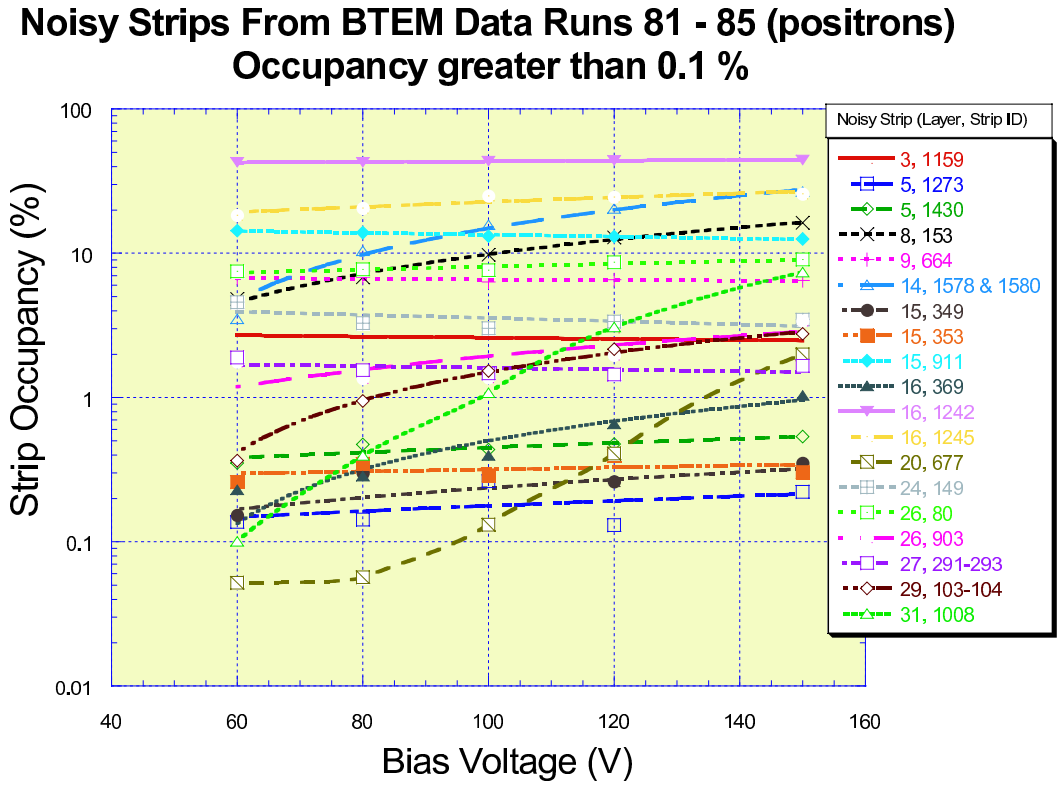

Figure B.22 Showing the occupancy of each strip analyzed as a function of bias voltage.

Occupancy

The occupancy of the noisy strips as a function of Bias voltage was also analyzed (Figure B.22).

$$\text{strip occupancy} = \frac{\text{number of hits in the strip}}{\text{total number of events in run}} \tag{B.4}$$

We did this for each of the nineteen leaky strips that were used throughout this analysis. This results in looking at all noisy strips in the detector that have occupancy at 150 V of greater than 0.1%. The noisiest strip (layer 16 strip 1242) has occupancy of 45% at 150 V (Figure B.22).

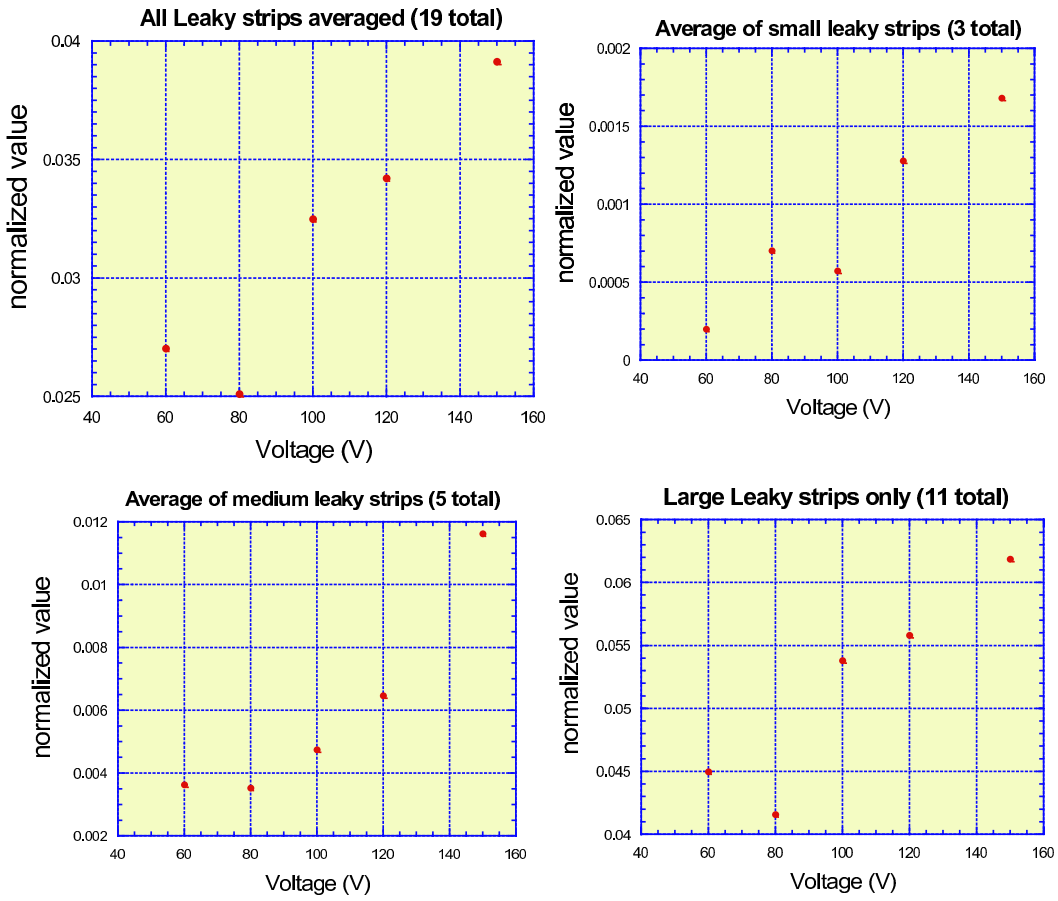

Figure B.23 The normalized value of noise as a function of voltage. The dominant contribution to the shape of the overall average comes from the large leaky strips, since 11 of the 19 are in this category. I do not understand why there is a dip at 80 V; however, I am not looking for quantified effects, only trends in the distribution.

Off Line Measurements

After the beam test, the bias voltage was increased up to 200 V. These data were analyzed to see if they contained any evidence of microdischarges. Typical results can be seen in Figure B.24. Figure B.24 shows the hits per strip vs. strip for six different bias voltages (100 - 200 V) for layer 16. One can see that at 200 V new noisy strips appear. A total of five new noisy strips were found in all layers when the bias voltage was increased from 180 to 200 V.

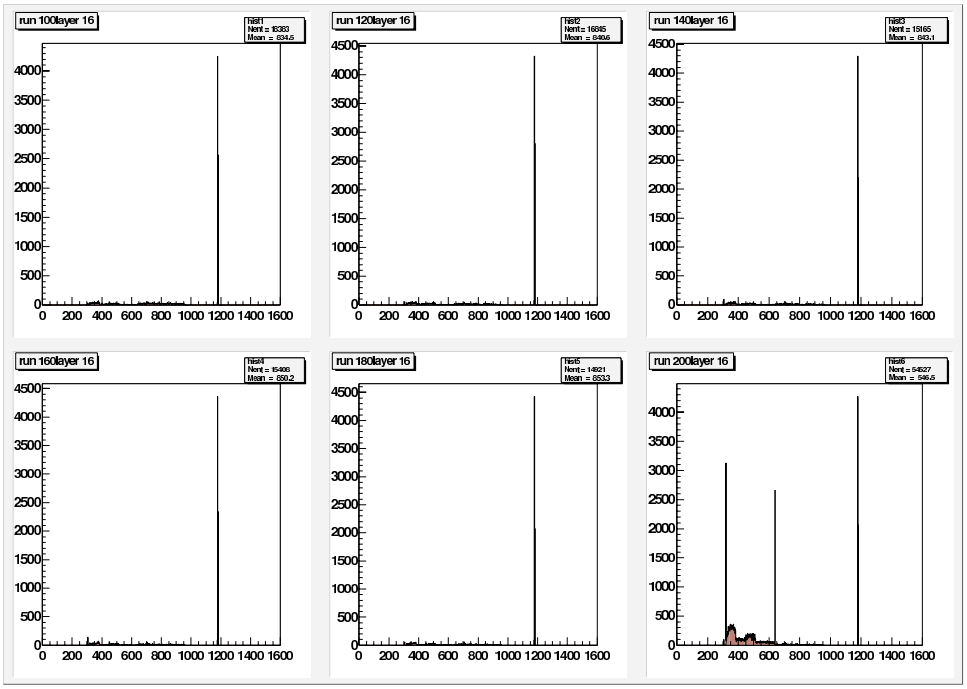

Figure B.24 The hits per strip vs. strip for layer 16 as the bias voltage was varied from 100 V to 200 V in 20 V increments. The last histogram shows the appearance of new noisy strips that did not show up until the bias voltage was 200 V.

Conclusions

The noise in the leaky strips increases with voltage, but there is no evidence of a large jump at the bias voltages used in the beam test. There is no exponential run-away or increase in the number of leaky channels either; there is no evidence of microdischarge effects. The only evidence of microdischarges occurred after the beam test when the bias voltage was increased to 200 V. At 200 V five new noisy strips appeared. The largest occupancy value seen is 45%, with 14 of the 19 strips falling below 10% occupancy at 150 V, for a nominal threshold of 170.5 mV.

Appendix C

List of Abbreviations

Abbreviation	Definition
ACD	Anti-Coincidence Detector
ADC	Analog to Digital Converter
AGN	Active Galactic Nuclei
ASM	All Sky Monitor aboard the RXTE
BATSE	Burst And Transient Source Experiment
BHC	Black Hole Candidate
BTEM	GLAST Beam Test Engineering Model
CR	Cosmic Ray
EDIE	Energy Dependent Instrumental Effect of the USA instrument
EGRET	Energetic Gamma-Ray Experiment Telescope
FOM	Figure of Merit
FWHM	Full Width at Half Maximum
GBM	Glast Burst Monitor
GLAST	Gamma-Ray Large Area Space Telescope
GPS	Global Positioning System
GRB	Gamma Ray Burst
HEXTE	High Energy X-ray Timing Experiment
HFQPO	High-Frequency Quasi Periodic Oscillation

Abbreviation	Definition
HID	Hardness vs. Intensity Diagram
HMXB	High-Mass X-ray Binary
HS	High/Soft State
HWHM	Half Width at Half Maximum
INTEGRAL	International Gamma-Ray Astrophysics Laboratory
IS	Intermediate State
ISCO	Innermost Stable Circular Orbit
ISM	Interstellar Medium
JD	Julian Day
LAT	Large Area Telescope
LFQPO	Low-Frequency Quasi Periodic Oscillation
LMXB	Low-Mass X-ray Binary
LS	Low/Hard State
MIP	Minimum Ionizing Particle
MJD	Modified Julian Day
MSGC	Micro-Strip Gas Chamber
NS	Neutron Star(s)
PCA	Proportional Counter Array aboard the RXTE
PCU	Proportional Counter Unit (five PCUs in the PCA)
PRN	Pseudo Random Noise
PSD	Power Spectral Density distribution
QPO	Quasi-Periodic Oscillation
QS	Quiescent State
RMS	Root Mean Square
RXTE	Rossi X-ray Timing Explorer space telescope
SNR	Supernova Remnant
SSD	Silicon Strip Detector
SUSY	Super Symmetry
SV	Space Vehicle or satellite

Abbreviation	**Definition**
SXT	Soft X-ray Transient
TAI	Temps Atomiqu International (International Atomic Time)
TCB	Barycentric Coordinate Time
TCG	Geocentric Coordinate Time
TDB	Barycentric Dynamical Time
TDT	Terrestrial Dynamical Time
TL	Transition Layer
TOO	Target Of Oppurtunity observation
TOT	Time Over Threshold
USA	Unconventional Stellar Aspect space telescope
UT	Universal Time
UTC	Coordinated Universal Time
VHS	Very High State

Table C.1: List of Abbreviations

Bibliography

Abramowicz, M. A., Kluźniak, W., & Lasota, J.-P. 2002, A&A, 396, L31

Alford, M., Rajagopal, K., & Wilczek, F. 1998, Physics Letters B, 422, 247

Allport, P., et al. 2001, Nuclear Instruments and Methods in Physics Research A, 466, 376

Alpar, M. A., Cheng, A. F., Ruderman, M. A., & Shaham, J. 1982, Nature, 300, 728

Armitage, P. J., & Livio, M. 2000, ApJ, 532, 540

Ashman, K. M. 1992, PASP, 104, 1109

Atwood, E., et al. 2001, Nuclear Instruments and Methods in Physics Research A, 457, 126

Atwood, W. B. 1994, Nucl. Instrum. Meth., A342, 302

Augusteijn, T., Kuulkers, E., & van Kerkwijk, M. H. 2001, A&A, 375, 447

Babak, S. V., & Grishchuk, L. P. 2002, gr-qc/0209006

Belczynski, K., Bulik, T., & Kalogera, V. 2002, ApJ, 571, L147

Bellazzini, R., et al. 2003, in Polarimetry in Astronomy. Edited by Silvano Fineschi . Proceedings of the SPIE, Volume 4843, pp. 372-382 (2003)., 372

Bildsten, L. 2000, in Rossi2000: Astrophysics with the Rossi X-ray Timing Explorer. March 22-24, 2000 at NASA's Goddard Space Flight Center, Greenbelt, MD USA, p.E65

Blackburn, J. K., Greene, E. A., & Pence, W. 1993, Bulletin of the American Astronomical Society, 25, 816

Blandford, R. D., & Rees, M. J. 1978, in Pittsburgh Conference on BL Lac Objects, Pittsburgh, Pa., April 24-26, 1978, Proceedings. (A79-30026 11-90) Pittsburgh, Pa., University of Pittsburgh, 1978, p. 328-341; Discussion, p. 341-347. NATO-supported research, 328

Borozdin, K., Revnivtsev, M., Trudolyubov, S., Shrader, C., & Titarchuk, L. 1999, ApJ, 517, 367

Bradt, H. V., Rothschild, R. E., & Swank, J. H. 1993, Astronomy and Astrophysics Suppl. Series, 97, 355

Brandt, S., Castro-Tirado, A. J., Lund, N., Dremin, V., Lapshov, I., & Syunyaev, R. 1992, A&A, 262, L15

Cannizzo, J. K., Chen, W., & Livio, M. 1995, ApJ, 454, 880

Catanese, M., et al. 1997, ApJ, 487, L143

Chen, V. 2000, in Proc. 4th Intl. Symposium on Dev. and App. of Semiconductor Tracking Detectors

Chiang, J., & Romani, R. W. 1992, in The Compton Observatory Science Workshop, 237

Chiang, J., & Romani, R. W. 1994, ApJ, 436, 754

Christian, D. J., & Swank, J. H. 1997, ApJS, 109, 177

Clayton, D. D. 1968, Principles of Stellar Evolution and Nucleosynthesis (New York, NY: McGraw-Hill)

Cooke, B. A., & Ponman, T. J. 1991, A&A, 244, 358

Cornelisse, R., et al. 2002, A&A, 392, 885

Cumming, A., & Bildsten, L. 2001, ApJ, 559, L127

Dana, P. H. 1994, The Geographer's Craft Project, Department of Geography, The University of Colorado at Boulder

Dieters, S. W., et al. 2000, ApJ, 538, 307

do Couto e Silva, E. d., et al. 2001, Nuclear Instruments and Methods in Physics Research A, 474, 19

Done, C. 2002, Philosophical Transactions of the Royal Society (Series A: Mathematical, Physical, and Engineering Sciences), 251, 3246

Done, C., & Gierliński, M. 2003, MNRAS, 342, 1041

Dorman, B., & Arnaud, K. A. 2001, in ASP Conf. Ser. 238: Astronomical Data Analysis Software and Systems X, Vol. 10, 415

Dotani, T., et al. 2003, in X-Ray and Gamma-Ray Telescopes and Instruments for Astronomy. Edited by Joachim E. Truemper, Harvey D. Tananbaum. Proceedings of the SPIE, Volume 4851, pp. 1071-1079 (2003)., 1071

Filippenko, A. V., & Chornock, R. 2001, IAU Circ., 7644, 2

Focke, W. B. 1998, Ph.D. thesis, University of Maryland, Colleg Park

Fox, D. D. 2003, Personal Communication

Fox, D. W., et al. 2001, MNRAS, 321, 776

Gaensler, B. M., Slane, P. O., Gotthelf, E. V., & Vasisht, G. 2001, ApJ, 559, 963

Galloway, D. D. 2003, Personal Communication

Galloway, D. K., Psaltis, D., Chakrabarty, D., & Muno, M. 2003, ApJ, in press, astro-ph/0208464

Gavriil, F. P., & Kaspi, V. M. 2002, ApJ, 567, 1067

Gehrels, N., & Michelson, P. 1999, Astroparticle Physics, 11, 277

Geldzahler, B. J., Fomalont, E. B., & Bradshaw, C. F. 1999, Bulletin of the American Astronomical Society, 31, 897

Gierliński, M., & Done, C. 2002, MNRAS, 331, L47

Glendenning, N. K., ed. 1997, Compact stars. Nuclear physics, particle physics, and general relativity

Goldreich, P., & Julian, W. H. 1969, ApJ, 157, 869

Greiner, J., Cuby, J. G., & McCaughrean, M. J. 2001, Nature, 414, 522

Guerriero, R., et al. 1997, American Astronomical Society Meeting, 191, 0

Guerriero, R., et al. 1999, MNRAS, 307, 179

Haberl, F., & Titarchuk, L. 1995, A&A, 299, 414

Hanisch, R. J., Farris, A., Greisen, E. W., Pence, W. D., Schlesinger, B. M., Teuben, P. J., Thompson, R. W., & Warnock, A. 2001, A&A, 376, 359

Hannestad, S., & Raffelt, G. G. 2002, Physical Review Letters, 88, 71301

Hansen, C. J., & van Horn, H. M. 1975, ApJ, 195, 735

Harding, A. K. 1981, ApJ, 245, 267

Harding, A. K., & Muslimov, A. G. 2001, ApJ, 556, 987

Herrero, A., Kudritzki, R. P., Gabler, R., Vilchez, J. M., & Gabler, A. 1995, A&A, 297, 556

Hjellming, R. M., et al. 1999, ApJ, 514, 383

Holloway, N. J. 1973, Nature Physical Science, 246, 6

Homan, J., Wijnands, R., van der Klis, M., Belloni, T., van Paradijs, J., Klein-Wolt, M., Fender, R., & Méndez, M. 2001, ApJS, 132, 377

Hunter, S. D., et al. 1997, ApJ, 481, 205

Iaria, R., Di Salvo, T., Burderi, L., & Robba, N. R. 2001, ApJ, 548, 883

Iben, I. 1975, ApJ, 196, 549

Jahoda, K., Swank, J. H., Giles, A. B., Stark, M. J., Strohmayer, T., Zhang, W., & Morgan, E. H. 1996, in Proc. SPIE, ed. O. H. Siegmund & M. A. Gummin, Vol. 2808, 59

Janka, H.-T., Eberl, T., Ruffert, M., & Fryer, C. L. 1999, ApJ, 527, L39

Jones, C., Forman, W., Tananbaum, H., & Turner, M. J. L. 1976, ApJ, 210, L9

Körding, E., Falcke, H., & Markoff, S. 2002, A&A, 382, L13

Kamae, T. 2002, in American Physical Society, April Meeting, Jointly Sponsored with the High Energy Astrophysics Division (HEAD) of the American Astronomical Society April 20 - 23, 2002 Albuquerque Convention Center Albuquerque, New Mexico Meeting ID: APR02, abstract #2A3.004, A3004

King, A. R., & Ritter, H. 1998, MNRAS, 293, L42

Knight, J. 2003, Nature, 422, 554

Kotthaus, R., Buschhorn, G., Pugachev, D., Shooshtari, H., & They, J. 1999, in Proc. SPIE Vol. 3764, p. 49-60, Ultraviolet and X-Ray Detection, Spectroscopy, and Polarimetry III, Silvano Fineschi; Bruce E. Woodgate; Randy A. Kimble; Eds., 49

Kowalski, M. P., Cruddace, R. G., Snyder, W. A., Fritz, G. G., Ulmer, M. P., & Fenimore, E. E. 1993, ApJ, 412, 489

Kuulkers, D. E. 2003, Personal Communication

Kuulkers, E., et al. 2002, A&A, 382, 503

Kuulkers, E., Parmar, A. N., Kitamoto, S., Cominsky, L. R., & Sood, R. K. 1997, MNRAS, 291, 81

Kuulkers, E., & van der Klis, M. 2000, A&A, 356, L45

Kuulkers, E., van der Klis, M., & Parmar, A. N. 1997, ApJ, 474, L47

Kuulkers, E., Wijnands, R., Belloni, T., Mendez, M., van der Klis, M., & van Paradijs, J. 1998, ApJ, 494, 753

Lewin, W. H. G., & den Heuvel, E. P. J. V., ed. 1983, Accretion Driven X-ray sources (Cambridge, UK: Cambridge University Press)

Lewin, W. H. G., van Paradijs, J., & Taam, R. E. 1993, Space Science Reviews, 62

Lewin, W. H. G., van Paradijs, J., & Taam, R. E. 1995, in X-ray Binaries, ed. W. H. G. Lewin, J. van Paradijs, & E. P. J. van den Heuvel (Cambridge University)

Lewin, W. H. G., van Paradijs, J., & van den Heuvel, E. P. J. 1995, X-ray binaries (Cambridge Astrophysics Series, Cambridge, MA: Cambridge University Press, —c1995, edited by Lewin, Walter H.G.; Van Paradijs, Jan; Van den Heuvel, Edward P.J.)

Lumb, D. H., Finoguenov, A., Saxton, R., Aschenbach, B., Gondoin, P., Kirsch, M., & Stewart, I. M. 2003, in X-Ray and Gamma-Ray Telescopes and Instruments for Astronomy. Edited by Joachim E. Truemper, Harvey D. Tananbaum. Proceedings of the SPIE, Volume 4851, pp. 255-263 (2003)., 255

Magdziarz, P., & Zdziarski, A. A. 1995, MNRAS, 273, 837

Marshall, H. L., et al. 2001, AJ, 122, 21

Mazur, P. O., & Mottola, E. 2002, in American Physical Society, April Meeting, Jointly Sponsored with the High Energy Astrophysics Division (HEAD) of the American Astronomical Society April 20 - 23, 2002 Albuquerque Convention Center Albuquerque, New Mexico Meeting ID: APR02, abstract #I12.011, 12011, gr-qc/0109035

McClintock, J. E., et al. 2001, ApJ, 555, 477

McConnell, M. L., Ledoux, J., Macri, J. R., & Ryan, J. M. 2003, in X-Ray and Gamma-Ray Telescopes and Instruments for Astronomy. Edited by Joachim E. Truemper, Harvey D. Tananbaum. Proceedings of the SPIE, Volume 4851, pp. 1382-1393 (2003)., 1382

Meyer, F., Liu, B., & Meyer-Hofmeister, E. 2001, in Black Holes in Binaries and Galactic Nuclei, 200

Meyer-Hofmeister, E., & Meyer, F. 2001, A&A, 372, 508

Michelson, P. F. 1996, in Proc. SPIE Vol. 2806, p. 31-40, Gamma-Ray and Cosmic-Ray Detectors, Techniques, and Missions, Brian D. Ramsey; Thomas A. Parnell; Eds., 31

Mignani, R. P., De Luca, A., Caraveo, P. A., & Mirabel, I. F. 2002, A&A, 386, 487

Mitsuda, K., et al. 1984, PASJ, 36, 741

Muno, M. P., Chakrabarty, D., Galloway, D. K., & Psaltis, D. 2002, ApJ, 580, 1048

Muno, M. P., Remillard, R. A., & Chakrabarty, D. 2001, American Astronomical Society Meeting, 199, 0

Narayan, R., & Heyl, J. S. 2002, ApJ, 574, L139

Nath, N. R., Strohmayer, T. E., & Swank, J. H. 2002, ApJ, 564, 353

Nikolaou, M. 2000, Master's thesis, Stockholm Royal Institute of Technology

O'Neill, P. M., Kuulkers, E., Sood, R. K., & van der Klis, M. 2002, MNRAS, 336, 217

Oosterbroek, T., Parmar, A. N., Kuulkers, E., Belloni, T., van der Klis, M., Frontera, F., & Santangelo, A. 1998, A&A, 340, 431

Orosz, J. A., et al. 2002, ApJ, 568, 845

Orosz, J. A., & Kuulkers, E. 1999, MNRAS, 305, 132

Paciesas, W. S., et al. 1989, in EUV, X-ray, and gamma-ray instrumentation for astronomy and atomic physics; Proceedings of the Meeting, San Diego, CA, Aug. 7-11, 1989 (A90-50251 23-35). Bellingham, WA, Society of Photo-Optical Instrumentation Engineers, 1989, p. 156-164., 156

Paczynski, B. 1983, ApJ, 264, 282

Paczynski, B. 1998, ApJ, 494, L45

Parmar, A. N., Stella, L., & White, N. E. 1986, ApJ, 304, 664

Parmar, A. N., Winkler, C., Barr, P., Hansson, L., Kuulkers, E., Much, R., & Orr, A. 2003, in X-Ray and Gamma-Ray Telescopes and Instruments for Astronomy. Edited by Joachim E. Truemper, Harvey D. Tananbaum. Proceedings of the SPIE, Volume 4851, pp. 1104-1112 (2003)., 1104

Peebles, P. J. E. 2002, astro-ph/0209403

Podsiadlowski, P., Rappaport, S., & Han, Z. 2003, MNRAS, 341, 385

Rapp, R., Schäfer, T., Shuryak, E., & Velkovsky, M. 1998, Physical Review Letters, 81, 53

Ray, P. S., et al. 2001, in AIP Conference Proceedings, Vol. 599, X-ray Astronomy 1999 – Stellar Endpoints, AGN, and the Diffuse Background, ed. G. Malaguti, G. Palumbo, & N. White (Melville, New York: AIP), 336

Ray, P. S., et al. 2003, AAS/High Energy Astrophysics Division, 35, 0

Reilly, K. T. 2002, Ph.D. thesis, Stanford University

R.N.Ogley, J. B. B., ed. 1998, Towards 4U 1630-47: a black-hole soft X-ray transient odyssey, Vol. 42 (NewAR), astro-ph/9807269 v2

Romani, R. W. 1996, ApJ, 470, 469

Rutledge, R. E., Bildsten, L., Brown, E. F., Pavlov, G. G., & Zavlin, V. E. 2000, ApJ, 529, 985

Rutledge, R. E., Bildsten, L., Brown, E. F., Pavlov, G. G., & Zavlin, V. E. 2001, ApJ, 559, 1054

RXTE Team. 1995, Appendix f: The xte technical appendix, Technical appendix to the XTE NRA

Sadrozinski, H. F. W. 2001, Nucl. Instrum. Meth., A466, 292

Saz Parkinson, P. M. 2003, Ph.D. thesis, Stanford Universtiy, In Press

Schmutz, W., Geballe, T. R., & Schild, H. 1996, A&A, 311, L25

Seidelmann, P. K., Guinot, B., & Dogget, L. E. 1992, Explanatory Supplement to the Astronomical Almanac (Mill Valley, California: University Science Books)

Seon, K., Min, K., Yoshida, K., Makino, F., Lewin, W. H. G., van der Klis, M., & van Paradijs, J. 1997, ApJ, 479, 398

Shabad, G. 2000, Ph.D. thesis, Stanford Universtiy

Shahbaz, T., & Kuulkers, E. 1998, MNRAS, 295, L1

Shrader, C. R., & Titarchuk, L. 1999, ApJ, 521, L121

Shu, F. H. 1982, The Physical Universe (Sausalito, California: University Science Books)

Singh, N. S., Naik, S., Paul, B., Agrawal, P. C., Rao, A. R., & Singh, K. Y. 2002, A&A, 392, 161

Spitkovsky, A., Levin, Y., & Ushomirsky, G. 2002, ApJ, 566, 1018

Stahle, C. K., et al. 1999, in Proc. SPIE Vol. 3765, p. 128-136, EUV, X-Ray, and Gamma-Ray Instrumentation for Astronomy X, Oswald H. Siegmund; Kathryn A. Flanagan; Eds., 128

Strohmayer, T., & Bildsten, L. 2003, in Compact Stellar X-ray Sources, ed. W. H. G. Lewin & M. van der Klis (Cambridge University Press), in press astro-ph/0301544

Strohmayer, T. E., & Brown, E. F. 2002, ApJ, 566, 1045

Strohmayer, T. E., & Markwardt, C. B. 1999, ApJ, 516, L81

Sunyaev, R., & Revnivtsev, M. 2000, A&A, 358, 617

Swank, J. H., Becker, R. H., Boldt, E. A., Holt, S. S., Pravdo, S. H., & Serlemitsos, P. J. 1977, ApJ, 212, L73

Tanihata, C., et al. 1999, in Proc. SPIE Vol. 3765, p. 645-663, EUV, X-Ray, and Gamma-Ray Instrumentation for Astronomy X, Oswald H. Siegmund; Kathryn A. Flanagan; Eds., 645

Tennant, A. F., Fabian, A. C., & Shafer, R. A. 1986, MNRAS, 219, 871

Thompson, C., & Duncan, R. C. 1995, MNRAS, 275, 255

Titarchuk, L. 1994, ApJ, 434, 570

Titarchuk, L., Mastichiadis, A., & Kylafis, N. D. 1997, ApJ, 487, 834

Titarchuk, L., & Shaposhnikov, N. 2002, ApJ, 570, L25

Tomsick, J. A., & Kaaret, P. 2000, ApJ, 537, 448

Tomsick, J. A., Lapshov, I., & Kaaret, P. 1998, ApJ, 494, 747

Tournear, D. 2001, Nuclear Instruments and Methods in Physics Research A, 473, 61

Trimble, V. 1987, ARA&A, 25, 425

Trudolyubov, S. P., Borozdin, K. N., & Priedhorsky, W. C. 2001, MNRAS, 322, 309

Ubertini, P., Bazzano, A., Cocchi, M., Natalucci, L., Heise, J., Muller, J. M., & in 't Zand, J. J. M. 1999, ApJ, 514, L27

Ullio, P., Bergström, L., Edsjö, J., & Lacey, C. 2002, Phys. Rev. D, 66, 123502

van der Klis, M. 2000, ARA&A, 38, 717

van Paradijs, J., & White, N. 1995, ApJ, 447, L33

van Paradijs, J. A. 2001, in Black Holes in Binaries and Galactic Nuclei, 316

von Toerne, E., et al. 2001, Nuclear Instruments and Methods in Physics Research A, 473, 17

Wagner, R. M., Foltz, C. B., Shahbaz, T., Casares, J., Charles, P. A., Starrfield, S. G., & Hewett, P. 2001, ApJ, 556, 42

Weiler, K., ed. 2003, Supernovae and Gamma-Ray Bursters (Heidelberg, Germany: Sprinter-Verlag)

Wen, H. C. 1997, Ph.D. thesis, Stanford Universtiy

Wheeler, J. C., & Harkness, R. P. 1990, Reports of Progress in Physics, 53, 1467

White, N. E., & Tananbaum, H. D. 2003, in X-Ray and Gamma-Ray Telescopes and Instruments for Astronomy. Edited by Joachim E. Truemper, Harvey D. Tananbaum. Proceedings of the SPIE, Volume 4851, pp. 293-303 (2003)., 293

Wijnands, R., Muno, M. P., Miller, J. M., Franco, L. ., Strohmayer, T., Galloway, D., & Chakrabarty, D. 2002, ApJ, 566, 1060

Wood, K. S. 1994, in SPIE Proceedings, Vol. 1940, Small Satellite Technology and Applications III, 105

Zdziarski, A. A., Poutanen, J., Paciesas, W. S., & Wen, L. 2002, ApJ, 578, 357

Zurita, C., et al. 2002, MNRAS, 334, 999